Synergy of multi-wavelength radar observations with polarimetry to retrieve ice cloud microphysics

Eleni Tetoni

Munich 2022

Synergy of multi-wavelength radar observations with polarimetry to retrieve ice cloud microphysics

Eleni Tetoni

Dissertation
at the Faculty of Physics
of Ludwig Maximilians University
Munich

submitted by
Eleni Tetoni

Munich, October 2022

First supervisor: Prof. Dr. Bernhard Mayer

Second supervisor: Prof. Dr. Markus Rapp

Submission date: 10.10.2022

Oral examination date: 01.12.2022

To Nikos and Frufru that I left back home..

To Sissi who left us so early..

Abstract

Numerical weather and climate models are known to reliably represent large scale precipitation features. However, uncertainties can be introduced for smaller scale processes due to resolution constraints. The representation of microphysical processes in models is considered to be a challenging task when it comes to ice microphysics. Ice cloud particles can have different habits, sizes or densities and the ice processes that are significant for the evolution of precipitation, are not always easily captured. In numerical models, it is a common approach that the ice cloud particles or ice microphysical processes are represented using simplified parameterizations. To reduce the uncertainties produced by these parameterizations, ice retrievals which constrain ice microphysical properties are needed.

Radars are suitable instruments for ice hydrometeor observations. Usually single-frequency radars are not able to perform measurements that can provide adequate ice microphysical information without using empirical relations. The combination of radars emitting at different frequencies (multi-frequency technique) exploit the different scattering signatures of ice hydrometeors in the Rayleigh and Mie regime and provide qualitative information about the size of the prevalent ice cloud particles. However, radars which are located at the same place performing vertical measurements provide only limited shape information, i.e., aspect ratio, from polarimetric observations. In this study, a novel approach was investigated combining the multi-frequency technique with slant-wise polarimetric observations. Two radars emitting at different frequencies and located at different places were used to study ice microphysics over the Munich area. Located at a horizontal distance of 23 km, the weather radar POLDIRAD (C band; 5.5 GHz) and the cloud radar MIRA-35 (Ka band; 35.2 GHz), performed coordinated scans towards each other, providing dual-frequency measurements with sensitivity to ice hydrometeors size. In addition to dual-frequency observations, the scanning weather radar provided radar reflectivity as well as differential radar reflectivity measurements with sensitivity to ice hydrometeors mass and shape, respectively. This combination was found to successfully work, during snowfall events when the hydrometeor attenuation can be considered negligible. All aspects to be considered e.g., spatiotemporal and volumetric mismatches, radar calibration uncertainty, were also analyzed in this study.

To derive quantitative ice microphysics information, the novel measurement combination was compared to scattering simulations for ice particles. The ice hydrometeors were represented by the simple – yet adjustable – assumption of the soft ice spheroids following a well-established mass-size relation and an exponential particle size distribution. The scattering simulations were calculated using the T-Matrix algorithm for different shapes, sizes and masses of the ice spheroids by varying the aspect ratio, the median mass diameter and the ice water content of the particle size distribution. Microphysical properties of ice hydrometeors were retrieved and could explain the radar observations when suitable assumptions were used, i.e., when oblate ice spheroids that follow the mass–size relation of aggregates, instead of the well-known Brown and Francis, were used in the simulations. The combination of the Brown and Francis mass-size relation, which suggests low density for large ice particles, along with the soft spheroid model could not well represent the radar observations as it led to very low simulated polarimetric signal which didn't match the measured one. Besides developing an ice

microphysics retrieval, a method to correct the radar measurements for hydrometeor attenuation, exploiting the output of the ice retrieval, was also developed. Using slant-wise polarimetric radar measurements along with dual-wavelength ratio, the ambiguity in the size retrievals caused by the variable shape of the ice particles could be reduced. Especially in the region above the Ka-band cloud radar, the contribution of slant-wise polarimetric measurements is of a great importance not only to constrain the shape but also to reduce the uncertainty in the size retrieval.

In the last part of this doctoral thesis, sensitivity studies on the assumptions used for the development of the ice microphysics retrieval were conducted. Particularly, the effect of the assumed mass-size relation, particle size distribution, oblate or prolate type and horizontal flutter of the ice spheroids on the ice retrieval results was investigated. The sensitivity analysis showed that the mass-size relation is the most significant component and needs to be better constrained in the ice retrieval by using additional measurements, e.g., Doppler velocity from the cloud radar. In the same analysis, several combinations or modifications of the original Brown and Francis and aggregates mass-size relations were tested in the ice microphysics retrieval. Investigating in depth two case studies of snowfall, comparisons of the retrieved ice water path to the ice water path from Terra MODIS were conducted for all mass-size relation assumptions. The comparisons showed that the best agreement between the two ice water paths was found when a mass-size relation with half the effective density of the original aggregates was used in the ice retrieval. Although of secondary importance, the oblate or prolate assumption, the horizontal flutter and the particle size distribution of the ice spheroids used in the scattering simulations can also influence the results of the ice retrieval. For instance, using a gamma over an exponential particle size distribution, it results approximately to 20% different retrieved median mass diameter and ice water content. However, the difference is lower (< 5–10%) for the shape retrieval. In a possible extend of the ice microphysics retrieval, in situ data or vertical radar measurements of linear depolarization ratio could help to constrain the particle size distribution or the oblate/prolate assumption, respectively.

Using the methodology presented in this doctoral thesis and exploiting more observations in a possible extend of this study, the ice microphysical information could be better constrained and used in numerical weather and climate models improving not only nowcasting but also leading to better forecasting.

Publications

Several parts of the present doctoral thesis belong to the following published research article:

Retrievals of ice microphysical properties using dual-wavelength polarimetric radar observations during stratiform precipitation events

Eleni Tetoni[1], Florian Ewald[1], Martin Hagen[1], Gregor Köcher[2], Tobias Zinner[2], and Silke Groß[1]

[1]Deutsches Zentrum für Luft- und Raumfahrt (DLR), Institut für Physik der Atmosphäre, Oberpfaffenhofen, Germany

[2]Meteorologisches Institut, Ludwig-Maximilians-Universität, Munich, Germany

Published in Atmospheric Measurement Techniques (AMT) scientific journal in 2022, with the identifier doi: https://doi.org/10.5194/amt-15-3969-2022.

For this work Eleni Tetoni, Dr. Florian Ewald, Dr. Martin Hagen and Gregor Köcher performed radar measurements during snowfall events. Eleni Tetoni developed the ice microphysics retrieval algorithm and wrote the paper under the guidance of Dr. Florian Ewald. During the radar measurements and the development of the ice retrieval, Dr. Silke Groß and Dr. Tobias Zinner contributed with productive discussions and ideas for the implementation of this study and the writing of the aforementioned paper.

Table of Contents

Chapter 1

1 Introduction

This section contains work, which has already been published by Tetoni et al. (2022) in Atmospheric Measurement Techniques (AMT), entitled *"Retrievals of ice microphysical properties using dual-wavelength polarimetric radar observations during stratiform precipitation events"*.

Clouds are known to be a significant ingredient for a romantic, late-afternoon walk by the sea to watch the sunset. Who isn't impressed by the color they get when the sun passes through them? Due to their variety in shapes, sizes, scales of grey – but also other colors, e.g., red –, clouds have attracted several kinds of people throughout the centuries. Not only romantics or photographers but also scientists or philosophers are always amazed by spectacular clouds. Very early already, the Greek philosopher Aristotle (384–322 BC) wrote:

> *"...εἰ δὴ γίγνεται ὕδωρ ἐξ ἀέρος καὶ ἀὴρ ἐξ ὕδατος, διὰ τίνα ποτ' αἰτίαν οὐ συνίσταται νέφη κατὰ τὸν ἄνω τόπον;...*
> *...ἢ οὖν οὐκ ἐξ ἅπαντος τοῦ ἀέρος πέφυκεν ὕδωρ γίγνεσθαι, ἢ εἰ ὁμοίως ἐξ ἅπαντος, ὁ περὶ τὴν γῆν οὐ μόνον ἀήρ ἐστιν ἀλλ' οἷον ἀτμίς, διὸ πάλιν συνίσταται εἰς ὕδωρ..."*

(Aristotle, Meteorologica, Book I, 340α)

wondering what is the reason that clouds aren't formed in the upper region, since water is generated from air and air from water. Regarding the cloud formation, he also hypothesized that, either it is not all air which water is generated from, or if it is, then the medium that surrounds the Earth is not only air but a kind of vapor which is again condensed back to water (in free translation).

Depending on their composition, cloud features can be thicker or thinner and they can be extended in a consist of smaller (some microns) or larger (several kilometers) spatial scale features. They play a key role in the climate system of the Earth as they interact with the shortwave solar radiation as well as the longwave terrestrial radiation developing a friendly environment for the evolution of life on Earth. Clouds are also significant components of the hydrological cycle. They are generated from the evaporation and the condensation of water from the sea, rivers or lakes but they also contribute to these water sources via precipitation (Fig. 1.1) leading to a vital, perpetual water exchange between Earth and atmosphere. Depending on the atmospheric dynamics and their temperature, clouds are divided into three main categories; ice-phase, mixed-phase and water-phase clouds, consisting of ice, water and ice, as well as water hydrometeors, respectively.

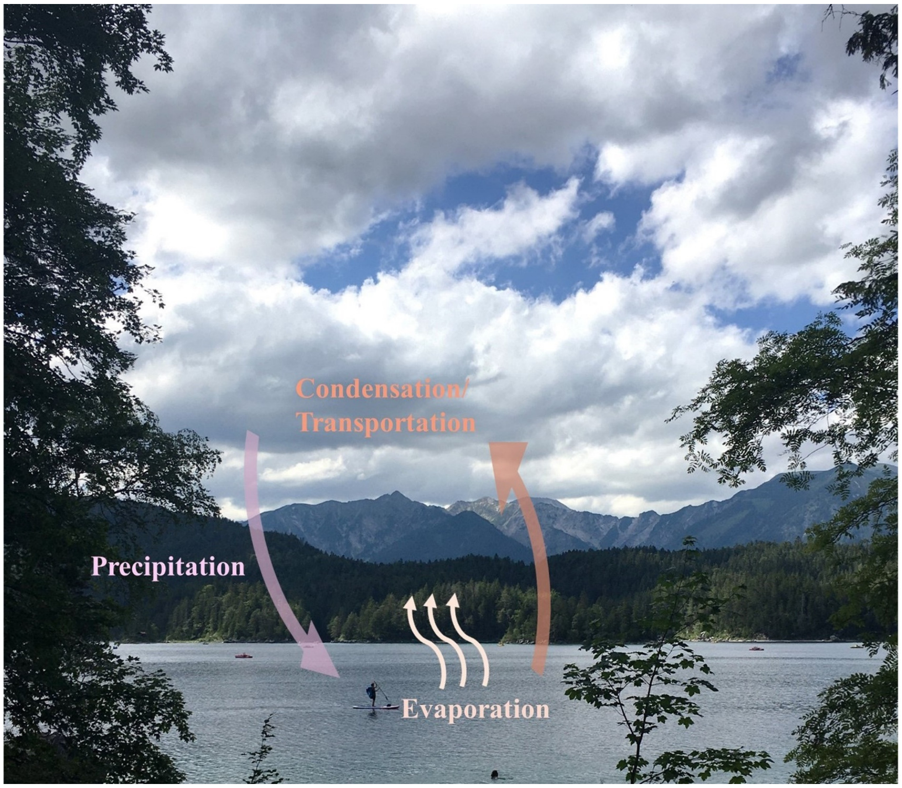

Figure 1.1: Clouds **-** a part of the hydrological cycle (location: Eibsee, Bavaria, Germany).

1.1 Ice clouds microphysics

The ice phase not only is the predominant cloud phase at mid and higher latitudes (Field and Heymsfield, 2015), but also approximately 63% of the global precipitation originate from that phase (Heymsfield et al., 2020). Clouds consisting of ice crystals reflect the shortwave incoming solar radiation, but they can also trap the longwave terrestrial radiation interfering in the energy budget of the Earth (e.g., Liou, 1986). Their influence on the radiation budget not only depends on their top height but also on ice crystals habits and effective ice crystal size (Zhang et al., 2002). Ice crystals can be found in a large variety of habits, sizes and densities in clouds. This variety is strongly connected to the ice microphysical processes, e.g., aggregation, deposition, riming, that take place inside the clouds. These processes have a great impact on the precipitation type, i.e., stratiform or convective, that reaches the surface of the Earth.

1.1.1 Precipitation formation in ice clouds

The ice microphysical processes can significantly affect the lifetime of a cloud. When a cloud extends above the 0 °C isotherm then it is assumed to be an ice cloud or a cloud region consisted of droplets that exist at temperatures below 0 °C without forming ice crystals yet. These droplets are called supercooled water droplets and play a leading role in the different ice processes taking place in a cloud. When supercooled water droplets are present in an ice cloud then the last is called mixed-phase cloud (e.g., Wallace and Hobbs, 2006).

Ice crystals may form when the ambient temperature is lower than 0 °C. This formation can occur via two kinds of nucleation, i.e., *homogeneous* and *heterogeneous* nucleation. *Homogeneous* nucleation can happen with spontaneous freezing of a liquid drop forming a stable ice nucleus or deposition or sublimation of water vapor molecules forming a stable ice embryo via collisions. The last mechanism, only occurs when extreme supersaturation conditions are present (400–600 %) but such conditions are unlikely to be met in the atmosphere. For negative temperatures around –40 °C or warmer, *heterogeneous* nucleation can take place. With this mechanism ice particles are formed by supercooled droplets (cloud droplets that are not frozen yet) and water vapor in the presence of suspended nuclei. *Condensation nucleation* is a type of heterogeneous nucleation and occurs when water vapor or a supercooled droplet is condensed onto a suspended nuclei at freezing temperature forming an ice particle. Moreover, if the ice particle is formed from the insertion of a suspended nuclei into the supercooled droplet and freezing follows, then an *immersion freezing* is taking place. Another way of heterogeneous nucleation is when ice particles are formed from the collision of a suspended nuclei with supercooled droplets and freezing follows and this process is known as *contact freezing* (homogeneous and heterogeneous nucleation processes are described in e.g., Houze, 2014; Liou and Yang, 2016 and many more). The different nucleation processes that can lead to ice particles formation are described in Fig. 1.2.

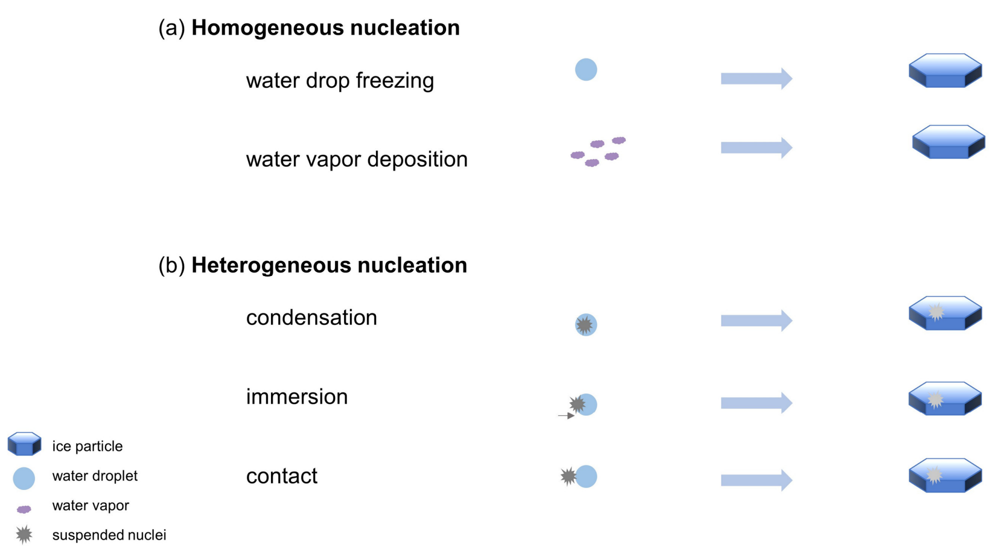

Figure 1.2: Schematic representation of the (a) homogeneous and (b) heterogeneous ice nucleation processes.

After an ice particle have formed, it can take part in different microphysical process depending on the cloud dynamics. There are different mechanisms that can cause growth or shrinkage of ice particles. Some of the most-known ice microphysical processes (e.g., Houze, 2014) are,

- <u>deposition</u>: water vapor is deposited onto an ice particle
- <u>aggregation</u>: ice particles collide with each other
- <u>riming</u>: ice particles collide with supercooled water droplets and then, freezing occurs

leading to growth of ice particles and,

➢ sublimation: ice particle loses mass as water vapor which escapes to the surrounding environment

leading to shrinkage of ice particles.

It is possible that more than one of the aforementioned ice processes take place inside a cloud until the precipitation starts. Depending on the ambient temperature and atmospheric dynamics, these ice particles can be found in different sizes or shapes (e.g., Bailey and Hallett, 2009) in nature. Then, they can fall to the ground as snow/graupel/hail (higher density ice particles tend to fall faster than lower density ice hydrometeors) or they melt at the 0 °C isotherm (melting layer; ML) and fall as rain or even evaporate before reaching the ground.

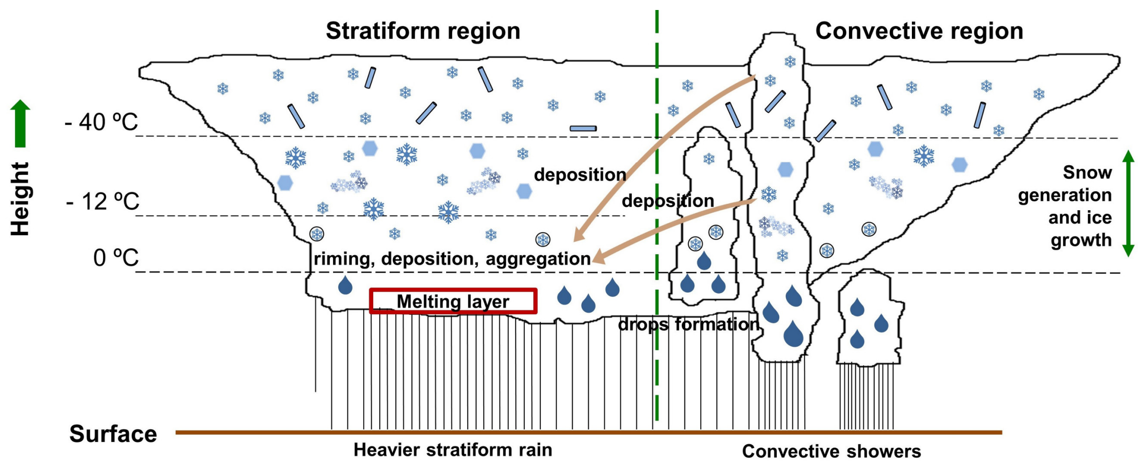

Figure 1.3: A representation of the ice microphysical processes taking place in a mesoscale convective system. The figure is adapted from Houze (1989) and modified to a colored version and to visualize ice particles as well.

The different ice processes play a leading role in the precipitation formation and they can also affect the type, i.e., stratiform or convective, as well as the amount of precipitation, indicating the connection between micro- and macrophysics. In Fig. 1.3, an example of a mesoscale convective system, where several ice microphysical processes take place, is presented (adapted from Houze, 1989 and modified). Mesoscale convective systems can extend to several kilometers. In these systems there is always a leading precipitation region with strong updrafts which produces convective precipitation at the ground. Behind this region, the stratiform precipitation region follows. In Fig. 1.3, the two different regions along with the ice microphysical processes are presented. Especially for the stratiform region ice particle growth can occur for temperatures higher than –40 °C, approximately. Several studies have been conducted about ice particles growth through different microphysical processes so far (e.g., laboratory study on ice aggregation; Connolly et al., 2012, or riming; Erfani and Mitchell, 2017).

1.2 Relevance of ice microphysics in NWP

For better weather forecasting but also nowcasting, the different ice processes or the various ice crystal characteristics have to be included in the numerical weather prediction (NWP) model parameterizations. However, the representation of ice cloud microphysics in model simulations remains a challenging task until today and can introduce large uncertainties due to a misrepresentation of ice processes or ice particle characteristics. The large variety of shapes, sizes, densities and fall velocities of ice hydrometeors is sometimes inadequately constrained in NWP models. The different parameterizations in ice cloud microphysical schemes can lead to uncertainties in weather predictions or shortwave and longwave radiation budget estimations. Sullivan and Voigt (2021) showed, for instance, that inadequately constrained parameters in ice schemes, like a poorly constrained effective radius of ice particles can lead to biases in cloud radiative heating as well as infrared cooling. The ice microphysical schemes used in NWP are divided into two categories, i.e., spectral bin schemes and bulk schemes, depending on the variables that need to be defined a-priori. In spectral bin schemes, microphysical information such as the particle size distribution (PSD) of the ice hydrometeors is not needed a-priori. In these schemes, a number of size or mass bins is defined beforehand, and each one of the microphysical variables are predicted individually (e.g., Lynn et al., 2005). In bulk schemes, the particle size distribution of the ice particles is pre-defined and fixed (e.g., exponential or gamma) and only bulk variables are predicted (e.g., mixing ratio). The bulk schemes are categorized as 1-moment, 2-moment and 3-moment schemes depending on the number of the predicted variables that they provide (e.g., Lin et al., 1983; Morrison et al., 2009; Milbrandt and Yau, 2005a; Milbrandt and Yau, 2005b).

Several studies have shown that the poor representation of ice growth processes such as deposition, riming and aggregation can cause deviations between the predicted parameters from models and the measured parameters from different scientific instruments, e.g., meteorological radars. Numerical weather and numerical climate models sometimes cannot capture microphysics very well for different parameterizations used (e.g., Wu et al., 2021; Huang et al., 2022). Brdar and Seifert (2018) presented the novel Monte-Carlo microphysical model, McSnow, aiming for a better representation of aggregation and riming processes of ice particles. Some other numerical weather models are used to predict microphysics information about ice hydrometeors (e.g., Predicted Particle Properties (P3), Morrison and Milbrandt, 2015). In Lin et al. (2021), new microphysical processes and ice particle properties, i.e., ice sedimentation, terminal velocity, rimed ice as a new hydrometeor type in the classification scheme as well as the feeding of stratiform clouds with detrained ice hydrometeors, were parameterized and led to model simulations that better match the radar observations. Köcher et al. (2022) evaluated different numerical weather models comparing dual-wavelength and polarimetric variables with model simulations, while review studies like Morrison et al. (2020) pointed the challenges, e.g., shape or PSD constraint, that have to be considered with special care when it comes to modelling of ice microphysics.

The assumptions used for the representation of ice microphysics can lead to different models output. For instance, Morrison et al. (2015) presented radar measurements of a mesoscale convective system, similar to that from Fig. 1.3, which was formed by the merging of three different convective systems near Oklahoma on 19 June 2007. The radar measurements were performed by the dual-polarization S-band KOUN weather radar (a description of such system can be found in e.g., Zrnic et al., 2006). Figure 1.4 (upper part) shows the radar measurements on a horizontal grid (upper left panel). In the upper right panel of Fig. 1.4, the vertical cross-section of the gridded measurements is shown. The convective region appears in reddish colors in both cases. The stratiform region is following the convective region with a weaker received radar signal compared to the convective part of the system. Below the measurements, simulations for that case study using different microphysical schemes are presented (Fig. 1.4 lower panels). By eye, the three simulation panels show differences especially in the convective region. The main reason for this is the different assumptions that the three schemes use. The P3 scheme (Fig. 1.4 lower left panel) considers dense and thus, fast-falling ice particles that are similar to hail for the convective core and less dense and thus, slowly-falling ice particles for the other regions. Moreover, the MOR-G (Fig. 1.4 lower right panel) assumes that the rimed ice particles behave like graupel in the Morrison scheme (e.g., Morrison et al., 2005; Morrison et al., 2009; Morrison and Milbrandt, 2011) while, MOR-H (Fig. 1.4 lower middle panel) assumes that the rimed ice particles behave like hail considering respective ice microphysical characteristics in the simulations. The differences in ice microphysical schemes reveal the need to constrain microphysics used in NWP. Therefore, ice retrievals that are developed comparing radar measurements to scattering simulations and predict information about the shape, the size and the mass of the detected ice hydrometeors, are needed. In this way, the ice mechanisms can be better understood and constrained in models.

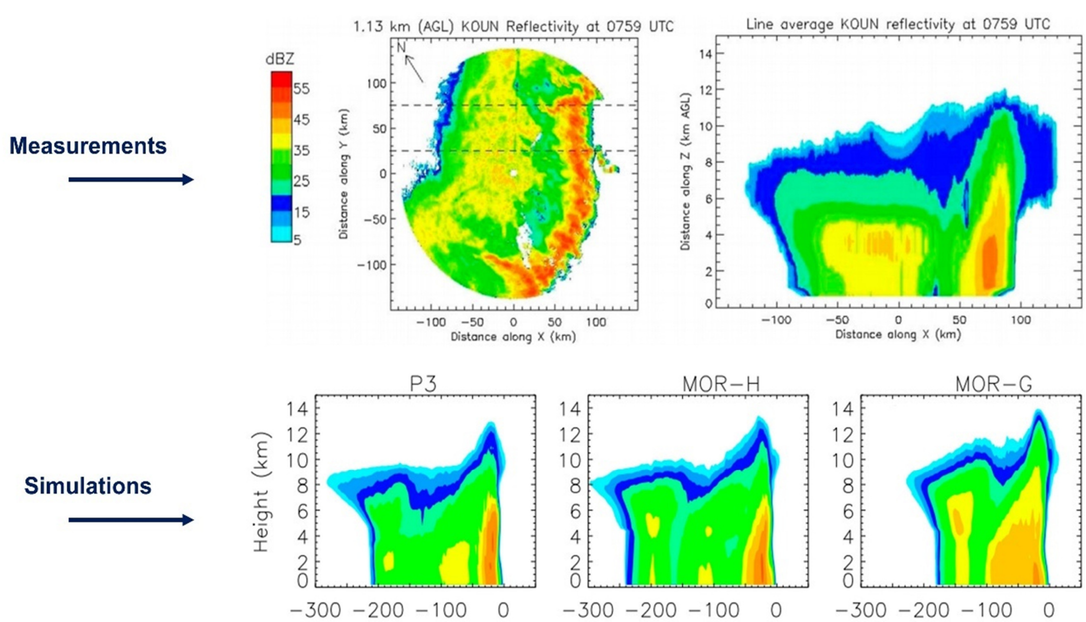

Figure 1.4: KOUN radar measurements from 19 June 2007 (upper part). In upper part the radar measurements on a horizontal grid (left) and vertical cross-section of the gridded measurements (right) are presented. Model simulations using different ice microphysical schemes (lower part). Adapted from Morrison et al. (2015) (their Fig. 1 and 5a–c) and merged in a single figure.

1.3 Radar meteorology

RADAR (RAdio Detection And Ranging; the word will be used in lower case letters in this study) systems are very popular in active remote sensing methods. Emitting electromagnetic radiation, radars are worldwide used to monitor weather phenomena in the atmosphere observed at longer distances. With radars it is possible to detect and monitor precipitation such as rain, snow and hail which are generated by microphysical processes inside clouds and fall to the ground. Except for precipitation, radars are able to provide information about the microphysical processes taking place in clouds, e.g., aggregation within fall streaks, but also properties about the ice hydrometeors themselves, e.g., size, shape, orientation and fall velocity. But what makes radars a suitable tool for the observation of atmospheric hydrometeors?

Atmospheric hydrometeors can be observed in multiple ways, e.g., in situ or with passive/active remote sensing techniques. In situ measurements of atmospheric hydrometeors are usually performed with aircraft probes. Although such instruments can provide significant information about the hydrometeors shape or size (e.g., particle size distribution), they are not able to provide complete 2D cross-sections of clouds containing hydrometeors. Passive remote sensing instruments, e.g., radiometers, collect the scattered radiation from hydrometeors and provide information about optical cloud properties, like the optical thickness and the effective radius. However, the passive remote sensors provide an integrated information and not spatial information along the line of sight. On the other hand, active remote sensing instruments, e.g., lidars or radars, can supply spatial information as they emit radiation in the atmosphere through beam pulses that interact with atmospheric hydrometeors. The radiation returning to the antenna provides information about the properties and the position of the detected hydrometeors. For atmospheric hydrometeors and thus, for observations through all cloud types, radars are very suitable instruments due to the wavelength used. Both cloud (merely for cloud observations) and weather (merely for nowcasting during storms and other weather phenomena) radars operate in the microwave region wherein clouds are semi-transparent. Therefore, radars are ideal for observations of e.g., cloud droplets, raindrops, ice particles.

Observations have shown that the size of atmospheric hydrometeors lies within the range of some microns and up to some centimeters. In particular, cloud droplets vary in the range of 1–100 μm, drizzle droplets are a bit larger in the range of 50 up to some hundreds of microns and raindrop sizes start from some hundreds but can reach up to some thousands of microns. On the other hand, ice particle sizes usually lie within the range of 10–5000 microns, but in some cases (i.e., hail) they can reach some centimeters in size (Houze, 2014). Atmospheric hydrometeors interact with radiation by scattering or absorption. Figure 1.5 shows the different scattering regimes regarding the particle size and wavelength of the incident radiation. The scattering regimes are defined by the size parameter $x = \frac{2\pi r_p}{\lambda}$, with r_p the particle radius and λ the wavelength. More details about the scattering signatures of particles in different regimes can be found in Section 2.2 of the present doctoral thesis. In Fig. 1.5, the wavelength ranges in which meteorological radars operate, i.e., cloud and weather radars, are also indicated.

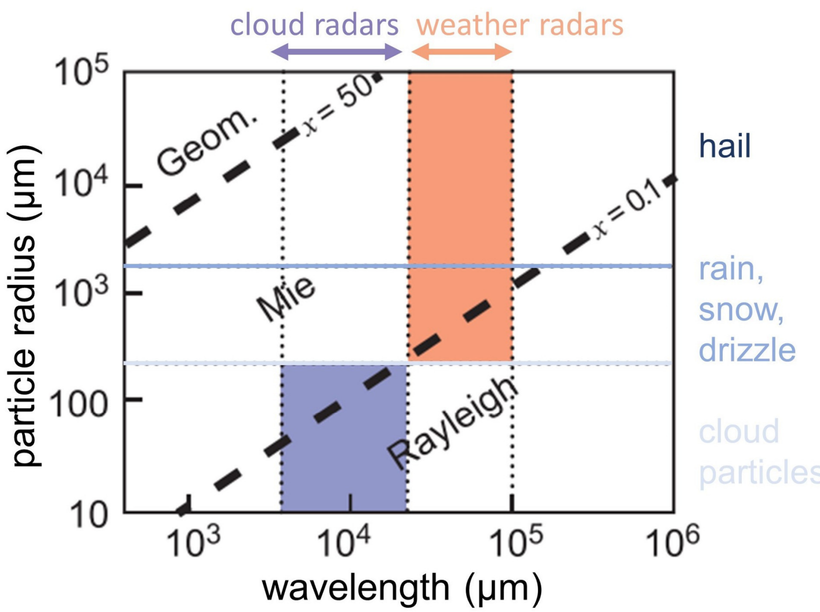

Figure 1.5: Scattering regimes regarding the size of the particle and the wavelength of the radiation. The colored lines show the typical size regions for the different hydrometeors. The dashed lines divide the different scattering regimes, i.e., geometric, Mie and Rayleigh scattering according to 0.1 and 50 size parameter x. The blue and orange shaded areas are the domains in which cloud and weather radars operate, respectively. The figure is adapted from Houze (2014), their Fig. 4.1, and modified.

1.3.1 Radar network in Germany

In Germany there is a radar network consisting of 17 C-band weather radars operated by the Deutscher Wetterdienst (DWD). This network monitors precipitation and wind proving three-dimensional information and offering the possibility of nowcasting and weather surveillance and thus, civil protection throughout the whole country. Among the operational radar systems, there is one research weather radar, operated at the Hohenpeißenberg Meteorological Observatory. All weather radar instruments of the network provide high spatial and temporal resolved observations with a maximum horizontal range of approximately 180 km. In addition to civil protection and nowcasting, these high-resolution radar data are exploited by numerical weather models increasing the quality of the weather forecasts provided by the DWD (source: Deutscher Wetterdienst; https://www.dwd.de/DE/Home/home_node.html, last access: 08 April 2022). An overview of the German radar network operated by the DWD is presented in Fig. 1.6.

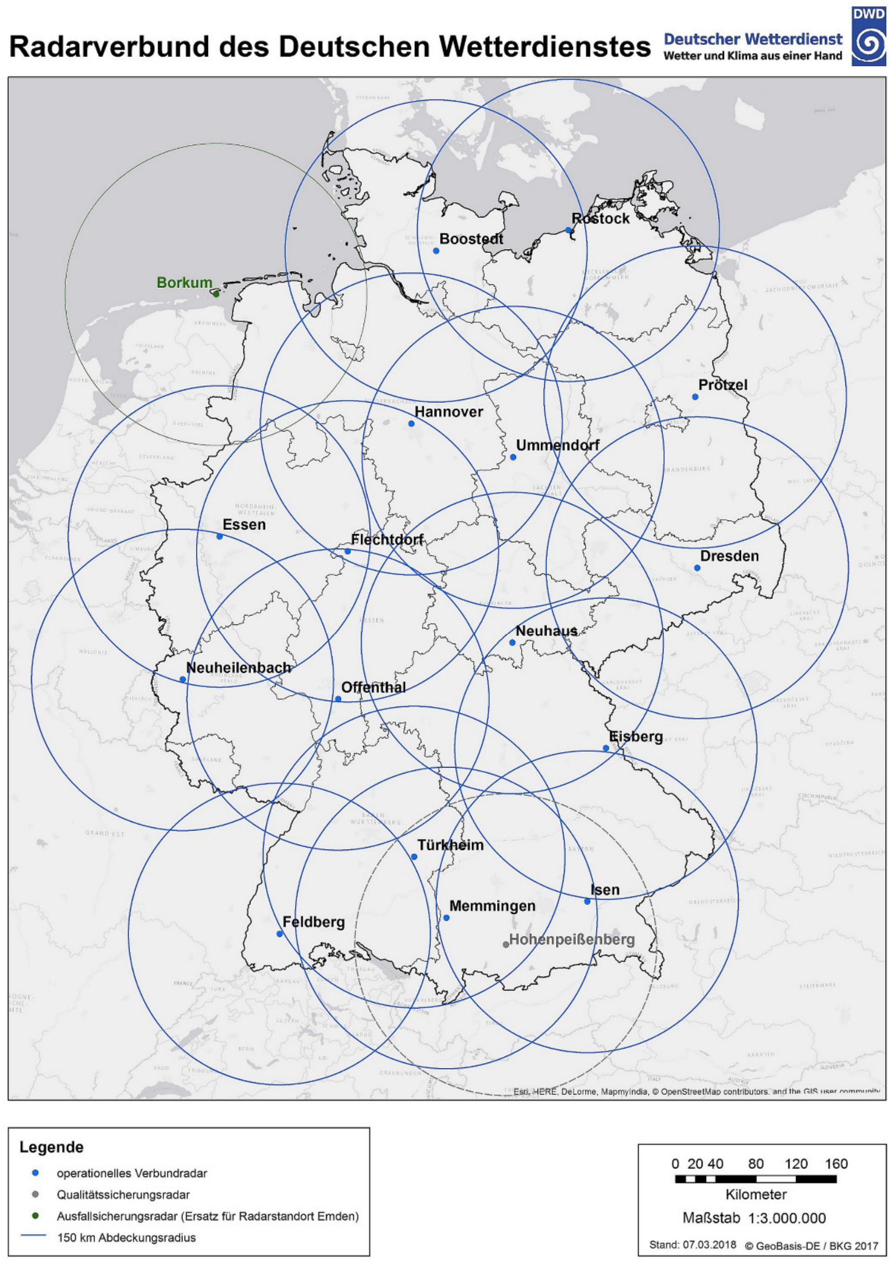

Figure 1.6: DWD german radar network. The figure is adapted from Deutscher Wetterdienst (source: Deutscher Wetterdienst; https://www.dwd.de/DE/Home/home_node.html, last access: 08 April 2022).

1.3.2 Radar measurements

Many studies have shown how millimeter-wave radar measurements can be used to retrieve ice microphysics, and in particular, ice water content (IWC) profiles in clouds (e.g., Hogan et al., 2006). However, stand-alone single-frequency radar measurements cannot constrain microphysical properties such as ice particle size and shape simultaneously without using empirical relations. Dealing with more parameters (e.g., IWC, size and shape) more measurements are needed (e.g., Trömel et al., 2021). Thus, observations or simulated radar parameters are often combined with other remote sensing instruments, e.g., with lidars, to retrieve microphysical properties such as the effective radius of cloud ice particles (Cazenave et al., 2019), or with infrared radiometers (Matrosov et al., 1994) to retrieve the median diameter of the ice particles size distribution.

The scattering of radar waves is sensitive to the size and number concentration of particles. Therefore, another way to gain microphysics information is to use multi-frequency (or dual-frequency when the scattering of radar waves from two radars is used) radar observations (also known as dual-wavelength ratio, DWR, observations) as they exploit the scattering properties of ice particles in both the Rayleigh and the non-Rayleigh regime. To this end, frequencies are chosen with respect to the prevalent particle size. In the case of dual-frequency techniques, one frequency is chosen to be in the Rayleigh regime (e.g., S, C or X band), where particle size is much smaller than the radar wavelength, and the other is chosen to be in the Mie regime (e.g., Ka, Ku or W band), where particle size is comparable or larger than the radar wavelength. In this way, size information about ice hydrometeors can be obtained. The dual-frequency approach has been widely used in many studies in the past providing microphysics information. In particular, the dual-frequency method (e.g., Matrosov, 1998) has been used in ice studies to estimate the snowfall rate *R* or for the Quantitative Precipitation Estimation (QPE). Matrosov (1998) developed a dual-frequency method to estimate *R*, supplementing experimental Z_e-R relations with a retrieved median size. In other studies, such as Hogan and Illingworth (1999) and Hogan et al. (2000), dual-frequency measurements from airborne and ground-based radars were used to obtain information about ice crystals sizes as well as IWC for cirrus clouds. Lately, the combination of multiple dual-frequency measurements has been explored to provide more microphysics information, e.g., ice particles habits or density. Kneifel et al. (2015) developed a triple-frequency method to derive ice particle habits information from three snowfall events measured during the Biogenic Aerosols-Effects on Clouds and Climate (BAECC) field campaign (Petäjä et al., 2016). The triple-frequency method was also used by Leinonen et al. (2018b) to develop an algorithm that retrieves ice particle size and density as well as number concentration using airborne radar data from the Olympic Mountains Experiment (OLYMPEX, Houze et al., 2017). More recent studies (e.g., Trömel et al., 2021) have underlined that multi-wavelength (also known as multi-frequency) measurements should be combined with other types of radar observations, e.g., polarimetric variables or Doppler velocity to improve our understanding on ice microphysics. The ice particle density, in particular, causes large ambiguity for dual-frequency techniques, while Doppler velocity measurements can better constrain the particle density as the fall speed is strongly connected to it. Specifically, Mason et al. (2018) used vertically pointing Ka- and W-band cloud radars to combine dual-frequency and Doppler measurements to provide information about the PSD and an ice particles density factor which is connected to ice particles shape and mass, but also terminal velocity and backscatter cross-section. In Mason et al. (2019), the PSD and morphology of ice particles were thoroughly explored using the triple-frequency method to improve ice particle parameterizations in numerical weather prediction models. In the same study, it was also found that for heavily rimed ice particles, the triple-frequency radar observations can constrain the width parameter μ of the PSD. Recently, Mroz et al. (2021) used single-frequency (X band), triple-frequency (X, Ka, W band) as well as triple-frequency combined with Doppler velocity radar measurements to develop different versions of an algorithm that retrieves the mean mass-weighted particle size, IWC and the degree of riming. The multi-frequency versions of the algorithm retrieved IWC with lower uncertainties compared to the single-frequency version. Additionally, with the multi-frequency approaches, the algorithm was also able to provide better ice particle density information as well as mean mass-weighted diameter information for larger snowflakes (larger than 3 mm size) in contrast to single-frequency approach. Overall, the multi-frequency versions of the algorithm performed better as the retrieved parameters agreed better with in situ measurements.

Beyond multi-frequency techniques, ice microphysics information can be obtained from polarimetric radar measurements. In previous studies, polarimetry was commonly used for snowfall rate estimation. Bukovčić et al. (2018), for instance, used polarimetric radar variables to study the IWC and the resulting snow water equivalent rate. Besides precipitation rate studies, polarimetry is a versatile tool to obtain information about the size distribution and the shape of ice particles. Additional characteristics, like the particle orientation and their canting angle distribution, as well as the variable refractive index of melting or rimed ice crystals have a further influence on polarimetric radar signals. To untangle some of these particle properties, polarimetric weather radars can provide several parameters such as differential radar reflectivity (ZDR), linear depolarization ratio (LDR), reflectivity difference (ZDP), cross-correlation coefficient (ρHV), differential propagation phase (φDP) and specific differential phase (KDP). The different sensitivities of these parameters have been widely used in classification schemes of atmospheric hydrometeors. For instance, Höller et al. (1994) developed one of the first algorithms to distinguish between rain, hail, single or multi-cells using ZDR, LDR, KDP and ρHV measurements during the evolution of a thunderstorm in southern Germany. This algorithm was extended to estimate hydrometeor mass concentrations (Höller, 1995). Later, Straka et al. (2000) summarized the characteristics of different hydrometeors types depending on their radar signatures at a wavelength of 10 cm. Polarimetric radar variables have also been exploited in studies which focus in ice growth processes. In Moisseev et al. (2015), particularly, ZDR along with KDP has been used to investigate the growth processes of snow and their signatures on dual-polarization and Doppler velocity radar observations. In Tiira and Moisseev (2020) vertical profiles of ZDR were combined with KDP and Z_e for the development of an unsupervised classification for rain and snow events. In that study, the growth processes of ice particles were studied using several years of the Ikaalinen C-band radar data, in Hyytiälä forestry station in Juupajoki, Finland.

Although the size of atmospheric hydrometeors is strongly correlated to dual-frequency measurements, many studies have shown that these kind of measurements are also sensitive to the shape of ice hydrometeors. This sensitivity to shape was shown e.g., in Matrosov et al. (2005), where they estimated the increased uncertainty in particle size retrievals when the particles are assumed to be spherical only. One solution to that problem was offered by Matrosov et al. (2019), who stated that the shape of ice hydrometeors can be disentangled from dual-frequency data by studying the angular dependence of these measurements during elevation scans. Non-spherical ice hydrometeors should show a strong angular dependence compared to spherical ice particles. Besides this scanning approach, the combination with polarimetry from collocated or nearby radar instruments could offer a promising solution to disentangle the contribution of size and shape in dual-frequency measurements. While the shape can be constrained by ZDR measurements, the size of the detected particles can be determined using dual-frequency techniques.

1.4 Problem statement and scientific objectives of this thesis

The multi-wavelength or – in the case of two radars – dual-wavelength method is the state-of-the-art to constrain ice cloud microphysics using radar observations. This method exploits the Mie effects in the shorter wavelength to infer particle size information and has been already used in several studies in the past (e.g., Hogan et al., 2000; Kneifel et al., 2015). A common approach in such studies is to use radars that are located in the same area and perform vertical measurements.

Vertically pointing radars are known to provide valuable Doppler spectra observations (e.g., Kneifel et al., 2016; Kalesse et al., 2016). However, they cannot simultaneously provide slant-wise polarimetric measurements, e.g., ZDR, which can be useful to estimate the shape of ice particles. As horizontally aligned ice plates are axially symmetric in the horizontal plane – xy plane in Fig. 1.7a –, appear to be roughly spherical for vertically pointing radars due to the observation geometry. For this reason, when vertically pointing radars are used to retrieve ice microphysical properties, e.g., size, an assumption about the shape of the ice hydrometeors, i.e., how much spherical they are, has to be made.

The present study aims to retrieve microphysical information (e.g., size, shape, mass) from ice particles detected into clouds. As the dual-wavelength method is known to provide valuable information about the particle size of ice hydrometeors, it is also used here. For shape retrievals, the feasibility to combine dual-wavelength radar measurements with slant-wise polarimetric radar observations is investigated. In this way, the shape of the ice hydrometeors could be constrained as polarimetric variables such as ZDR could be exploited, avoiding to make a shape assumption in the ice retrievals. To accomplish this in practice, the possibility to combine radar observations provided from different locations (Fig. 1.7b) is thoroughly investigated in the present doctoral thesis. In particular, the synergy of a research C-band weather radar, similar to those of the DWD radar network (Sect. 1.3.1), with a Ka-band cloud radar is used to study the aforementioned hypothesis. If this hypothesis is found to work, then the size, shape and mass of the detected ice hydrometeors can be retrieved by developing a simple ice microphysics retrieval.

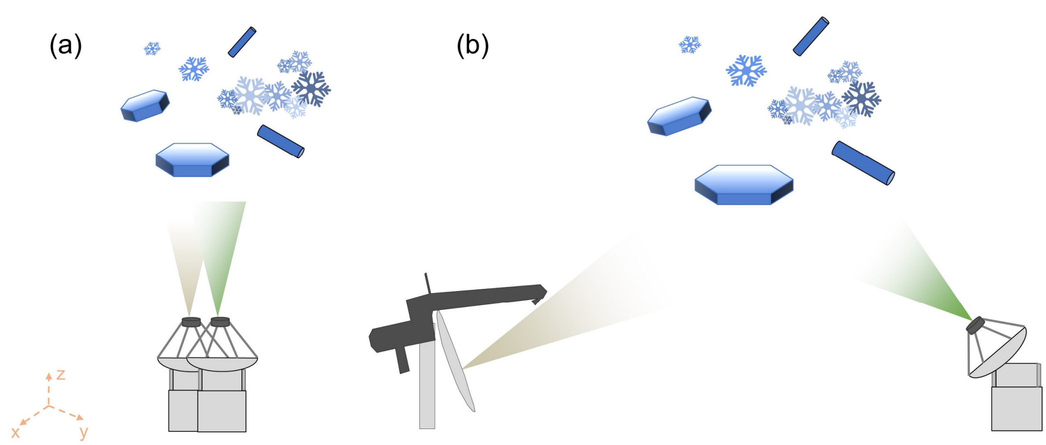

Figure 1.7: Dual-wavelength method radar setup of (a) other studies so far (b) this study.

1.4.1 Research questions and outline

While studying the hypothesis to combine slant-wise radar polarimetric observations with dual-wavelength for ice retrievals, the present doctoral thesis addresses three research questions.

Research Question 1: How can the dual-wavelength method be combined with polarimetry to obtain information about the size and shape of ice hydrometeors?

Research Question 2: How well can a simple ice particle model explain the dual-wavelength and polarimetric radar observations? Can this model be used for ice retrievals, i.e., size, shape, mass, making some assumptions about the microphysics of the ice particles?

Research Question 3: How are the ice retrievals affected by the assumptions about the (unknown) microphysics?

In particular, this doctoral thesis presents a feasibility study investigating whether it is possible to: *(1)* combine observations from two different radar systems, located in different places, to obtain reliable dual-wavelength and slant-wise polarimetric measurements of ice hydrometeors, *(2)* use the radar observations in combination with scattering simulations to retrieve ice cloud microphysics and *(3)* investigate how can the assumptions made for the ice particles, e.g., particle size distribution, influence the ice retrieval results. Using two spatially separated radar instruments, microphysical properties of ice hydrometeors are retrieved by developing an ice retrieval which uses a simple particle model to represent the observed ice particles. The ice retrieval uses a minimization technique to find the best match, i.e., lowest residual, between the ice scattering simulations and the radar measurements and at the end, resolves the ice water content, the median size and the apparent shape of the detected ice hydrometeors.

This dissertation is organized as follows: In Chapter 2 the basics about different ice microphysical parameters, electromagnetic radiation and radar basics are introduced. Subsequently, the methods used in this study are presented in Chapter 3. In particular, the instruments as well as the measurement strategy and the measurements error assessment are thoroughly described. Moreover, the scattering simulations for ice particles using the T-Matrix algorithm and different assumptions, e.g., the spheroid model, are presented in detail. Chapter 3 also demonstrates the methodology to combine DWR and polarimetric measurements along with the scattering simulations to retrieve microphysical properties of ice particles, i.e., development of the ice retrieval. In addition, the errors of the retrieved parameters are estimated. Chapter 4 presents the retrieval results for different assumptions of ice hydrometeors along with sensitivity studies investigating these assumptions in depth. In Chapter 5 the results from the previous chapter are discussed in detail, while in Chapter 6 the conclusions and summary of the present doctoral thesis are drawn.

Chapter 2

2 Theory

This section contains work, which has already been published by Tetoni et al. (2022) in Atmospheric Measurement Techniques (AMT), entitled *"Retrievals of ice microphysical properties using dual-wavelength polarimetric radar observations during stratiform precipitation events"*.

In this chapter the most significant ice microphysical properties will be presented (Sect. 2.1). All the mentioned parameters are substantial for the characterization of ice particles as well as for their scattering properties and thus, they will be described in detail. In Sect. 2.2, the electromagnetic theory principles this thesis is based on will be introduced while, in Sect. 2.3 the radar principle along with the used radar variables will be presented.

2.1 Ice particles microphysical characteristics

Observations have shown that ice particles can be found in different shapes, sizes, densities, but also in different orientations or fall speeds in nature. In this section, the most crucial parameters describing the ice hydrometeors will be thoroughly explained.

Characteristic size

The size of ice particles has been investigated by several studies (e.g., Hogan et al., 2000; Heymsfield et al., 2002; Lawson et al., 2006). This parameter of ice hydrometeors is intrinsically linked to their shape. Due to their asymmetric shape, ice crystals are not easy to be characterized by one size value (diameter or radius) and thus, different diameter/radius definitions can be used. One of the most common definitions used to characterize the ice hydrometeors size is the maximum dimension, also known as the *maximum diameter*, D_{max}. Figure 2.1 shows D_{max} of an aggregated ice particle, which is also the largest dimension in all axis of all conceivable planes that the ice aggregate lies on. As already mentioned, ice particles can be found in a variety of shapes in clouds. Therefore, it is likely that more than one ice crystal or aggregate can be found with the same maximum diameter but a totally different structure. In this case, D_{max} cannot provide adequate information to infer additional properties, e.g., the speed that these particles would fall to the ground. The *melted equivalent diameter*, D_{eq}, of ice hydrometeors is also commonly used to describe the particle size (Fig. 2.1). D_{eq} is the diameter of a spherical water droplet that has the same mass as the ice crystal. Differences between D_{max} and D_{eq} can thus, be used as an indication of the effective density of the described ice crystal. A more detailed description of some of the aforementioned sizes can be found in Hogan et al. (2012).

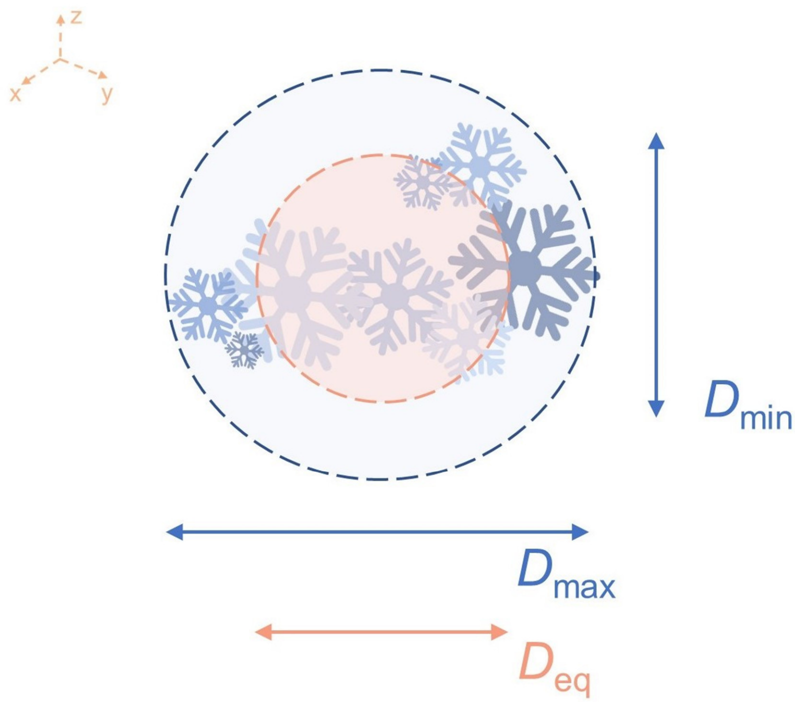

Figure 2.1: Different diameter definitions for an ice aggregate.

Depending on the application, and especially when the studies are focused on the properties of ice particles, other diameter definitions can be used; for instance, D_{mean}, the *mean-dimension diameter,* and D_{area}, the *equivalent-area diameter,* of a particle. D_{mean} is the rotationally averaged size, while D_{area} is the diameter of a sphere which has the same cross-sectional area like the ice particle.

Aspect ratio

Along with the size, the shape definition is equally important. The shape information can be expressed using different definitions, e.g., aspect ratio, axis ratio or sphericity. In this study the shape of the particles is described using the aspect ratio, AR, or the sphericity, *S*. The AR is defined here as the ratio of the horizontal to rotational axis of the ice particles and thus, expressed using the formula,

$$AR = \frac{horizontal\ axis}{rotational\ axis}\,. \tag{2.1}$$

Assuming z as the rotational axis in Fig. 2.1, it is obvious that $AR = \frac{D_{\text{max}}}{D_{\text{min}}} > 1$, with D_{min} the minimum diameter or minimum dimension of the particle. Using this definition, all ice particles in this study with AR > 1 are called oblates, while prolate and spherical particles have AR < 1 and AR = 0, respectively.

In the framework of the present study the *S* definition for shape information was used when the degree of asphericity was the focus of interest. The sphericity is defined as,

$$S = \frac{D_{\min}}{D_{\max}}, \tag{2.2}$$

and thus, it is found to be smaller than 1 for both oblate and prolate ice particles, while it is 1 for spherical particles.

Mass-size relation

The maximum dimension, $D_{\max}$, of ice particles is often used in connection to their mass according to a power-law formula, i.e., the mass-size relation. The mass *m* of ice particles is on average related with the maximum diameter $D_{\max}$ with,

$$\mathrm{m}(D_{\max}) = aD_{\max}^{b} \tag{2.3}$$

where,
a: the prefactor of the $\mathrm{m}(D_{\max})$, connected to the density at all particles sizes,
b: the exponent of the $\mathrm{m}(D_{\max})$, connected to the shape and growth mechanisms of particles.

For the mass of ice particles, the modified mass-size relation of Brown and Francis (Brown and Francis, 1995), BF95, as presented in Hogan et al. (2012) was initially used in this study,

$$\begin{aligned} \mathrm{m}(D_{\max}) &= 480D_{\max}^{3},\ D_{\max} < 6.6 \times 10^{-5}\ \mathrm{m} \\ \mathrm{m}(D_{\max}) &= 0.0121D_{\max}^{1.9},\ D_{\max} \geq 6.6 \times 10^{-5}\ \mathrm{m} \end{aligned} \tag{2.4}$$

where,
$D_{\max}$: maximum dimension of the ice particle in meters (m),
m: mass of the ice particle in kilograms (kg).
Providing information about the mass of the ice crystals, this formula captures the effective density (ρ_{eff}) of ice hydrometeors with respect to their size, when their shape is known. While the effective density of an ice particle decreases strongly with its size due to the exponent b = 1.9 in BF95, this effect was contrasted with a second $\mathrm{m}(D_{\max})$ with a higher and constant effective density. To that end, the $\mathrm{m}(D_{\max})$ of the irregular aggregate model from Yang et al. (2000), to simulate ice particles with an analog mass-size relationship, was exploited. Originally, the construction of these aggregates was fully described in Yang and Liou (1998) as an aggregated collection of geometrical hexagonal columns. In the present study, only the maximum dimension and mass of the underlying aggregates was emulated to build corresponding spheroids. To represent the detected ice hydrometeors with these ice aggregates, the density and thus, the mass of the particles can be calculated via the melted-equivalent diameter D_{eq} using $D_{\max}$ in Eq. (2.5).

$$\mathrm{m}(D_{\max}) = \frac{\pi\rho_{\mathrm{w}}D_{\mathrm{eq}}^{3}}{6} = \frac{\pi\rho_{\mathrm{w}}}{6}\, e^{\sum_{n=0}^{4} b_{\mathrm{n}}(ln(D_{\max}))^{n}\,3} \tag{2.5}$$

where b_{n} is a fitting coefficient taken from Table 2 in Yang et al. (2000), the water density ρ_{w} = 1 g cm^{-3} and D_{eq} as well as $D_{\max}$ are in microns. Figure 2.2a and 2.2b shows the mass and the effective density ρ_{eff} of the same-size ice particles as calculated using the aforementioned mass-size relations.

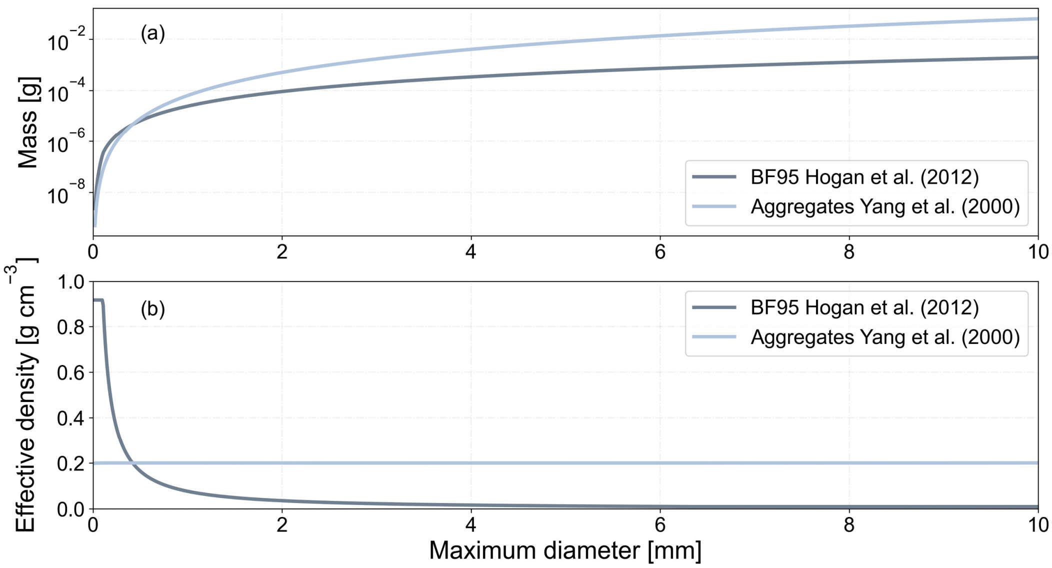

Figure 2.2: (a) Mass and (b) effective density for ice particles with AR=1.67 and the same $D_{\max}$ for BF95 and aggregates mass-size relation.

Particle size distribution

In this thesis, ice particle sizes were assumed to follow the normalized gamma particle size distribution of Bringi and Chandrasekar (2001) with a width parameter $\mu = 0$ (exponential PSD), a typical value for snow aggregates (several studies, e.g., Tiira et al., 2016; Matrosov and Heymsfield, 2017 and many more, suggest also μ values close to 0):

$$N\left(D_{eq}\right) = N_{\mathrm{w}} f(\mu)\left(\frac{D_{eq}}{D_0}\right)^{\mu} e^{\frac{-(3.67+\mu)D_{eq}}{D_0}} \quad \text{with } f(\mu) = \frac{6}{3.67^4}(3.67+\mu)^{\frac{(\mu+4)}{\Gamma(\mu+4)}}, \tag{2.6}$$

where,
N_{w}: the intercept parameter,
μ: the width parameter,
D_0: the median volume diameter,
D_{eq}: the melted-equivalent diameter of the ice particles.

The median volume diameter (D_0) is one of the three parameters used to define the gamma PSD for the scattering simulations and is the size which separates the PSD in half with respect to volume (defined as: $\int_0^{D_0} D^3 N(D)\mathrm{d}D = \frac{1}{2}\int_0^{D_{\mathrm{max\_PSD}}} D^3 N(D)\mathrm{d}D$). However, the use of a median mass diameter is more common in ice studies. The median mass diameter, or equivalent median diameter of ice particles, or simple, D_{m}, is the size that splits the PSD in half with respect to mass (defined as: $\int_0^{D_{\mathrm{m}}} m(D)N(D)\mathrm{d}D = \frac{1}{2}\mathrm{IWC}$, Ding et al., 2020). Although dual-wavelength radar measurements are more suitable to retrieve median size D_0, because D_0 is independent from the effective density of ice particles (e.g., Matrosov, 1998; Hogan et al., 2000), it can be also used to retrieve D_{m} when a suitable mass-size relation is investigated, as D_{m} is significantly affected by the used $\mathrm{m}(D_{\max})$. For instance, Leroy et al. (2016) found that the retrieval of D_{m} is significantly affected by the b exponent of the $\mathrm{m}(D_{\mathrm{max}})$. As one of the goals of this work is to investigate the sensitivity of ice particles median size towards $\mathrm{m}(D_{\mathrm{max}})$, the D_{m} was chosen to vary in the scattering simulations. In Fig. 2.3, an example of the PSD for intercept parameter $N_{\mathrm{w}} = 1\times10^{3}$, width parameter $\mu = 0$ (exponential PSD), different D_{m} values and constant AR = 1.67 is presented, showing how D_{m} and the shape of the PSD are related.

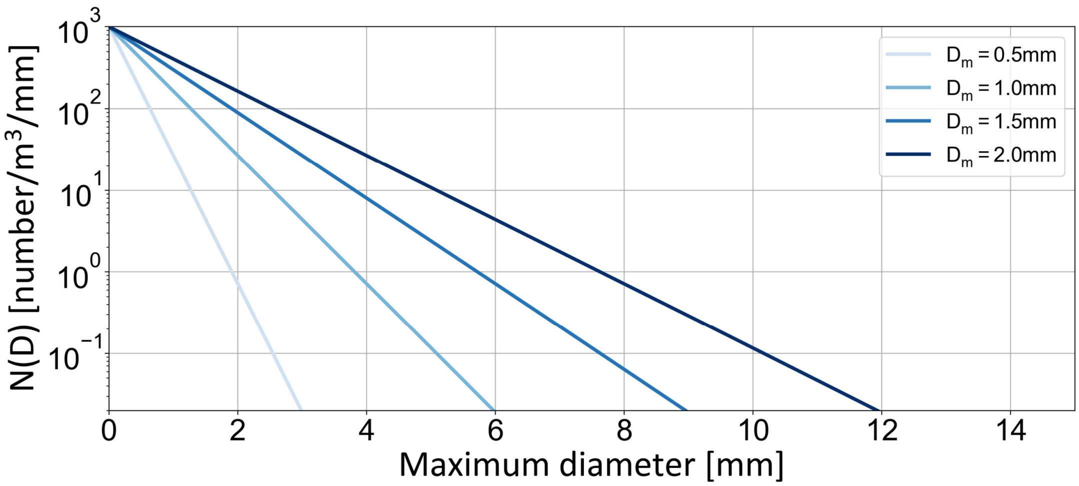

Figure 2.3: PSD for different values of D_{m}, AR = 1.67, $N_{\mathrm{w}} = 1\times10^{3}$, and $\mu = 0$.

Ice water content

Another variable parameterizing populations of ice particles is the ice water content (IWC). The IWC of a particle size distribution describes the total mass of the particles considering their number concentration $N(D)$ and it is calculated using the following formula,

$$\mathrm{IWC} = \int_{D_{\mathrm{min\_PSD}}}^{D_{\mathrm{max\_PSD}}} N(D)m(D)\mathrm{d}D. \tag{2.7}$$

The IWC has been widely used in several retrieval studies along with radar data, e.g., Hogan et al. (2006). In the present thesis, the IWC was varied to study its impact on different radar measurements.

2.2 Principles of electromagnetism for radar applications

Several applications of the everyday life exploit radiation from different parts of electromagnetic spectrum as well as its interaction with the matter. Figure 2.4 shows some examples of such applications. For instance, the widely used radio sensors emit radiation in the section of radio waves, while X-rays can be used to radiograph, e.g., broken bones, in medical applications. The same principles of radiation's interaction with the matter apply when it comes to ice hydrometeor observations using, e.g., a radar beam.

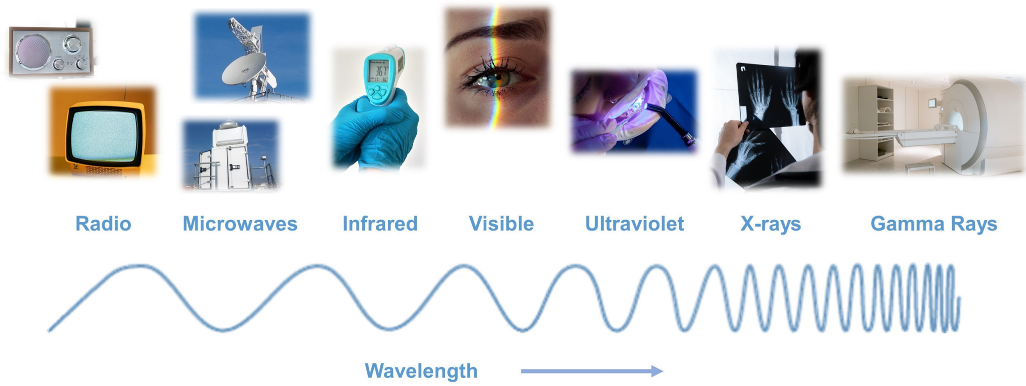

Figure 2.4: Different applications on the electromagnetic spectrum.

Radar instruments emit electromagnetic radiation in the microwave region and they are used for different purposes, e.g., meteorological or military. Depending on the application, different radar bands are used. Some of the radar bands can be found in Table 2.1. The frequency or wavelength of the operation is defined by,

$$c = \lambda f \tag{2.8}$$

where,
c: the speed of light ($c = 3 \cdot 10^8$ m s^{-1}),
λ: the radar wavelength in m,
f: the radar frequency in Hz (1 Hz = 1 s^{-1}).

Table 2.1: Frequency and wavelength at different radar bands.

band	frequency (GHz)	wavelength (mm)
P	0.3–1	1000–300
L	1–2	300–150
S	2–4	150–75
C	4–8	75–37.5
X	8–12	37.5–25
Ku	12–18	25–17
K	18–27	17–11
Ka	27–40	11–7.5
V	40–75	7.5–4
W	75–110	4–2.7

In the framework of the present study, the synergy of two meteorological radars is used. At first, a C-band weather radar which emits at f = 5.504 GHz (λ = 54.5 mm) is a suitable instrument to monitor precipitation systems with larger hydrometeors at a long distance (up to 300 km). In combination to the weather radar, a Ka-band cloud radar emitting at f = 35.2 GHz (λ = 8.5 mm) is more suitable to observe smaller atmospheric hydrometeors in clouds. The way that the emitted radiation from radars interacts with hydrometeors strongly depends on the relation between the radar wavelength and the hydrometeors size. In Fig. 1.5 (Sect. 1.3), different types of scattering, i.e., Rayleigh, Mie, optical geometry, are presented depending on this aforementioned relation. To better illustrate this statement it is easier to consider spherical, e.g., water hydrometeors. Assuming that the diameter of each hydrometeor is larger than the radar wavelength, then its backscattering cross-section, σ_{b_sca}, defined as the area of the target interacting with the incident radiation by scattering backwards at 180° part of the incident waves, is proportional to the second power of its diameter D (Eq. 2.9a). The scattering region where particles interact like so with the incident radiation is known as Mie scattering regime.

$$\sigma_{b\_sca} \sim \pi D^2 \tag{2.9a}$$

When the radar wavelength is much larger than the size of hydrometeors, Rayleigh scattering take place. σ_{b_sca} in this case is found to be proportional to the sixth power of the diameter of the particle, i.e.,

$$\sigma_{b\_sca} = \frac{\pi^5 |K|^2 D^6}{\lambda^4} \tag{2.9b}$$

with $|K|^2 = 0.93$ the dielectric factor related to the complex refractive index, m_{RI}, in the case of water hydrometeors. A visualization of the aforesaid scattering types can be found in Fig. 2.5 where a radar beam is sketched. In the field of view of this beam atmospheric hydrometeors of different sizes are detected. The small – compared to the radar wavelength – hydrometeors are defined as Rayleigh scatterers, while the larger particles are considered to be Mie scatterers.

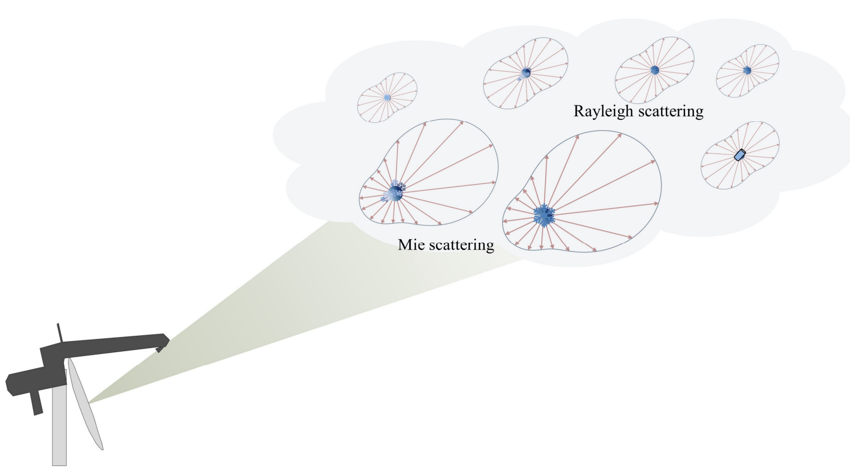

Figure 2.5: Radar field of view and interaction of radar beam with atmospheric hydrometeors.

Besides the size, the effective density and material of hydrometeors has a strong influence on the intensity of the interaction with the radar beam and this is described by the refractive index. For this purpose, the effective medium approximation (EMA) was used to model the refractive index of the composite material as an ice matrix with inclusions of air following the Maxwell-Garnett (MG) mixing formula (Garnett and Larmor, 1904):

$$\frac{e_{\mathrm{eff}}-e_{\mathrm{m}}}{e_{\mathrm{eff}}+2e_{\mathrm{m}}} = f_{\mathrm{i}}\frac{e_{\mathrm{i}}-e_{\mathrm{m}}}{e_{\mathrm{i}}+2e_{m}} \tag{2.10}$$

where,
e_{m}, e_{i}: the permittivities of the medium and the inclusion, respectively,
e_{eff}: the effective permittivity,
f_{i}: the volume fraction of the inclusions.
The complex refractive index, m_{RI}, is then calculated from $m_{\mathrm{RI}} = n - ik = \sqrt{e_{\mathrm{eff}}}$; where *n*, *k* is the real and the imaginary – related to the absorption of the medium – part of the complex refractive index. In the framework of the EMA, the electromagnetic interaction of an inhomogeneous dielectric particle (components with different refractive indices) can be approximated with one effective refractive index of a homogeneous particle (e.g., Liu et al., 2014; Mishchenko et al., 2016). In Liu et al. (2014), internal mixing has been proven to best represent the scattering properties of atmospheric particles. The same work also pointed out that the size parameter $D_{\mathrm{crit}} = \frac{\pi d}{\lambda}$ for each of the inclusions should not be larger than 0.4 (with *d* as the diameter of the inclusion). In the present doctoral study, the refractive index of ice hydrometeors is modelled as an internal mixing of ice and air which are arranged throughout the ice particle.

2.3 Radar basics

This section aims to introduce the most significant radar basics, e.g., radar equation and observables, so that the reader can have an overview about the radar variables used throughout this doctoral thesis.

2.3.1 Radar equation

The power density, I_{iso}, defined as the ratio of transmitted power P_τ by an isotropic source to the area where the energy is transmitted at a distance *r*, is calculated from the following formula,

$$I_{\mathrm{iso}} = \frac{P_\tau}{4\pi r^2}\,. \tag{2.11}$$

On the other hand, the power density, $I_{\mathrm{non-iso}}$, defined as the ratio of transmitted power by a non-isotropic radar antenna with a gain g to the area where the energy is transmitted at a distance *r*, is calculated from:

$$I_{\text{non-iso}} = \frac{P_\tau g}{4\pi r^2}\,. \tag{2.12}$$

A point-target with an area A_{target}, detected at a distance r from the radar antenna, intercepts the power of the antenna beam according,

$$P_{\text{target}} = \frac{P_\tau g A_{\text{target}}}{4\pi r^2}\,. \tag{2.13}$$

If the aforementioned point-target interacts with the radiation transmitted by the radar, part of the energy returns back to the antenna. This amount of the detected/received energy, P_{r}, is calculated from,

$$P_{\text{r}} = \frac{P_{\text{target}} A_{\text{eff}}}{4\pi r^2} = \frac{P_\tau g A_{\text{target}} A_{\text{eff}}}{(4\pi)^2 r^4} \tag{2.14}$$

where,
A_{eff}: the effective area of the radar antenna receiving the returned signal. Assuming $A_{\text{eff}} = \frac{g\lambda^2}{4\pi}$ and A_{target} the backscattering cross-section, σ_{b_sca}, of the detected target, Eq. (2.14) becomes,

$$P_{\text{r}} = \frac{P_{\text{target}} A_{\text{eff}}}{4\pi r^2} = \frac{P_\tau A_{\text{target}} g^2 \lambda^2}{(4\pi)^3 r^4} = \frac{P_\tau \sigma_{b\_sca} g^2 \lambda^2}{(4\pi)^3 r^4}. \tag{2.15}$$

In reality, meteorological radars perform pointed measurements of a whole volume V. Figure 2.6 demonstrates how this measured volume can be visualized. Equation (2.16) shows how it can be calculated considering only the signal returned to the antenna during half of a radar pulse.

$$V = \pi \frac{c\tau}{2} \frac{r\theta}{2} \frac{r\varphi}{2} \tag{2.16}$$

where,
τ: the duration of the radar pulse,
θ, φ: the horizontal and vertical radar beam width, respectively.
Assuming a Gaussian shape for the radar beam pattern, only the $\frac{1}{2ln(2)}$ of the radiation of the beam passes through the aforementioned volume V. Moreover, not only one but a number of targets are detected in this volume, adding up to a total backscattering cross-section, $\sigma = \sum_{vol} \sigma_{b\_sca}$. Hence, multiplying Eq. (2.15) with $\frac{1}{2ln(2)}$ and replacing the σ_{b_sca} with σ, the received signal becomes,

$$P_r = \frac{P_\tau g^2 \lambda^2 \theta \varphi c\tau}{1024 ln(2) \pi^2 r^2} \sigma. \tag{2.17}$$

The $\sum_{vol} \sigma_{b\_sca}$ which is normalized to a specific volume is also referred as radar reflectivity η, presented also in Sect. 2.3.2.

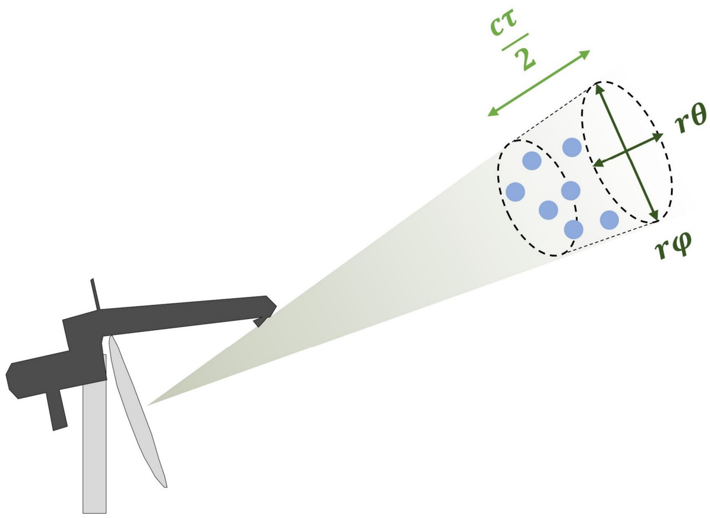

Figure 2.6: Measured volume by radar during a radar pulse. With $\frac{c\tau}{2}$ the radar range resolution is calculated.

2.3.2 Radar variables

Depending not only on the required hardware but also on the envisioned application, radars can provide different observables. Vertically pointing radars are, for instance, ideal for Doppler measurements and thus, can provide effective density information of atmospheric hydrometeors. Scanning radars can perform valuable polarimetric measurements which are beneficial to retrieve shape or orientation information of the detected hydrometeors. This information can be obtained by exploiting the different polarizations (horizontal, vertical, circular) of the emitted radiation. In this section, all radar variables used in the present doctoral thesis are described. Information of these variables can be found in, e.g., Matrosov (1998), Straka et al. (2000) and Kumjian (2013).

Radar reflectivity factor *Z*

The radar reflectivity factor *z* provides information about the backscattered signal (signal scattered at 180° with respect to the direction of the incident radiation) of the atmospheric hydrometeors. This parameter is designed to be proportional to the Rayleigh scattering cross section of small liquid spheres, which are much smaller than the radar wavelength:

$$z\ [\mathrm{mm}^6\ \mathrm{m}^{-3}] = \int_0^\infty N(D) D^6 \mathrm{d}D \tag{2.18a}$$

where,
z: the radar reflectivity in linear scale,
$N(D)$: the number concentration,
D: the geometric diameter of the particles in mm.

This formula can be also expressed in logarithmic terms:

$$Z\ [\mathrm{dBZ}] = 10\log_{10}\left(\frac{z}{1\ mm^6 m^{-3}}\right). \tag{2.18b}$$

The aforementioned definition, however, cannot be directly applied to snow due to the varying density, the irregular shape and larger size of ice particles which cause deviations from the Rayleigh into the Mie scattering regime. Nevertheless, an equivalent radar reflectivity factor Z_e can be derived from the measured radar reflectivity η when the dielectric factor of water $|K|^2 = 0.93$ is assumed:

$$z_\mathrm{e}\ [\mathrm{mm}^6\ \mathrm{m}^{-3}] = \eta \frac{\lambda^4}{\pi^5|K|^2} \text{ and } Z_\mathrm{e}\ [\mathrm{dBZ}] = 10\log_{10}\left(\frac{z_e}{1\ mm^6 m^{-3}}\right) \tag{2.18c}$$

In the Rayleigh regime, the radar reflectivity factor Z or the equivalent radar reflectivity factor Z_e (for simplicity reasons referred also as radar reflectivity here) is proportional to the sixth power of the particle size, while in the Mie regime Z_e scales with the second power of the particle size. In both regimes Z_e scales linearly with the particle number concentration.

Dual-wavelength ratio DWR

Using the ratio of radar reflectivities at two different radar wavelengths (Eq. 2.19; dual-wavelength ratio, DWR), size information about hydrometeors observed within the radar beams can be inferred. This parameter increases with the particle size when the shorter radar wavelength is equal or shorter than the particle size:

$$\mathrm{DWR}_{\lambda1,\lambda2}\ [\mathrm{dB}] = 10\log_{10}\left(\frac{z_{\mathrm{e},\lambda1}}{z_{\mathrm{e},\lambda2}}\right) \text{ or } \mathrm{DWR}_{\lambda1,\lambda2}\ [\mathrm{dB}] = Z_{\mathrm{e},\lambda1}\ [\mathrm{dBZ}] - Z_{\mathrm{e},\lambda2}\ [\mathrm{dBZ}]. \tag{2.19}$$

In Eq. (2.19), $\lambda_1 > \lambda_2$ are the two radar wavelengths, $z_{e,\lambda1}$, $z_{e,\lambda2}$ the radar reflectivities at the two radar wavelengths in linear scale (units: $\mathrm{mm}^6\ \mathrm{m}^{-3}$) and $Z_{e,\lambda1}$, $Z_{e,\lambda2}$ the radar reflectivities in logarithmic scale (units: dBZ)

Differential radar reflectivity ZDR

One prominent polarimetric parameter in ice microphysics studies is the differential radar reflectivity, ZDR, a parameter which is defined as:

$$\mathrm{ZDR}\ [\mathrm{dB}] = 10\log_{10}\left(\frac{z_{\mathrm{HH}}}{z_{VV}}\right) \text{ or } \mathrm{ZDR}\ [\mathrm{dB}] = Z_{\mathrm{HH}}\ [\mathrm{dBZ}] - Z_{\mathrm{VV}}\ [\mathrm{dBZ}] \tag{2.20}$$

where,
z_{HH}, z_{VV} the linear reflectivity factor at horizontal and vertical polarization, when the radar transmits and receives horizontally and vertically polarized signal, respectively. Z_{HH}, Z_{VV} are the logarithmic reflectivity factor at horizontal and vertical polarization, also when the radar transmits horizontally and vertically polarized signal, respectively.

This radar variable can provide shape or orientation information and following its definition, it is found to be zero if the received signal in both polarization channels is the same, i.e., for spherical targets. For elongated, azimuthally oriented particles ZDR is found to be greater (horizontally aligned particles) or less than zero (vertically aligned particles), always depending on the orientation of their rotational axis to the horizontal plane (e.g., Straka et al., 2000). Figure 2.7 demonstrates in detail how ZDR is calculated for oblates and horizontally aligned prolate ice particles.

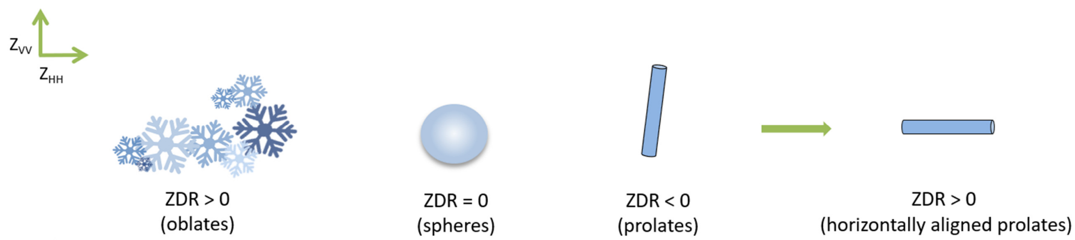

Figure 2.7: Definition of ZDR for oblates, spheres and horizontally aligned prolate ice particles.

Linear depolarization ratio LDR

Another polarimetric radar variable which provides information about hydrometeors shape is the linear depolarization ratio, LDR. The LDR is also used to distinguish between ice and water hydrometeors and it is defined as,

$$\mathrm{LDR}\ [\mathrm{dB}] = 10\log_{10}\left(\frac{z_{\mathrm{HV}}}{z_{\mathrm{HH}}}\right) \tag{2.21}$$

where,

z_{VH}, z_{HH} the linear reflectivity factor at the vertical and horizontal polarization channel, respectively. LDR is the vertically received signal of a horizontally polarized pulse. This definition indicates that spherical hydrometeors have theoretically LDR which approaches $-\infty$. However, due to antenna depolarization measured LDR is found to be finite, e.g., Myagkov et al. (2015) for spheres.

Cross-correlation coefficient ρ_{HV}

The radar cross-correlation coefficient ρ_{HV} is a parameter which describes the correlation between the horizontally and vertically polarized received radar signals. While consecutive pulses are very similar in the horizontal and vertical channel for spherical particles, this correlation can be influenced by tumbling and aspherical hydrometeors. Therefore, it is a variable that provides information about hydrometeors sphericity.

$$\rho_{\mathrm{HV}} = \frac{\langle S_{\mathrm{VV}} S_{\mathrm{HH}}^{*} \rangle}{\langle |S_{\mathrm{HH}}|^2 \rangle^{1/2} \langle |S_{\mathrm{VV}}|^2 \rangle^{1/2}} \tag{2.22}$$

where,
S_{VV}, S_{HH} the scattering amplitudes of the received signal at the vertical or horizontal channel originated from vertically or horizontally polarized emitted signal – depending on the subscripts. From the aforementioned definition, ρ_{HV} is expected to be 1 for spheres. For water hydrometeors ρ_{HV} ranges between 0.97–0.99 while, for ice hydrometeors it ranges from 0.75–0.95.

Chapter 3

3 Methods

This section contains work, which has already been published by Tetoni et al. (2022) in Atmospheric Measurement Techniques (AMT), entitled *"Retrievals of ice microphysical properties using dual-wavelength polarimetric radar observations during stratiform precipitation events"*.

In this study, the potential to combine two spatially separated radars to obtain DWR and ZDR observations for size, shape and mass retrievals of ice particles and aggregates, detected into clouds and above the melting layer, was investigated. The ice microphysics retrieval is developed by combining the radar measurements with ice scattering simulations and it resolves the ice water content, the median size and the apparent shape of the detected ice particles. The apparent shape – for simplicity the term shape will be used throughout this doctoral thesis – is described by the average observed aspect ratio which is strongly connected to the orientation of ice particles including their horizontal flutter. This study was conducted in the scope of the Priority Program "Fusion of Radar Polarimetry and Numerical Atmospheric Modelling Towards an Improved Understanding of Cloud and Precipitation Processes" also known as "Polarimetric Radar Observations meet Atmospheric Modelling" (PROM; Trömel et al., 2021), funded by the German Research Foundation (DFG) and especially, in the framework of the "Investigation of the initiation of convection and the evolution of precipitation using simulations and polarimetric radar observations at C- and Ka-band" (IcePolCKa) project with grant no. HA 3314/9-1. The measurement dataset was collected using measurements from a scanning cloud radar and a weather radar, located 23 km away, during precipitation events in winter 2019. As the average wind direction in the Munich area is almost aligned to the radars cross-section, the evolution of precipitation and the development of fall streaks inside the clouds was monitored by performing continuous Range-Height-Indicator (RHI; fixed azimuth angle with the radar scanning at different elevation angles) scans according to the precipitation rate. Since the aim was to use DWR and ZDR measurements from two different locations, case studies with quite homogeneous cloud scenes, in which hydrometeor attenuation can be considered negligible, were investigated. Therefore, cloud cross-sections of cloud scenes with stratiform snowfall that reached the ground, and with air temperatures below freezing at the surface, were selected. To exclude liquid hydrometeors and melting layers, an ice mask was developed and applied to the observational dataset. Wet particles were considered to be out of scope in this work, but should be included in future studies to improve the representation of melting and riming processes in numerical weather models as well. In this chapter, all methods used in the present thesis will be demonstrated in detail. Using example plots the reader will be given a whole picture about the aim of this study. At first, the instruments used to collect the radar observations as well as the measurement dataset, along with the filters/errors applied to collect only high-quality ice hydrometeors observations, will be described in depth. Moreover, the error assessment of the measurements will be analyzed, and the methods used in the scattering simulations of ice particles will be presented. Finally, the way that the ice microphysics retrieval is developed will be presented in detail.

3.1 Radar instruments

For the DWR dataset used in this study the synergy of two polarimetric radars, the C-band POLDIRAD weather radar at German Aerospace Center (DLR) in Oberpfaffenhofen and the Ka-band MIRA-35 cloud radar at Ludwig Maximilians University of Munich (LMU) in Munich, was exploited. POLDIRAD and MIRA-35 performed coordinated RHI scans towards each other (constant azimuth angle for both radars) at a distance of 23 km between DLR and LMU, monitoring stratiform precipitation events. Within the framework of IcePolCKa project, another measurement strategy included sector range-height-indicator (S-RHI) scans using POLDIRAD and MIRA-35 to monitor precipitation cells during convection. In this way, a first scan was executed towards the cell of interest at a specific azimuth. Then, two additional fast RHI scans were executed from each radar deviated ±2° from the initial azimuth. This approach can result nine vertical profiles within the precipitation cell providing additional microphysical information (Köcher et al., 2022, their Fig. 1). In this doctoral thesis, only single coordinated RHI radar measurements were used as the aim was to focus on snowfall cases, in which the attenuation of the radar signal due to hydrometeors is not strong and which are simpler case studies for the development of the first version of the ice microphysics retrieval.

POLDIRAD

POLDIRAD (Fig. 3.1, left) is a polarization diversity Doppler weather radar operating at C band with a frequency of 5.504 GHz (λ = 54.5 mm, λ_1 in Eq. 2.19). The radar is located at DLR in Oberpfaffenhofen, 23 km southwest of Munich, at 48° 05' 12" N and 11° 16' 45" E at an altitude of 602.5 m above mean sea level (MSL). Since 1986, POLDIRAD has been operated on the roof of Institute of Atmospheric Physics (IPA), DLR for meteorological research purposes (Schroth et al., 1988). The weather radar consists of a parabolic antenna with a diameter of 4.5 m and a circular beam width of 1°. A magnetron transmitter with a power peak of 400 kW and a Selex ES Germatronik GDRX digital receiver with both linear and logarithmic response are synchronized with the polarization network of the receiver, which can record the linear, elliptic and circular polarization of each radar pulse (Reimann and Hagen, 2016). POLDIRAD has the capability to receive the co- and cross-polar components of the horizontal, vertical, circular and elliptical polarized transmitted electromagnetic waves. In this way it provides several polarimetric variables, e.g., ZDR, which can be used to obtain additional information about the size, shape, phase, and falling behavior of the hydrometeors in the atmosphere (Steinert and Chandra, 2009; Straka et al., 2000). In the present doctoral study ZDR from POLDIRAD was used to constrain the shape of the detected ice hydrometeors. Depending on the operational mode of POLDIRAD, the maximum range that can be reached is approximately 300 km (for a pulse repetition frequency of 400 Hz, a pulse duration of 2 μs and a range resolution of 300 m), making it a suitable instrument for nowcasting in the surrounding area of Munich. For the present study the maximum range of POLDIRAD was 130 km with a pulse repetition frequency of 1150 Hz, a pulse duration of 1 μs and a range resolution of 150

m. The system can be operated in the STAR mode (simultaneous transmission and reception). Here, the alternate-HV mode (alternate horizontally and vertically polarized transmitted electromagnetic waves), which allows measuring the cross-polar components of the backscatter matrix, was used. The elevation velocity during the RHI scans was 1° s^{-1}. The technical characteristics of POLDIRAD are presented in Table 3.1.

Figure 3.1: C-band POLDIRAD weather radar (left, photo: Dr. Martin Hagen) and Ka-band MIRA-35 cloud radar (right, photo: Prof. Dr. Bernhard Mayer).

Table 3.1: POLDIRAD and MIRA-35 technical characteristics.

Parameter	POLDIRAD	MIRA-35
frequency/wavelength	5.5 GHz/ 54.5 mm	35.2 GHz/ 8.5 mm
peak transmitted power	400 kW	30 kW
antenna diameter	4.5 m diameter	1 m diameter
beam width	1.0º	0.6º
transmit mode	pulse duration: 1 µs pulse repetition frequency: 1150 Hz max. range: 130 km range resolution: 150 m	pulse duration: 0.2 µs pulse repetition frequency: 5000 Hz max. range: 24 km range resolution: 30 m

MIRA-35

MIRA-35 (Fig. 3.1, right) is a Ka-band scanning Doppler cloud radar developed by Metek (Meteorologische Messtechnik GmbH, Elmshorn, Germany) with a frequency of ca. 35.2 GHz and a wavelength $\lambda = 8.5$ mm (Görsdorf et al., 2015), which is λ_2 in Eq. (2.19). The cloud radar, which is operated by the Meteorological Institute Munich (MIM) as part of the Munich Aerosol Cloud Scanner (MACS) project (also referred as miraMACS, Ewald et al., 2015), is located on the roof of the institute at the LMU at 48° 08' 52.2" N and 11° 34' 24.2" E and 541 m above

MSL. The transmitter consists of a magnetron with a power peak of 30 kW which typically transmits radar pulses of 0.2 μs with a pulse repetition frequency of 5 kHz, corresponding to a range resolution of 30 m. The 1 m diameter antenna dish produces a beam width of 0.6°. The MIRA-35 cloud radar emits horizontally polarized radiation and measures both vertical and horizontal components of the backscattered wave. Hence, it has the capability to perform LDR measurements. The cloud radar usually points to the zenith, but can also perform RHI scans at different azimuths with elevation velocity 4° s^{-1} and Plan-Position-Indicator (PPI) scans at different elevations angles (executed for constant elevation angle and with the radar rotating). The technical characteristics of MIRA-35 are presented in Table 3.1.

3.1.1 Measurements

Coordinated RHI measurements with POLDIRAD and MIRA-35 had been collected during monitored snowfall events, with some ice particles reaching the ground where both radars are located (602.5 m for POLDIRAD and 541 m for MIRA-35, both heights above MSL). However, only ice particles above the melting layer were investigated in the present study. RHI scans were executed from the two radars at almost the same time with a temporal resolution which was adjusted to the precipitation rate. POLDIRAD scanned between 0°–35° elevation towards MIRA-35 (northeast direction, azimuth of 73°), while MIRA-35 scanned between 0°–90° elevation towards POLDIRAD (southwest direction, azimuth of 253°) as well as 90°–169° elevation in a backward northeast direction but still inside the common cross-section (Fig. 3.2). With this setup, the cross-section between the two radars as well as beyond the MIRA-35 position was fully covered to record the development and microphysics of precipitation cells and fall streaks. During snowfall cases, Z_e measurements from the two radars were performed and interpolated onto a common rectangular grid (50 m × 50 m) using the nearest neighbor interpolation method. The 0-height of this grid was defined to be the height above MSL. In this section, a case study from 30 January 2019 when a snowfall event took place over the Munich area will be presented to demonstrate the methodology. At 04:00 UTC of that night, an ice cloud started forming at an altitude of 9 km. During the time of the coordinated measurements the vertical extension of the cloud was up to 7 km. Throughout that day, the ambient temperature was mostly below 0°. The wind speed at the surface was very low, while at higher altitudes exceeded 15 m s^{-1} at some cases. The vertical gradient of the wind favored the development of fall streaks (shown in the radar observations in Fig. 3.3) and thus, ice particle growth within the ice cloud. In Fig. 3.3a and 3.3c, the measured Z_e from the two radar systems during the RHI scans from 30 January 2019 at 10:08 UTC is presented. For the MIRA-35 Z_e measurements a calibration offset of 4 dBZ was applied, as derived in Ewald et al. (2019). Studying only snow cases no strong effects of hydrometeor attenuation are expected (e.g., Nishikawa et al., 2016). However, an iterative method to estimate hydrometeor attenuation has been developed. Additionally, both Z_e datasets were corrected for gaseous attenuation using the ITU-R P.676-12 formulas provided by the International Telecommunication Union (ITU) in August 2019 (ITU-R P.676-12, 2019). Both attenuation correction methods are fully described in Sect. 3.1.4 and 3.3.1. After the interpolation of both radar reflectivities in the common radar grid, the DWR was calculated (Fig. 3.3b) using Eq. (2.19). Since DWR is defined as the ratio of Z_e at two wavelengths, it is independent of number concentration $N(D)$. Therefore, it exploits the difference in the received radar signal due to Mie effects to give size information. To avoid unwanted biases by measurement artefacts, DWR values lower than –5 dB and higher than 20 dB were excluded. Furthermore, errors from other sources, e.g., beam width mismatch effects (beam width 1º for POLDIRAD and 0.6º for MIRA-35), were analyzed (fully explained in Sect. 3.1.3). Besides DWR measurements, polarimetric observations were used to study the shape of ice particles. POLDIRAD provided polarimetric measurements of ZDR, but only ZDR values between –1 dB and 7 dB were considered to be atmospheric hydrometeors signatures. The ZDR calibration was validated using additional measurements (also described in detail in Sect. 3.1.3). For the ZDR panel (Fig. 3.3d), reasonable boundaries for optimal visualization purposes were used in the colormap. When Z_e, ZDR and DWR measurements are combined (Fig. 3.3), one can already get a first glimpse on the prevalent ice microphysics. Especially below 3 km height, between 20–30 km from POLDIRAD, the large values of Z_e accompanied with the large values of DWR (greater than 5 dB) and the low values of ZDR (lower than 1 dB) indicate the presence of large and quite spherical ice particles. In the following, quantitative ice microphysics will be revealed by the combination of Z_e, DWR and ZDR measurements with scattering simulations for a variety of ice particles.

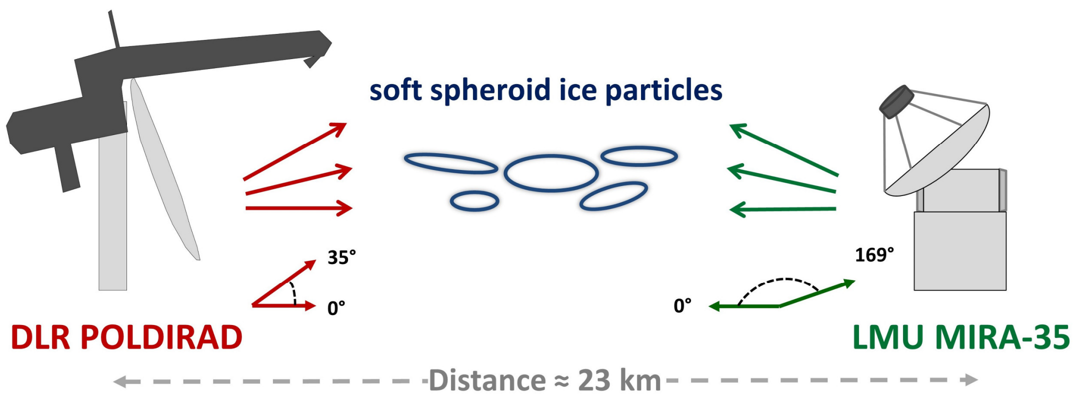

Figure 3.2: Geometry of the radar setup. The range of elevation angles is 0°–35° and 0°–169° for POLDIRAD and MIRA-35, respectively.

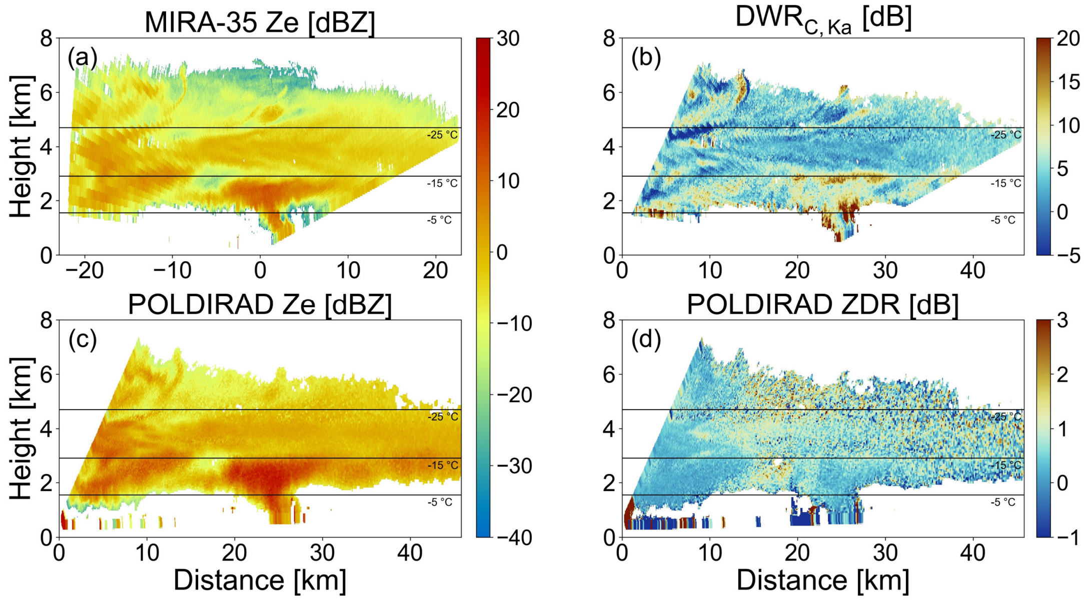

Figure 3.3: Radar observations of (a, c) MIRA-35 and POLDIRAD Z_e, (b) DWR and (d) POLDIRAD ZDR from 30 January 2019 at 10:08 UTC. The –5 ºC, –15 ºC and –25 ºC temperature levels are plotted with black solid lines (source: Deutscher Wetterdienst, data provided by University of Wyoming; http://weather.uwyo.edu/upperair/sounding.html, last access: 08 April 2022).

3.1.2 Ice mask application on measurements

As already mentioned, this study aims to retrieve microphysical information for ice particles that are detected only into clouds and above melting layer, ML. Hence, radar measurements were filtered accordingly and an ice mask was applied. The implementation of the ice mask was achieved using thresholds from polarimetric radar variables, i.e., MIRA-35 LDR, POLDIRAD ZDR and ρHV, as well as temperature sounding data (shown in Fig. 3.4).

For the ice mask implementation, variables from both radars, i.e., the LDR from MIRA-35 as well as the ZDR and ρHV from POLDIRAD, were used. These variables are known to have distinct polarimetric signatures when a ML is present. The mask was applied to each vertical profile of the common grid for every pair of RHI scans. Below 4 km, a ML is detected for the following condition: MIRA-35 LDR is in the range –22 dB ≤ LDR ≤ –15 dB and POLDIRAD ρHV as well as ZDR are in the range 0.75 ≤ ρHV ≤ 0.95 and 1.5 dB ≤ ZDR ≤ 2.5 dB respectively. As this study merely focused on stratiform snowfall precipitation cases and as it was assumed that riming or melting ice is unlikely to occur, all hydrometeors above 4 km (height above MSL) and/or above ML were accounted dry. When the polarimetric criteria were not met, the isotherm of 0 ºC was used as an auxiliary information for ice above that height. The temperature data were obtained from the Oberschleißheim sounding station (about 13 km north of Munich, source: Deutscher Wetterdienst, data provided by University of Wyoming; http://weather.uwyo.edu/upperair/sounding.html, last access: 08 April 2022). Although the thresholds used in the ice mask were evaluated in precipitation cases where a ML was observed, it is required either to investigate more precipitation cases obtaining more precise thresholds (this topic was not in the scope of this study), or to use already established ML detection algorithms exploiting polarimetric radar observations, e.g., Wolfensberger et al. (2016).

The necessity of sharpening the thresholds of the ice mask is highlighted from Fig. 3.5 where an example of ZDR observations during a thunderstorm observed over Munich on 7 July 2019 is presented. Figure 3.5a shows ZDR without the application of any filters, while in Fig. 3.5b the filtered and masked ZDR is plotted. Figure 3.5c presents the origin of the masked ZDR values. On 7 July 2019 at 08:22 UTC a melting layer was observed at 3 km and thus, ZDR was masked for ice hydrometeors at that height. However, the greater part of the cloud cross-section was masked using the 0 ºC isotherm revealing the need for more precise ice thresholds with evaluating more case studies with mixed-phase cloud cross-sections. In the investigated case studies of this thesis, an ML was never detected and only a very small part of the cloud cross-section was masked using the 0 ºC isotherm.

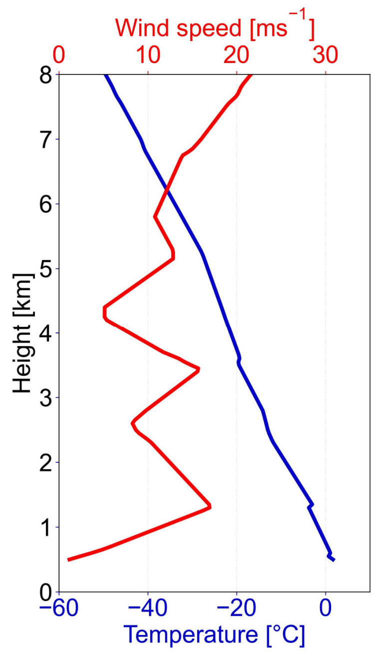

Figure 3.4: Temperature and wind speed data from Oberschleißheim sounding station (source: Deutscher Wetterdienst, data provided by University of Wyoming; http://weather.uwyo.edu/upperair/sounding.html, last access: 08 April 2022) for 30 January 2019 at 12:00 UTC are presented.

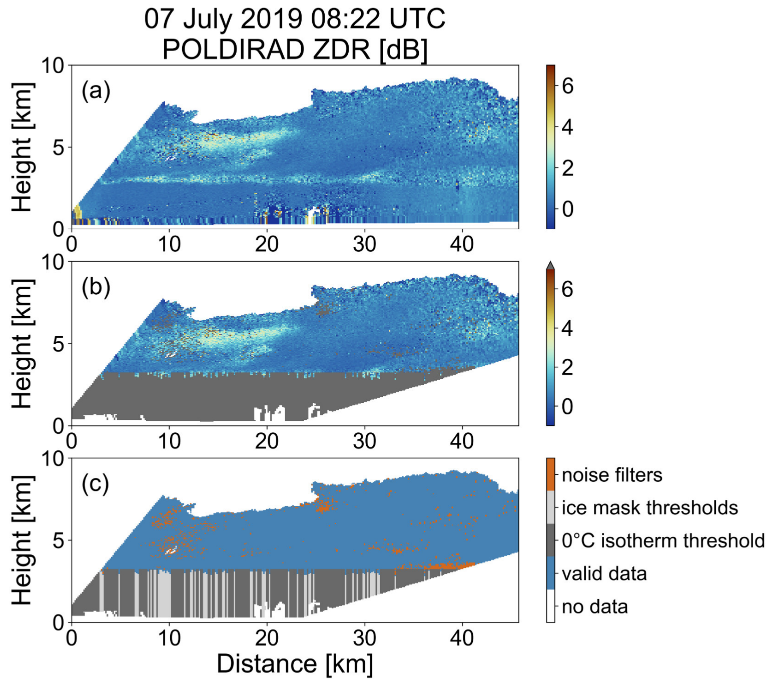

Figure 3.5: (a) Unfiltered POLDIRAD ZDR measurements from 7 July 2019 at 08:22 UTC. (b) Noise filtered and ice masked values of POLDIRAD ZDR plotted with grey color. (c) Different origin of filtered and masked values.

3.1.3 Measurements error assessment

Radar measurements are often affected by systematic or random errors. To assess their impact on the ice microphysics retrieval developed in this study, possible errors in POLDIRAD and MIRA-35 observations, as well as all their sources, were investigated.

The absolute radiometric calibration of both instruments is an important error source in DWR measurements. While the error of the absolute radiometric calibration of POLDIRAD was estimated to be ±0.5 dB following the validation with an external device (Reimann, 2013), the budget laboratory calibration of MIRA-35 following Ewald et al. (2019) was estimated to be ±1.0 dB.

In order to test for a systematic ZDR bias, POLDIRAD measurements during vertically pointing scans (e.g., Gorgucci et al., 1999, also known as birdbath scans), in a liquid cloud layer performed on the 4 April 2019, were exploited. The measurements indicated that ZDR had an offset of about +0.15 dB as ZDR values were expected to be near 0 dB for this case due to the spherical apparent shape of liquid droplets. Although the examined calibration study from the 4 April 2019 was conducted three months later, this ZDR offset was considered to be reliable since calibration efforts showed similar values over the past years. Recent studies (Ryzhkov et al., 2005; Frech and Hubbert, 2020; Ferrone and Berne, 2021) have confirmed the stability of ZDR offsets for long time periods as long as the integrity of the antenna is maintained and wet radome effects are avoided. In Fig. 3.6, examples of radar reflectivity Z_e, differential reflectivity ZDR as well as a scatter plot showing the ZDR offset are presented.

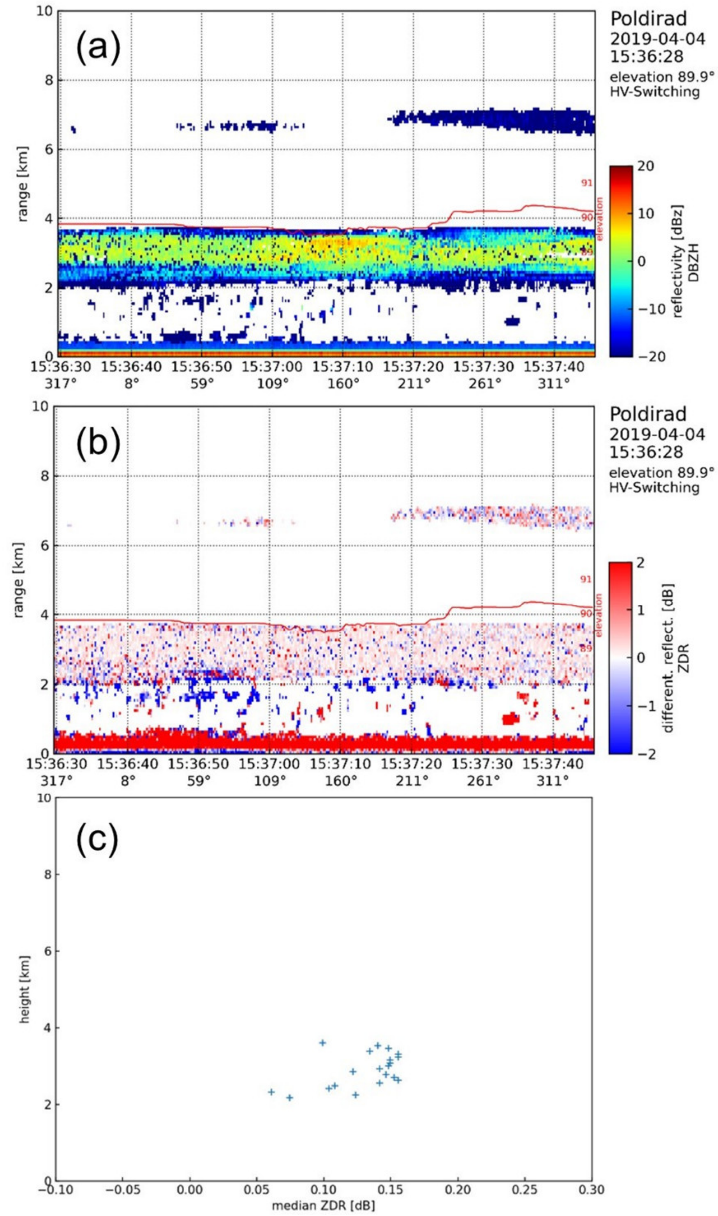

Figure 3.6: POLDIRAD (a) Z_e, and (b) ZDR measurements of a liquid cloud layer for different times and azimuth angles with a vertical pointing antenna on 4 April 2019. Panel (c) shows the offset of the averaged ZDR for the range where the liquid layer was detected.

To further ensure the stability of ZDR bias, an additional calibration validation was conducted following the Ryzhkov and Zrnic (2019) approach (described in their Sect. 6.2.4). The measurement dataset from January 2019 was filtered for large Z_e regions and intermediate temperatures for dry and large aggregates. This analysis yielded a median ZDR = 0.2 dB for these areas, where ice aggregates were expected, indicating that POLDIRAD was well calibrated during the period of this study. In Fig. 3.7, histograms of the ZDR measurements with and without the calibration correction are plotted.

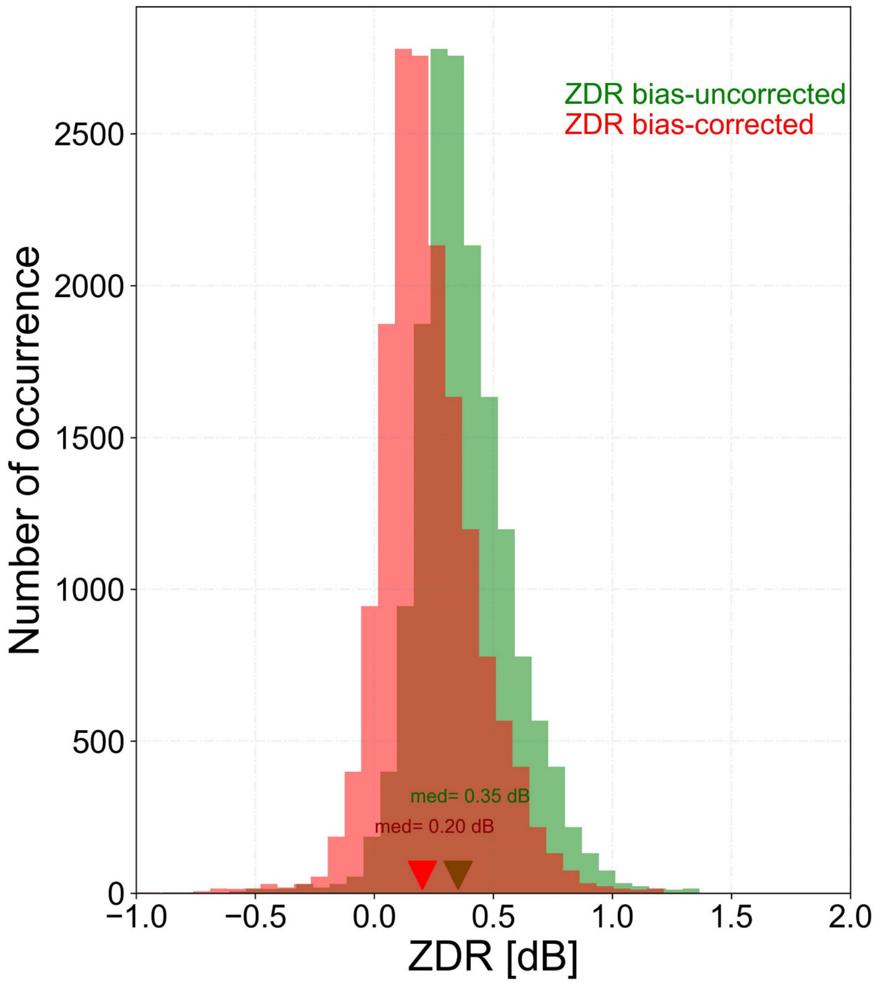

Figure 3.7: ZDR calibration validation for the period of this study following the Ryzhkov and Zrnic (2019) approach for dry aggregates with more relaxed Z_e ($Z_e > 20$ dBZ) and temperature (-20 °C < T < -7 °C) thresholds. With red and green color the histograms for corrected and uncorrected ZDR values, with respect to the ZDR bias as calculated on April 2019, are plotted.

Another error that should be considered is the random error, especially for ZDR measurements at low signal levels. To detect and filter out regions with high ZDR noise the local (3 range gates) standard deviation ZDR_{stdv} was compared with the local mean ZDR_{mean}. Subsequently, regions where the signal ZDR_{mean} exceeded the noise ZDR_{stdv} by one order of magnitude were considered for analysis. An example of this approach can be found in Fig. 3.8. While the retrieval was applied to all cloud regions, the described ice mask and noise filters were used during the statistical aggregation of retrieval results.

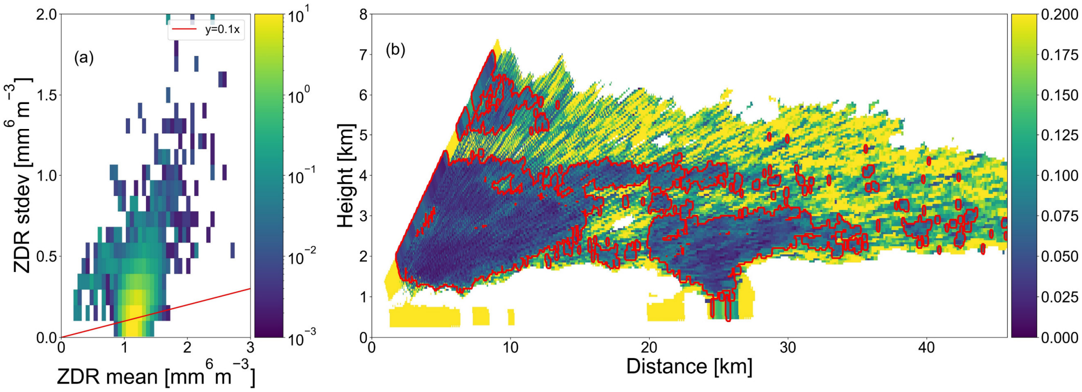

Figure 3.8: (a) The local standard deviation of ZDR is plotted as a function the local mean of ZDR using a 2D density histogram of the calculated parameters (colorbar indicates the density values). (b) The ratio $a_{ZDR} = ZDR_{stdev} / ZDR_{mean}$ can be used to filter out noisy ZDR measurements (values of ZDR are indicated with the corresponding colorbar). In the red encircled areas ($a_{ZDR} < 0.1$), the retrieval results are considered to be reliable enough to be aggregated into statistical results.

When combining spatially separated radar instruments, an azimuthal misalignment between both instruments had to be excluded to obtain meaningful DWR measurements. To this end, several solar scans (e.g., Reimann and Hagen, 2016) were performed with both instruments in spring 2019 to confirm their azimuthal pointing accuracy. Here, an azimuth offset of –0.2° for POLDIRAD and an azimuth offset of +0.1° for MIRA-35 was found. Consecutive solar scans confirmed the azimuthal pointing accuracy within ±0.1°. Despite the small azimuthal misalignment, the radar beam centroids of both instruments were clearly within the respective other beam width during the measurement period in 2019.

Besides an azimuthal misalignment, the temporal mismatch between both RHIs as well as the volumetric mismatch in the context of non-uniform beam filling were also investigated. Although the RHIs from the radars were scheduled to be executed simultaneously, regions during the RHIs were measured at slightly different times by both instruments. This temporal mismatch can lead to slightly different Z_e radar observations from both radars in the context of horizontal advection of an inhomogeneous cloud scene. In the following, this temporal mismatch was used to estimate the resulting DWR error for the example case shown in Fig. 3.3. Using wind data (Fig. 3.4) from the Oberschleißheim sounding station (source: Deutscher Wetterdienst, data provided by University of Wyoming; http://weather.uwyo.edu/upperair/sounding.html, last access: 08 April 2022), the temporal mismatch (Fig. 3.9a) was converted between the radar measurements for each pixel in the common radar grid to a spatial difference (Fig. 3.9c). To estimate the impact of this spatiotemporal mismatch (hereafter spatiotemporal error), spatial differences were used to calculate DWR error between pixels in the spatially higher resolved MIRA-35 Z_e measurements (Fig. 3.9e). Concluding the DWR error assessment, the volumetric mismatch caused by the different beam widths of the two radars was analyzed. For spatially heterogeneous scenes, this volumetric mismatch can lead to artificial DWR signatures caused by a non-uniform beam filling. Here, the spatially higher resolved MIRA-35 Z_e measurements (30 m range gate length) along the RHI cross section were used as a proxy to obtain the spatial heterogeneity of Z_e perpendicular to the RHI cross section. In a first step, the local beam diameters for each pixel in the common grid were calculated for POLDIRAD (Fig. 3.9b) and MIRA-35 (Fig. 3.9d).

Then, moving averages along the Z_e cross sections from MIRA-35 were performed using the corresponding local beam diameters. Hence, at each pixel of the common radar grid two averaged MIRA-35 Z_e values were obtained; one corresponding to the local beam diameter of MIRA-35 and one corresponding to the local beam diameter of POLDIRAD. Subtracting the averaged Z_e for each pixel, the estimation of the error caused by the volumetric mismatch between both radar beams (Fig. 3.9f) was possible.

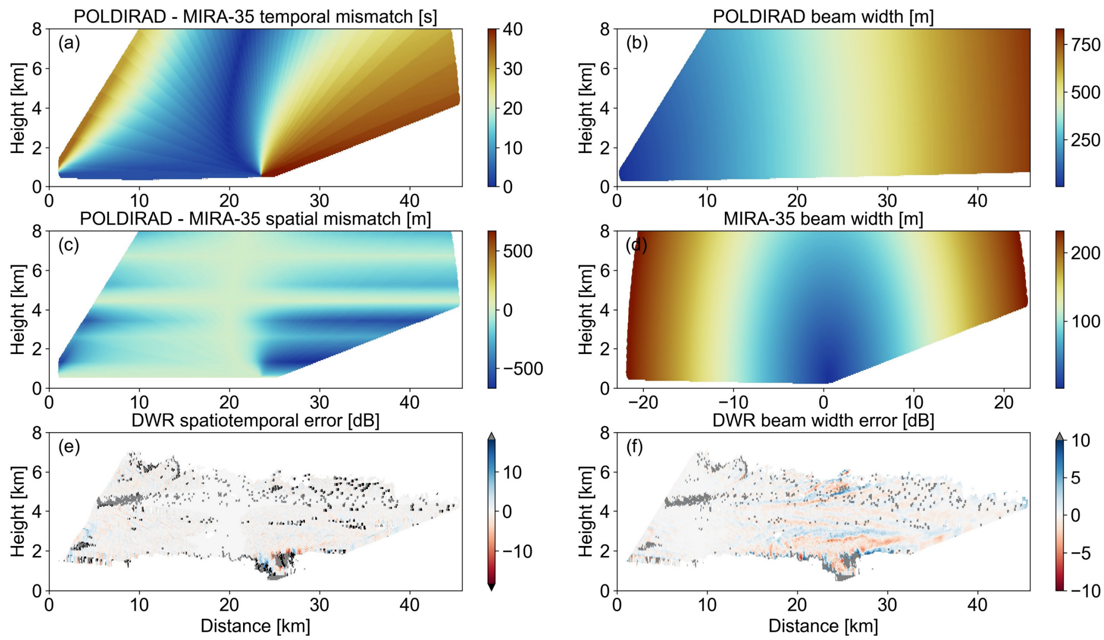

Figure 3.9: DWR error assessment due to temporal mismatch (left panels) and volumetric mismatch (right panels). In (a), (c) and (e) panels, the POLDIRAD and MIRA-35 temporal mismatch, the POLDIRAD and MIRA-35 spatial mismatch and the spatiotemporal error in dB are plotted. In (b) and (d) panels, the POLDIRAD and MIRA-35 beam widths are presented, while in panel (f) the estimated DWR error due to the volumetric mismatch is shown. For this plot the data from 30 January 2019 at 10:08 UTC are used. The ice masked and noise filtered values in (e) and (f) are plotted with grey color. Black color in panel (e) denotes the additional missing values due to the spatial shift of the radar grid. For better visualization purposes the –5 ºC, –15 ºC and –25 ºC temperature levels are not plotted here.

3.1.4 Correcting the radar observations for attenuation effects

Before using the radar observations for the development of the ice retrieval algorithm, they needed to be corrected for beam propagation effects. One major influence was the attenuation by atmospheric gases and by hydrometeors. This was significant especially for the Ka-band radar measurements. Although snow attenuation in C band can be merely neglected especially for low density particles and low snowfall rates (Battan, 1973; Table 6.4), the corrections were done in both radar bands for reliability purposes.

Gaseous attenuation

Both MIRA-35 and POLDIRAD radar reflectivities were corrected for attenuation caused by atmospheric gases. Atmospheric water vapor can cause considerable attenuation of radar signals especially at the higher frequency (35.2 GHz) of the instrumentation. The gaseous attenuation for both radar bands was calculated using formulas proposed by ITU-R P.676-12 model (ITU-R P.676-12, 2019). The corrections were implemented for oxygen and water vapor lines where the attenuation was expected to be significant. The gaseous attenuation formulas used atmospheric pressure, temperature and relative humidity for each RHI, obtained from the Copernicus Climate Change Service (C3S) Climate Data Store (CDS) European Centre for Medium-Range Weather Forecasts (ECMWF) ERA5 reanalysis data (Hersbach et al., 2018).

Figure 3.10 shows specific attenuation lines calculated for temperature 15 °C, pressure 1013 hPa and water vapor 7.5 g m^{-3} for the C and Ka band. In Fig. 3.11 the gaseous attenuation for radar measurements of 30 January 2019 at 10:08 UTC are presented. At Ka band the maximum gaseous attenuation value was calculated at low altitudes, where more water vapor was present, around 1.5 dB (Fig. 3.11a). On the contrary, gaseous attenuation at C band was calculated close to 0 for the same altitudes (Fig. 3.11b).

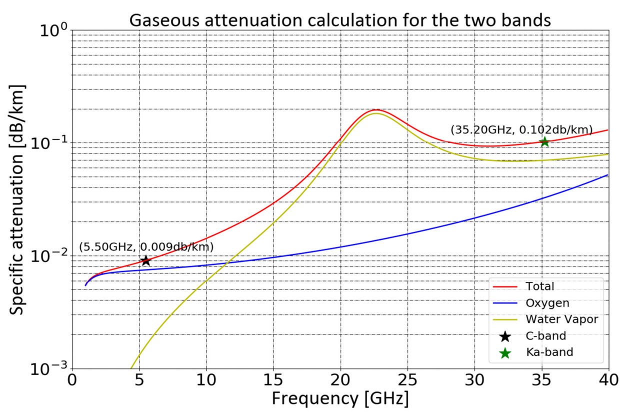

Figure 3.10: Gaseous attenuation calculations using the ITU-R P.676-12 model for temperature 15 °C, pressure 1013 hPa and water vapor 7.5 g m^{-3}.

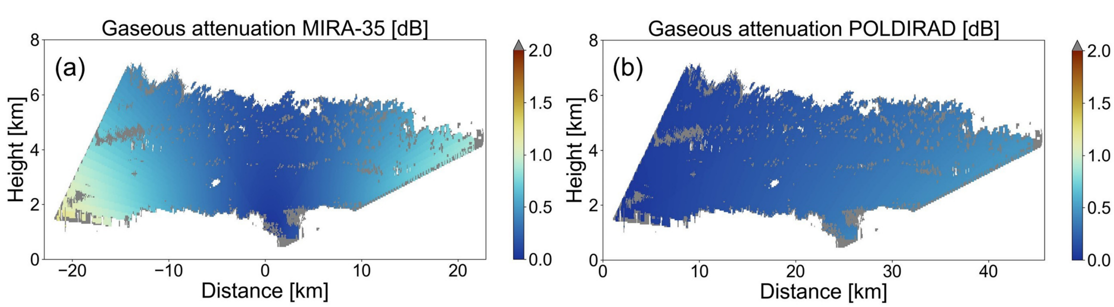

Figure 3.11: Gaseous attenuation estimation for Ka and C band for 30 January 2019 at 10:08 UTC using formulas from ITU-R P.676-12 model (ITU-R P.676-12, 2019). Areas with filtered radar measurements are marked using grey color.

Hydrometeors attenuation

Next to the gaseous attenuation, the hydrometeor attenuation needed to be also considered. For this purpose, an iterative approach using the ice microphysics results was developed. In this way, both radar reflectivities were corrected to mitigate the impact of hydrometeor attenuation on the ice microphysics retrieval. For this approach, the output of the retrieval algorithm was used. A more detailed description of this method will be presented in Sect. 3.3.1 along with the developed ice retrieval scheme.

3.2 Scattering simulations

Single scattering simulations are an indispensable tool to bridge the gap between microphysical properties of hydrometeors and polarimetric radar observations. In the case of ice particles, the calculation of scattering properties can be challenging due to their large complexity, variety in shape, structure, size and density. One of the most sophisticated methods, the Discrete-Dipole Approximation (DDA; Draine and Flatau, 1994), can be used to calculate the scattering properties of realistic ice crystals and aggregates. However, this approximation can be computational demanding. To reduce computation cost and complexity, ice particles are often assumed to be spheres and their scattering properties are calculated using the Mie theory or they are assumed to be spheroids using the T-Matrix method (Waterman, 1965) or the Self-Similar Rayleigh-Gans Approximation (SSRGA; e.g., Hogan and Westbrook, 2014; Hogan et al., 2017; Leinonen et al., 2018a). The calculations when SSRGA is used are known to be affected by the way that ice mass is distributed throughout the volume of the particle. As the goal of this study was to use a simple ice particle model, the T-Matrix method was selected, assuming the ice particles to be *soft spheroids*.

3.2.1 Soft spheroid approximation

In ice particles simulations, it is a common approach that the particles are represented by homogeneous spheroids with density equal or smaller of bulk ice. Due to its simplicity, the limitations of the spheroid approximation have been a heavily researched and debated topic in the last decade. While Tyynelä et al. (2011) showed an underestimation of the backscattering for large snowflakes, Hogan et al. (2012) suggested that horizontally aligned oblate spheroids with a sphericity (S; minor to major axis ratio, also described in Sect. 2.1) of 0.6 can reliably reproduce the scattering properties of realistic ice aggregates which are smaller than the radar wavelength. The same study also concluded that, spheroids are more suitable to represent larger particles (maximum diameter up to 2.5 mm) in simulations, rather than Mie spheres can, as the latter can lead to a strong overestimation of Z_e. Leinonen et al. (2012) on the other hand showed that the spheroidal model cannot always explain the radar measurements as more sophisticated particle models do, e.g., snowflake models. Later on, Hogan and Westbrook (2014) indicated that the soft spheroid approximation underestimates the backscattered signal of large snowflakes (1 cm size) – measured with a 94 GHz radar – up to 40 and 100 times for vertical and horizontal incidence, respectively. In contrast, the simple spheroidal particle model could successfully explain measurements of slant-45° linear depolarization ratio, SLDR, as well as SLDR patterns on the elevation angles (Matrosov, 2015) during the Storm Peak Laboratory

Cloud Property Validation Experiment (StormVEx). In Liao et al. (2016) it was found that randomly oriented oblate ice spheroids could reproduce scattering properties in Ku and Ka band similar to these from scattering databases when ice particles were assumed to have a density of 0.2 g cm^{-3} and a maximum size up to 6 mm. Although Schrom and Kumjian (2018) showed that homogeneous reduced-density ice spheroids or plates cannot generally represent the scattering properties of branched planar crystals, the ellipsoidal and spheroidal model have been used in recent comparison studies to represent ice aggregates as in Jiang et al. (2019). Moreover, the spheroidal model was used to simulate DWR for snow rate estimation studies as in Huang et al. (2019) or to retrieve shape from LDR as in Matrosov (2020). In all these studies, it was recognized that the spheroidal model requires less assumed parameters compared to more complex particle models.

A *soft spheroid* consists of a homogeneous mixture of ice and air and thus, the ice mass is evenly distributed all over the volume of the spheroid. Using the soft spheroid approximation, a decision for the way that the particles would be constructed was needed. In this study, the maximum diameter ($D_{\max}$) and the AR values of the ice spheroids were a-priori chosen and the mass was calculated according to the formula that describes the relation between mass and maximum dimension from the literature (i.e., mass-size relation). With the mass and the dimensions known, the density of the ice spheroid was calculated. In the special case when the density was found to exceed that of solid ice (0.917 g cm^{-3}), the mass of the spheroid was clipped and its density was set equal to 0.917 g cm^{-3}.

Being homogeneous and composed of an ice-air mixture, the soft spheroids were found to have a real component of the refractive index m_{RI} close to 1. Figure 3.12 demonstrates how an ice aggregated particle can be represented using this approach. The soft spheroid model uses the effective medium approximation (EMA; described in Sect. 2.2) to model the refractive index of a composite material as an ice matrix with inclusions of air, which are arranged throughout the ice particle, according to the Maxwell-Garnett mixing formula (Garnett and Larmor, 1904).

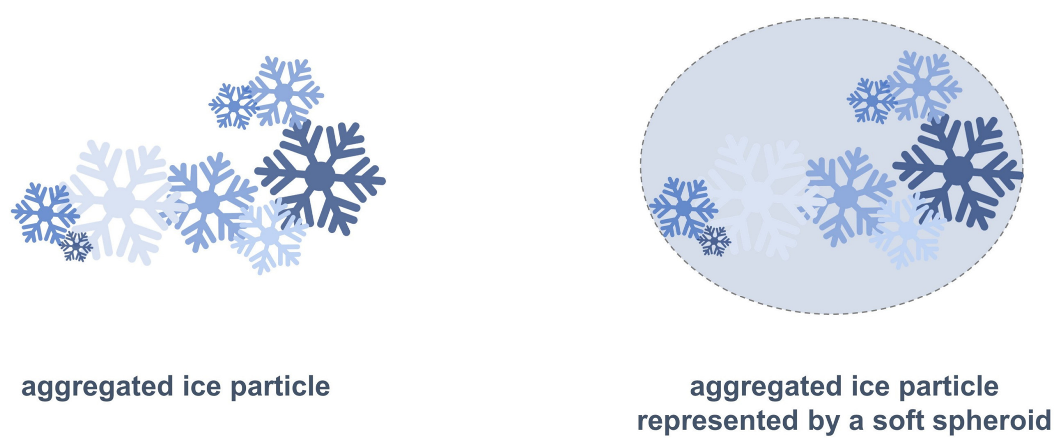

Figure 3.12: Schematic representation of an aggregated ice particle (left) by a soft spheroid (right) with the same mass equally distributed on the whole volume of the spheroid.

The shape of the ice spheroids was defined using the aspect ratio (AR; described in Sect. 2.1) in this study. AR was defined as the ratio of the horizontal to rotational axis of the particle. From the description of the simulated ice spheroids in Fig. 3.13, it is obvious that oblate (shaped like lentil) and prolate particles (shaped like rice) have AR larger and lower than 1.0, respectively, as z axis was selected to be the rotational axis. Using this principle, the representative value of sphericity 0.6 (S; minor to major axis ratio, also described in Sect. 2.1) for oblate ice spheroids from Hogan et al. (2012) was calculated as AR = 1.67 in this study and therefore, this number was used as a reference value for the simulation plots (Fig. 3.14 and 3.16a). In this work, S was used to compare retrieval results for the oblate and prolate assumption. S for oblates and prolates was defined to be smaller than 1, while for spheres was equal to 1. Here, all ice particles were assumed to fall with their maximum diameter aligned to the horizontal plane. Hence, all ice prolates (hereafter referred as horizontally aligned prolates or horizontally aligned prolate ice spheroids) were rotated 90° (mean canting angle) in the yz plane (Fig. 3.13), while ice oblates were not rotated (0° mean canting angle). The canting angle, i.e., angle between the major dimension of the particle and the horizontal plane, of the falling hydrometeors has been the topic of several studies. This value in nature is not so easy to estimate and thus, a standard deviation (e.g., 2°–23° as in Melnikov, 2017) is often additionally used. Here, a fixed standard deviation of 20° was used to describe the tumbling of the maximum dimension of ice spheroids around the selected canting angle. Then, the calculation of the scattering properties was performed using an integration technique for all possible geometries of the particles, ignoring the Euler angles α and β of the scattering orientation.

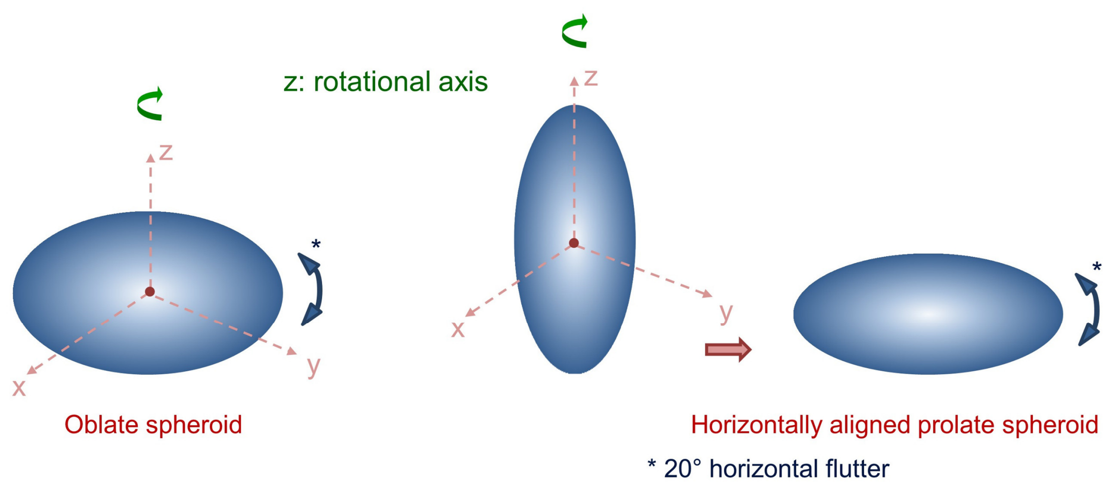

Figure 3.13: Description of simulated oblate, vertically aligned prolate and horizontally aligned (rotated 90° in the yz plane) prolate ice spheroids. Only oblate and horizontally aligned prolate ice spheroids were used in the scattering simulations with a 20° standard deviation out of the horizontal plane.

3.2.2 T-matrix scattering algorithm

The single scattering properties of the ice spheroids were calculated using the T-matrix scattering method as described by e.g., Waterman (1965), Mishchenko and Travis (1994) or Mishchenko et al. (1996). The averaging over particle orientations and the calculation of radar variables for whole size distributions were done using PyTMatrix (Leinonen, 2014). PyTMatrix is a package that can be easily adjusted to the needs of the user via functions and classes regarding the desired preferences for particle shape, size, orientation, particle size distribution and wavelength.

3.2.3 Assumptions for the ice hydrometeors

Combining exponential particle size distribution PSD with the mass-size relation $\mathrm{m}(\mathrm{D}_{\mathrm{max}})$ relationships of BF95 or aggregates (thoroughly described in Sect. 2.1), scattering simulations showed that ice spheroids with $\mathrm{m}(\mathrm{D}_{\mathrm{max}})$ analog to aggregates produced more pronounced polarimetric signatures for larger ice particles due to their higher density and in turn, higher real refractive index. This is illustrated by scattering simulations using both $\mathrm{m}(\mathrm{D}_{\mathrm{max}})$ assumptions which are shown in Fig. 3.14 (BF95 and aggregates line is plotted with black and solid red color, respectively). The simulation calculations were done for horizontally emitted radar beams, for an aspect ratio of 1.67 and an IWC of 0.50 g m^{-3}. Here, larger DWR values are an indication of larger particles, while ZDR values around 0 are an indication of spherical particles. The same figure also shows scattering simulations for ice spheroids with double and half the density of aggregates $\mathrm{m}(\mathrm{D}_{\mathrm{max}})$ (red dashed and dash-dotted line, respectively). This influence of density on retrieval results will be further discussed in a sensitivity study presented in Sect. 4.2.1. In addition, Fig. 3.14 shows DWR-ZDR measurements for low elevation angles (0°–5°) and for all 59 RHI coordinated scans as a blue shaded density histogram. The radar observations were collected during three snowfall events that took place in winter 2019 on 9, 10 and 30 January 2019 over Munich. The dark blue isoline frames the 95$^{\mathrm{th}}$ percentile of the radar observations. In Fig. 3.14, it becomes apparent that the BF95 $\mathrm{m}(\mathrm{D}_{\mathrm{max}})$ relationship assumed for the ice spheroids could not explain the radar observations for large ice hydrometeors as ZDR values drop fast with increasing DWR due to the fast decrease of density with size. Therefore, BF95 was excluded from further analysis at the beginning. However, in the framework of sensitivity analyses that were conducted, retrieval results using BF95 will be presented in Sect. 4.2.1. The mass-size relationship for aggregate ice particles could better explain the density histogram of the DWR-ZDR dataset, especially for particles with DWR > 4 dB.

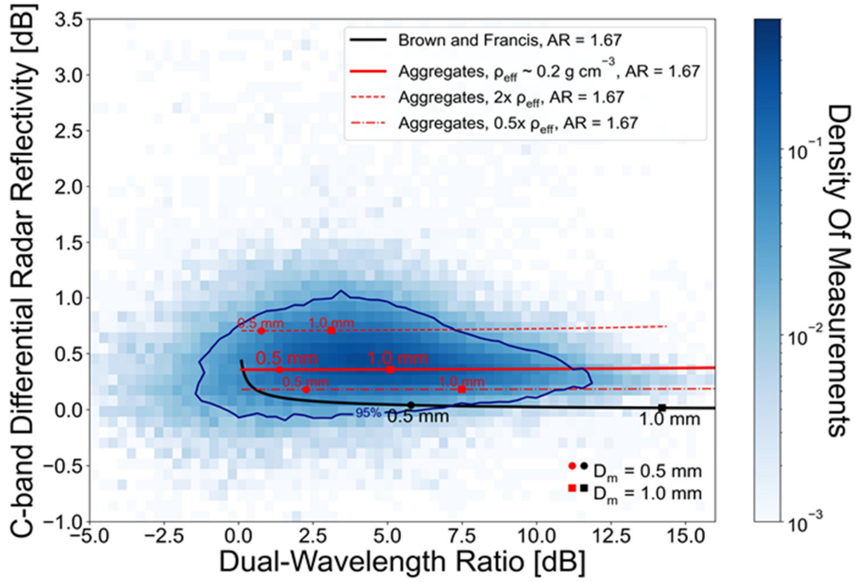

Figure 3.14: Radar observations between 0°–5° elevation angles and scattering simulations for ice spheroids with $m(D_{max})$ corresponding to aggregates (red) and BF95 (black) for AR = 1.67, IWC = 0.50 g m^{-3} and both radar beams simulated to be emitted horizontally. With scatters, the D_m = 0.5 mm and D_m = 1.0 mm are denoted. The 95^{th} percentile of the 2D density histogram is drawn with a dark blue isoline. With red dashed and dash-dotted lines simulations for ice spheroids with double and half the density of aggregates are plotted.

3.2.4 Look-up tables

Using ice spheroids that follow the $\mathrm{m(D_{max})}$ of aggregates, look-up tables (LUTs), for different values of median mass diameter D_{m}, AR, IWC and geometries (Fig. 3.15) covering the radar elevation angles (presented in Fig. 3.2) were created. D_{m} of the PSD was varied between 0.1–3.02 mm in a logarithmic grid of 150 points. For all calculations, a minimum, $D_{\mathrm{min\_PSD}}$, and a maximum, $D_{\mathrm{max\_PSD}}$, diameter of 2×10^{-2} mm and 20 mm were used as integration boundaries in the PSD of the ice particles, as this study investigated ice particles detected only into clouds and above ML. A minimum sensitivity limit of DWR = 0.1 dB was used in the simulations leading to different minimum retrievable D_{m} according to the $\mathrm{m(D_{max})}$ and the AR used, but also the radar viewing geometry (more details about this topic can be found in Appendix A). IWC was varied between 0.00001−1 g m^{-3} in a logarithmic grid of 101 points. Scattering properties for spheroid oblate and horizontally aligned prolate ice particles, with a horizontal flutter of 20° out of the horizontal plane, were calculated and saved in separated LUTs with the aspect ratio ranging between 0.125−1.0 (values: 0.125, 0.16, 0.21, 0.27, 0.35, 0.45, 0.6, 0.8, 1.0) for the horizontally aligned prolates and the inverted values for the oblate particles.

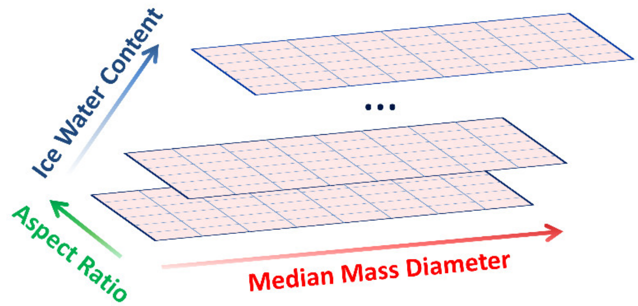

Figure 3.15: Schematic 3D representation of the look-up tables.

3.3 Ice microphysics retrieval

To better explain the way that the ice microphysics retrieval was developed, two examples of the scattering simulations are presented in Fig. 3.16. For the creation of both panels the simulated radar beams were assumed to be transmitted horizontally towards each other (horizontal-horizontal geometry). For Fig. 3.16a the AR was chosen 1.67. Radar reflectivity Z_e at C band as well as DWR were calculated for different D_m values and different values of IWC of the PSD. Larger values of radar reflectivity Z_e at C band are observed for larger values of D_m and larger IWC. Furthermore, as D_m increases, DWR increases as well, indicating the sensitivity of DWR to the particle size. An important remark is that for constant D_m, DWR remains invariant to varied IWC. For Fig. 3.16b IWC was chosen to be 0.50 g m^{-3}. Howvere, ZDR values are found to be invariant for all simulated values of IWC when AR, D_m and width parameter μ of PSD as well as the $m(D_{max})$ remained the same. In the same figure, it is also obvious that simulation lines for oblates or horizontally aligned prolates are not distinct in the ZDR-DWR space. For this reason, there was the need to assume either oblates or prolate ice spheroids that are horizontally oriented in the retrieval. All the aforementioned principles were then used to implement a method for retrieving ice microphysics information from radar measurements.

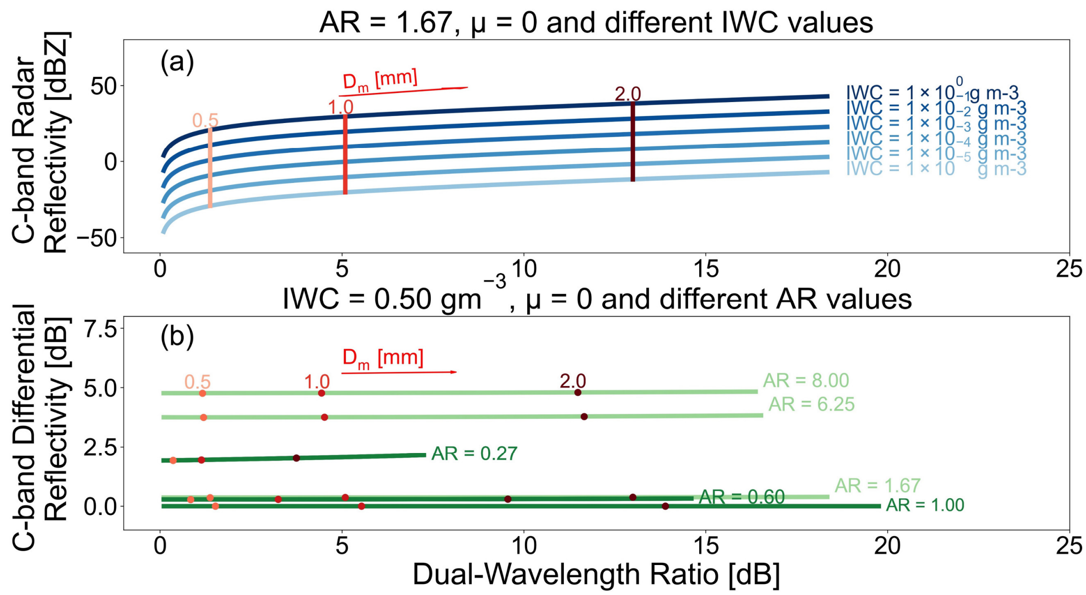

Figure 3.16: Scattering simulations for (a) radar reflectivity and (b) differential radar reflectivity vs. dual-wavelength ratio for horizontally aligned spheroid ice particles, horizontal-horizontal geometry, width parameter $\mu = 0$ and m(D_{max}) of aggregates. For the upper panel the AR was chosen 1.67, while for the bottom panel the IWC was chosen 0.50 g m^{-3}. The light green and the dark green color lines denote simulations for oblates and horizontally aligned prolates, respectively.

For the development of the ice retrieval scheme, radar measurements of Z_e, ZDR and DWR were compared with the PyTMatrix scattering simulations described in Sect. 3.2. The retrieved parameters were IWC in g m^{-3}, D_m of the PSD in mm, and AR of the measured hydrometeors. Considering their different ranges, normalized differences between simulated and measured values of DWR as well as Z_e and ZDR at C band were calculated. By minimizing these differences, the best-fitting microphysical parameters were found. The microphysics retrieval was implemented in two steps using the minimization of the two following cost functions J_1 and J_2:

$$\begin{aligned} &\min J_1(D_m, \mathrm{AR}) = \mathrm{norm}\big(\Delta\mathrm{ZDR}(D_m, \mathrm{AR})\big) + \mathrm{norm}\big(\Delta\mathrm{DWR}(D_m, \mathrm{AR})\big) \\ &\min J_2(\mathrm{IWC}) = \mathrm{norm}\left(\Delta \mathrm{Z}_{e_C}(\mathrm{IWC})\right) \end{aligned} \tag{3.1}$$

where with Δ the difference between simulated and measured parameter is denoted. Both ZDR and DWR were invariant to IWC when same values of D_m and AR were used. Therefore, D_m and AR were found in the first step, whilst the IWC was constrained in the second step. While the DWR contributes to the retrieval of D_m, the ZDR measurement merely narrows down the solution of aspect ratio of the ice particles. As Z_e at C band is less affected by attenuation compared to Ka band, it was better suited to estimate the IWC.

3.3.1 Using the ice retrieval to estimate hydrometeors attenuation

After the retrieval of size D_{m} and shape AR in the first step, the algorithm continued with these values with the retrieval of IWC in the second step by minimizing the cost function J_2 in the LUT. Completing these two steps, the microphysics retrieval retrieved not only preliminary D_{m}, AR and IWC but also the specific attenuation A at both radar bands which was then used for the total attenuation estimation. As the ice retrieval produced results using radar measurements interpolated onto a cartesian grid, the retrieved A at C and Ka band needed to be converted from cartesian to the original polar coordinates for the calculation of the total attenuation for each radar band. After A, in polar coordinates, was integrated along the radar beams, the total attenuation for each radar dataset was calculated and converted back from polar to cartesian coordinates. Then, it was used to correct Z_e for both radars. In the next step, the final microphysical parameters such as AR, IWC and D_{m} were retrieved using the corrected Z_e from both bands as well as ZDR from POLDIRAD. Figure 3.17 shows the process of attenuation correction and retrieval in more detail. An output example of the ice microphysics retrieval scheme for the already introduced case study from 30 January 2019 at 10:08 UTC can be found in Sect. 4.1. The total attenuation for this case study is presented in Appendix B of the present doctoral thesis.

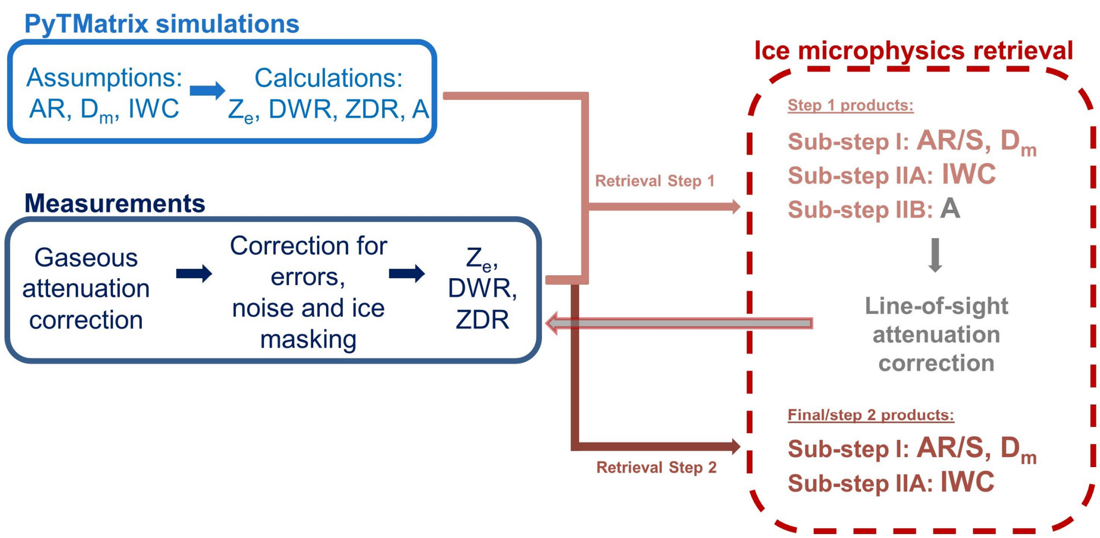

Figure 3.17: Ice microphysics retrieval flowchart. The dark blue color refers to radar observations. The light blue color is used for scattering simulations and the red dotted rounded rectangle gives information about the ice microphysics retrieval scheme. With gray color the total attenuation correction method is described.

Chapter 4

4 Results

This section contains work, which has already been published by Tetoni et al. (2022) in Atmospheric Measurement Techniques (AMT), entitled *"Retrievals of ice microphysical properties using dual-wavelength polarimetric radar observations during stratiform precipitation events"*.

Comparing a novel combination of radar measurements to scattering simulations for ice spheroids, a retrieval algorithm which provides microphysical information, i.e., IWC, AR and D_{m}, about the ice hydrometeors was developed. As of radar observations, radar reflectivity Z_e, differential radar reflectivity ZDR and dual-wavelength ratio DWR were used with sensitivity to ice hydrometeors mass, shape and size. While the retrieval algorithm is extensively described in Sect. 3.3, in this chapter the retrieval results for selected case studies will be presented. To demonstrate the followed approach, the already presented case study from Fig. 3.3 was also used in the ice retrieval making assumptions for the ice particles. Using the ice microphysics retrieval, results for mass, shape and size of ice hydrometeors will be shown. Investigating radar measurements from 59 RHI scans in total, by retrieving microphysical properties for the detected ice particles during three snowfall events, a statistical analysis, using oblate or prolate spheroid assumption in the scattering calculations, was conducted and will be presented in Sect. 4.1.2. In the last section of this chapter, sensitivity studies, on how the retrieval results can change when different assumptions for the ice spheroids are used, will be shown, exploiting a more homogeneous snowfall case study with a similar stratified radar reflectivity field; low Z_e at cloud top and higher Z_e values towards the melting layer.

4.1 Retrieval results for a selected case study

Here, the already shown atmospheric scene from 30 January 2019 at 10:08 UTC (Fig. 3.3, Sect. 3.1.1) is used to demonstrate the output of the ice microphysics retrieval. For all the presented results, it was anticipated that the ice hydrometeors can be represented by ice spheroids that follow the aggregates mass-size relation and an exponential PSD. The microphysical properties of the detected hydrometeors are shown in Fig. 4.1 (assuming oblate ice spheroids) and Fig. 4.2 (assuming horizontally aligned prolate ice spheroids). In Fig. 4.1a and 4.2a, the retrieved AR is presented. Both plots suggest that in the cross-section of the cloud between the two radars and especially, in the area which is below 3 km height at a distance 0–12 km away from POLDIRAD, more spherical ice hydrometeors were present. Further away at a distance 12–20 km from POLDIRAD, more aspherical particles with AR around 4.0 and AR around 0.5, for oblates and horizontally aligned prolates respectively, were found. The same result is also supported from S plots in Fig. 4.1c and 4.2c where $S > 0.6$ for the spherical particles between 0–12 km distance and $S < 0.6$ for the aspherical particles between 12–20 km distance. The retrieved AR and S could explain well the ZDR measurements from Fig. 3.3d where more spherical particles had ZDR < 0.5 dB, while aspherical particles have ZDR > 0.5 dB. In Table 4.1, the Root Mean Square Error (RMSE) over all points of the cloud cross-section describes the difference between the fitted and measured ZDR for the whole scene. Overall, the ZDR measurements could be replicated better with the retrieval results using oblate ice spheroids with RMSE = 0.19 dB (against RMSE = 0.25 dB when horizontally aligned prolate ice spheroids were used). The retrieved D_m increasing towards the ground (for the range between 20–30 km away from POLDIRAD) is an indication that large ice particles were present below 3 km height compared to smaller particles that were dominant at higher altitudes. This is shown in both results for oblates and horizontally aligned prolates (Fig. 4.1b and 4.2b). Comparing this plot with the DWR measurements from Fig. 3.3b, it is clear that the retrieved D_m could reasonably explain DWR. The correlation between measured and simulated DWR was found again to be better when oblate ice spheroids were used. In particular, the RMSE for the fitted-simulated and measured DWR was 0.50 dB when ice oblates were used in the simulations, while RMSE = 0.61 dB when the ice particles were assumed horizontally aligned prolates. Although DWR and ZDR measurements were combined for the shape and size retrieval (minimization of J_1 in Eq. 3.1), the spatial patterns agreement between DWR-D_m and ZDR-AR/S plots indicated the strong correlation of DWR and ZDR with size and shape, respectively. Figure 4.1d and 4.2d show the results of the retrieved IWC for oblates and horizontally aligned prolate ice spheroids described by the $\mathrm{m(D_{max})}$ of aggregates and the exponential PSD. Areas with positive POLDIRAD Z_e values in Fig. 3.3c corresponded to IWC values higher than 1×10^{-3} g m^{-3}. Hence, the sensitivity of Z_e to mass of the ice particles was indicated for both spheroid assumptions (oblates and horizontally aligned prolates). Nevertheless, the Z_e RMSE for horizontally aligned prolate ice particles was 0.36 dB, whilst the RMSE was found 0.20 dB when ice oblates were used. All in all, the lowest RMSE for all radar variables were found when oblate ice spheroids were assumed (all RMSE are summarized in Table 4.1).

Using the retrieved specific attenuation A from the step 1 of the retrieval scheme (shown in Fig. 3.17), the hydrometeors attenuation for the selected case study was estimated. A was integrated along the radar beams and then, the total attenuation for each radar dataset was calculated. The steps for this estimation are described in detail in Sect. 3.3.1, while the attenuation results for both radars and oblate or horizontally aligned prolate assumption can be found in the Appendix B.

Table 4.1: RMSE values between simulated and observed ZDR, DWR, Z_e values for the whole radar cross-section after running the retrieval for 30 January 2019 at 10:08 UTC using oblate and horizontally aligned prolate ice spheroids and assuming their $\mathrm{m(D_{max})}$ to be the aggregates from Yang et al. (2000).

Oblate/prolate assumption	Parameter	RMSE
Oblates	DWR	0.50 dB
	ZDR	0.19 dB
	Z_e	0.20 dB
Horizontally aligned prolates	DWR	0.61 dB
	ZDR	0.25 dB
	Z_e	0.36 dB

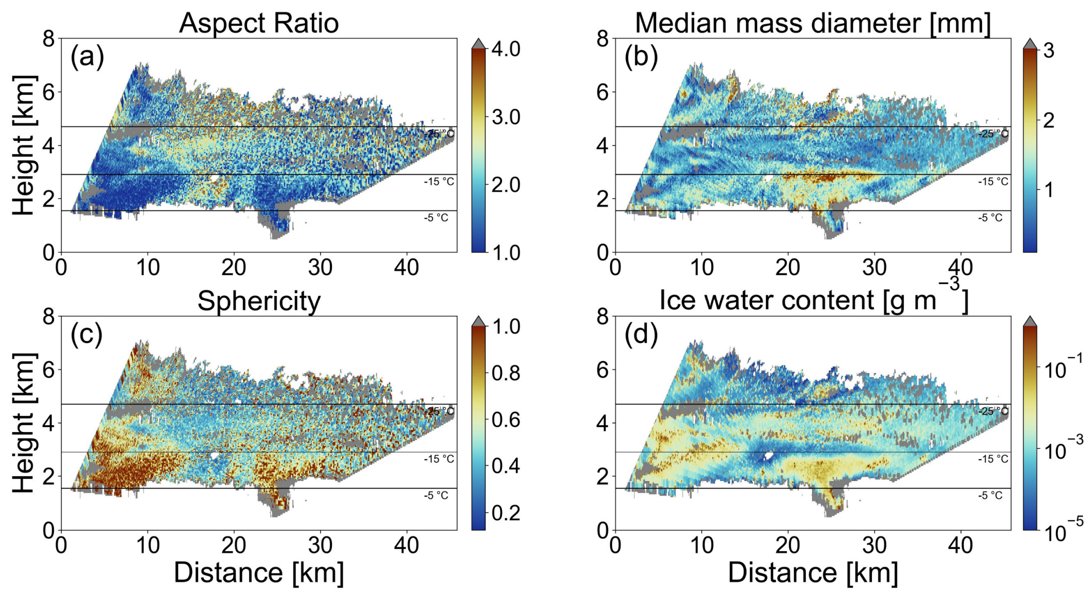

Figure 4.1: Retrieved (a) AR, (b) D_m, (c) S and (d) IWC for 30 January 2019 at 10:08 UTC with ice spheroids assumed to be oblates, following an exponential PSD and their m(D_{max}) corresponding to aggregates from Yang et al. (2000). The –5 ºC, –15 ºC and –25 ºC temperature levels are plotted with black solid lines (source: Deutscher Wetterdienst, data provided by University of Wyoming; http://weather.uwyo.edu/upperair/sounding.html, last access: 08 April 2022). Areas with filtered radar measurements are marked using grey color.

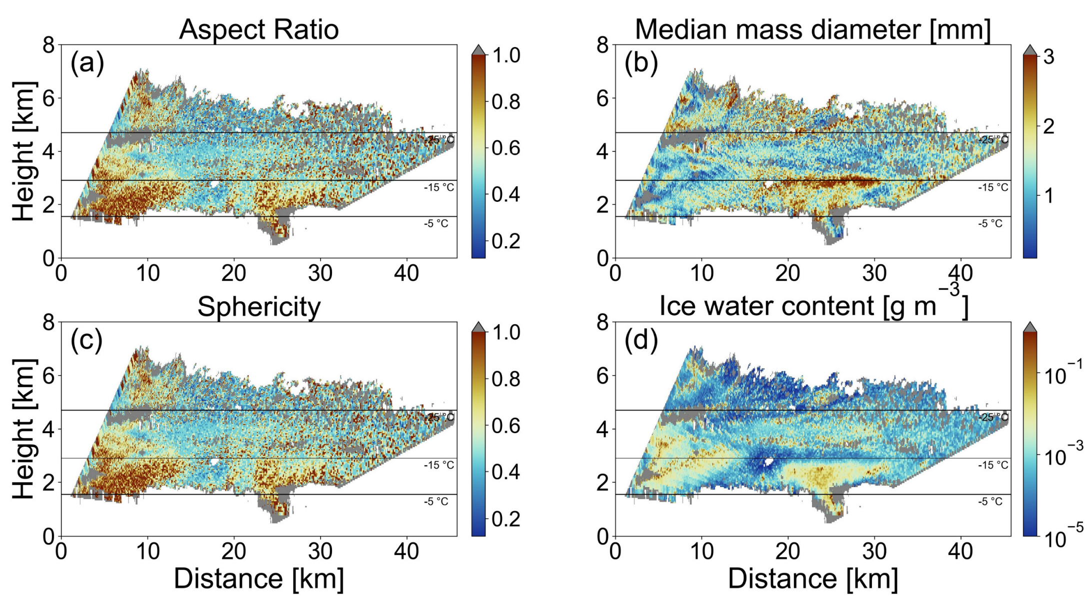

Figure 4.2: Retrieved (a) AR, (b) D_m, (c) S and (d) IWC for 30 January 2019 at 10:08 UTC with ice spheroids assumed to be horizontally aligned prolates, following an exponential PSD and their m(D_{max}) corresponding to aggregates from Yang et al. (2000). The –5 ºC, –15 ºC and –25 ºC temperature levels are plotted with black solid lines (source: Deutscher Wetterdienst, data provided by University of Wyoming; http://weather.uwyo.edu/upperair/sounding.html, last access: 08 April 2022). Areas with filtered radar measurements are marked using grey color.

4.1.1 Retrieved parameters error assessment

Figure 4.3 shows averaged profiles of D_m and IWC for the whole cloud cross-section measured on 30 January 2019 at 10:08 UTC when different error sources and oblate or prolate assumption were considered. In Fig. 4.3a and 4.3b, the averaged D_m and IWC profile for oblate ice spheroids, as they were calculated from Fig. 4.1b and 4.1d with only accounting for ice masked and noise-filtered measurements, are plotted in dark red and dark blue, respectively. In the same panels, the averaged D_m and IWC profiles are plotted with different red and blue shades for different combinations of calibration errors for POLDIRAD (±0.5 dBZ) and MIRA-35 (±1.0 dBZ). Figure 4.3a indicates that, e.g., the lowest values of D_m were retrieved when the calibration for POLDIRAD and MIRA-35 would be dZ_{e_C} = –0.5 dBZ and $dZ_{e_{Ka}}$ = +1.0 dBZ respectively, resulting in a DWR bias of –1.5 dB. Due to the smaller D_m retrieval, the retrieved IWC profile in Fig. 4.3b was the largest in this case. In the lower panels of the same figure, the same profiles of D_m (Fig. 4.3c) and IWC (Fig. 4.3d) are plotted again, this time including the additional errors caused by the spatiotemporal and beam width mismatch discussed in Sec. 3.1.3. While the beam width mismatch could locally lead to the most significant deviations (shown in Fig. 3.9), the calibration uncertainty (red and blue shades) in the worst cases (for dZ_{e_C} = –0.5 dBZ, $dZ_{e_{Ka}}$ = +1.0 dBZ vs. dZ_{e_C} = +0.5 dBZ, $dZ_{e_{Ka}}$ = –1.0 dBZ) could lead to the largest bias throughout the profile. With increasing microphysical heterogeneity within a cloud, the DWR error due to the volumetric mismatch between the instruments would increase. Here, criteria would need to be defined where the estimated DWR errors could indicate a non-applicability of the multi-wavelength technique. The selection of such criteria, however, would require an in-depth sensitivity study using model clouds and in situ data which was beyond the scope of the present study. This error estimation therefore, only served as an indication in which areas the retrieval results should be taken with caution. The lower panels of Fig. 4.3 also show the averaged D_m and IWC profile (dashed lines) as they were calculated from Fig. 4.2b and 4.2d when horizontally aligned prolate ice spheroids were assumed. Between the two assumptions the horizontally aligned prolates yielded a larger D_m profile (+0.31 mm) on average, while oblate ice spheroids yielded a slightly larger IWC profile (+0.002 g m^{-3}). With the influence of the calibration uncertainty on the retrieved D_m and IWC profile with ±0.41 mm and ±0.02 g m^{-3}, respectively, the oblate or prolate assumption was found to be of equal significance for the retrieval of D_m, while it was less important than the calibration uncertainty for the retrieval of IWC.

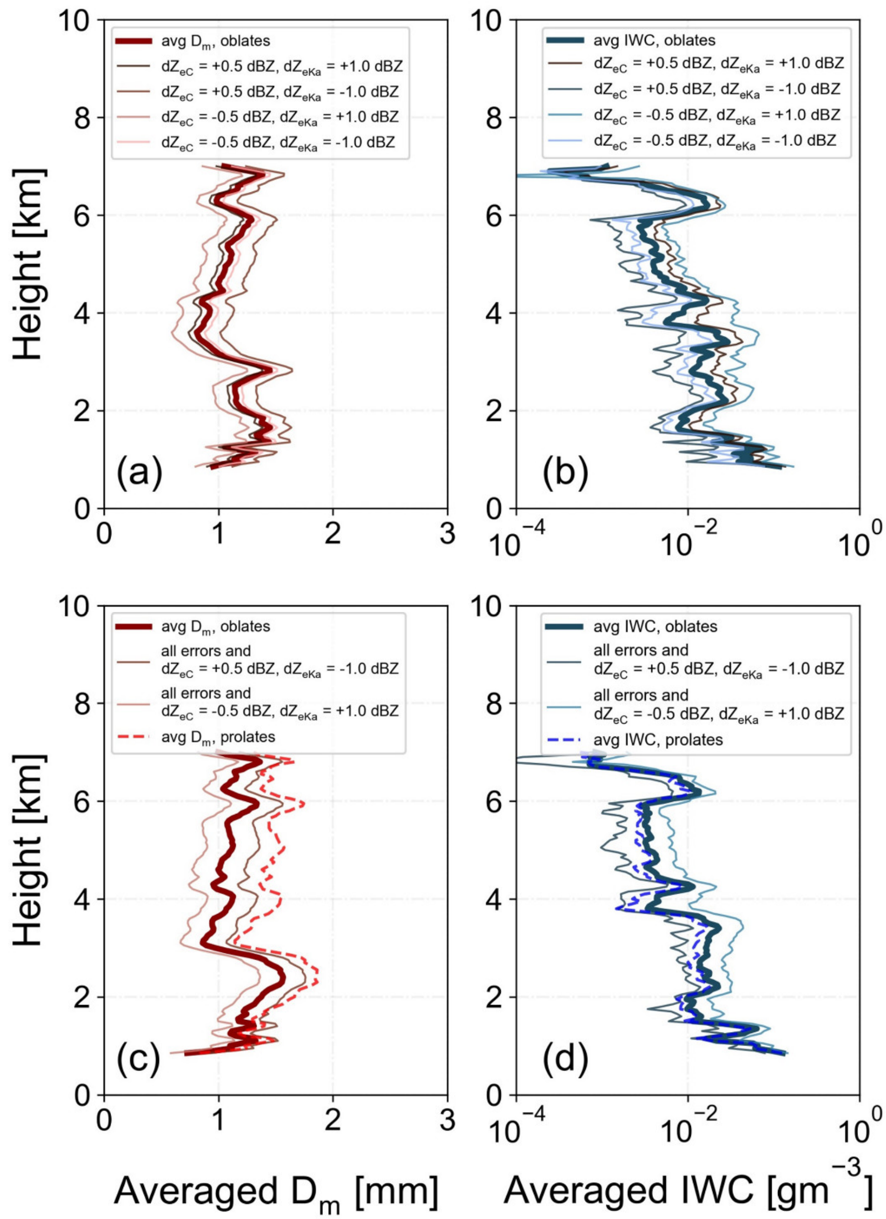

Figure 4.3: Averaged profiles of the retrieved (a) D_m and (b) IWC as derived from Fig. 4.1b and 4.1d for oblate ice spheroids, with (thinner lines) and without (thicker line) considering the calibration error for both radars. (c, d) Same as upper panels but now the beam width error, the spatiotemporal error as well as dDWR = +1.5 dB or dDWR = –1.5 dB is considered. With dashed lines the retrieved D_m and IWC as derived from Fig. 4.2b and 4.2d for the prolate assumption is plotted. All panels refer to the case study from 30 January 2019 at 10:08 UTC as well as to aggregate mass-size relationship and exponential particle size distribution.

4.1.2 Statistical analysis of the retrieved results

After investigating 59 pairs of RHI scans from three different snow events (9 January 2019 between 11:18−15:08 UTC, 10 January 2019 between 09:08−17:08 UTC and 30 January 2019 between 10:08−12:38 UTC), stacked histograms with respect to temperature were created for a deeper insight of the retrieval. Particularly, all RHI measurements from these days were compared to scattering simulations in LUTs for oblate and horizontally aligned prolate ice particles.

Statistical results of the retrieved S, D_m as well as IWC for ice spheroids with $\mathrm{m(D_{max})}$ corresponding to this of aggregates and exponential PSD assumption are presented in Fig. 4.4 (results for the retrieved parameters assuming oblate ice spheroids) and Fig. 4.5 (results for horizontally aligned prolate ice spheroids). At first glance, the majority of ice hydrometeors were found to be neither very spherical nor very elongated (green color panel plots, in Fig. 4.4 and 4.5). When oblate ice spheroids were used in the scattering simulations, the greater part of retrieved S values was found to range from 0.3 to 0.6. With the assumption that ice hydrometeors can be represented by horizontally aligned prolate ice spheroids, the distribution was narrower with the majority of the detected particles to have S values ranging between 0.4−0.6. From the D_m retrieval (red color panel plots, in Fig. 4.4 and 4.5) the results for oblates showed a narrower distribution shifted towards smaller median mass diameters, while for horizontally aligned prolates the retrieved values were more broadly distributed towards larger values of D_m (median value of both distributions can be found in Table 4.2). The histograms for the retrieved IWC (blue color plot panels, in Fig. 4.4 and 4.5) are plotted using logarithmic x axis for visualization purposes. The statistical results showed that the greater part of the detected ice hydrometeors was found to have IWC values 3×10^{-4}–3×10^{-1} g m^{-3} (−3.5 to −0.5 in the logarithmic axis) when oblate ice spheroids were assumed. For horizontally aligned prolate ice particles, most of the detected ice hydrometeors were found to have IWC values between 1×10^{-4}–1×10^{-1} g m^{-3} (−4 to −1 in the logarithmic axis). The spikes in both D_m and IWC histograms were merely caused from the strong discrepancies between simulated and measured radar variables during the minimization of J_1 and J_2 in Eq. (3.1), i.e., negative measured values of DWR, while the minimum value 0.1 dB was used in the simulations (described in Appendix A). The different color shades in all panel plots denote the different temperature groups in which the detected hydrometeors were separated.

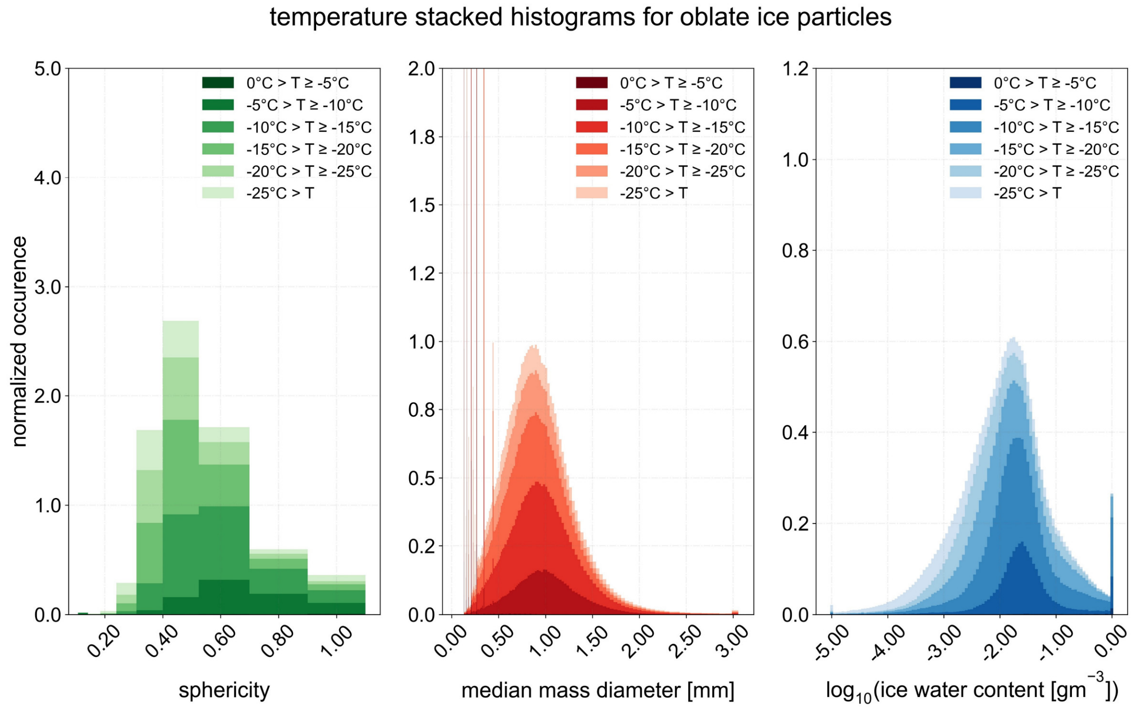

Figure 4.4: Temperature stacked histograms for all RHI scans on 9, 10 and 30 January 2019 for oblate ice particles using the retrieval output for ice spheroids $m(D_{max})$ to be the aggregates from Yang et al. (2000).

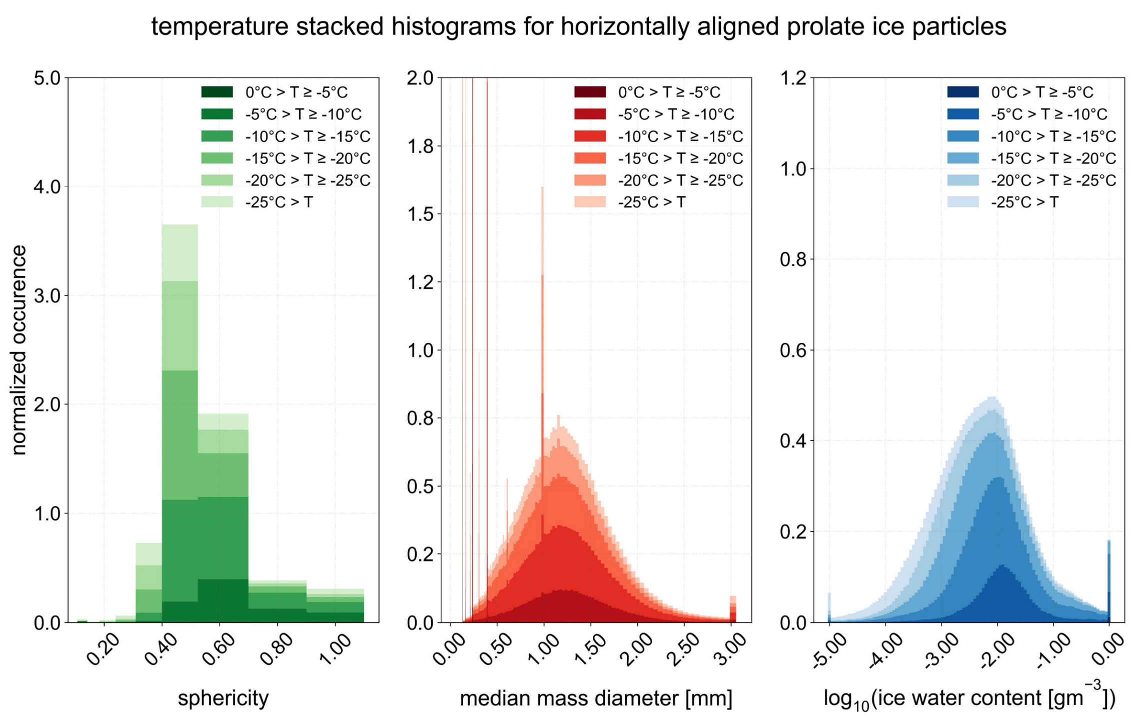

Figure 4.5: Temperature stacked histograms for all RHI scans on 9, 10 and 30 January 2019 for horizontally aligned prolate ice particles using the retrieval output for ice spheroids $m(D_{max})$ to be the aggregates from Yang et al. (2000).

For better interpretation of the ice retrieval results during the three snow events, the calculation of some descriptive statistics is presented in Table 4.2, always under the assumption that the detected ice hydrometeors can be represented by ice spheroids whose $\mathrm{m(D_{max})}$ corresponds to that of aggregates and they follow a PSD with $\mu = 0$ (exponential). The median of the retrieved properties for the observed particles distributions was calculated. Anticipating that the detected ice particles can be represented by oblate spheroids, the median retrieved S was found 0.45, the median retrieved $D_\mathrm{m} = 0.80$ mm and the median retrieved IWC = 13×10^{-3} g m^{-3}. On the contrary, when the observed hydrometeors were assumed to be horizontally aligned prolate spheroids, the median retrieved sphericity, the median retrieved median mass diameter and the median retrieved ice water content, were found $S = 0.45$, $D_\mathrm{m} = 1.08$ mm and IWC = 5×10^{-3} g m^{-3}, respectively. Although the two median S are the same, there are differences in the median D_m and IWC between oblates and horizontally aligned prolates. For the latter, the median D_m was calculated larger and the IWC was calculated lower than the respective values for oblate ice spheroids. Therefore, the oblate or prolate assumption seemed to affect the retrieved microphysical properties of the ice particles (this will be also shown in Sect. 4.2.4)., pointing out the necessity for individual sensitivity studies on each of the assumptions made for the ice particles. In Table 4.2 the 10$^{\mathrm{th}}$ and 90$^{\mathrm{th}}$ percentile of the detected ice hydrometeors retrieved parameters can be also found.

Table 4.2: Statistical description of the retrieved parameters for oblate and horizontally aligned prolate ice spheroids that follow mass-size relation of aggregates from Yang et al. (2000) for all RHI scans on 9, 10 and 30 January 2019.

Oblate/prolate assumption	**Statistical description**	**Sphericity**	**Median mass diameter [mm]**	**Ice water content [g m^{-3}]**
Oblates	Median	0.45	0.80	13×10^{-3}
	10$^{\mathrm{th}}$ percentile	0.35	0.27	11×10^{-4}
	90$^{\mathrm{th}}$ percentile	0.80	1.36	11×10^{-2}
Horizontally aligned prolates	Median	0.45	1.08	5×10^{-3}
	10$^{\mathrm{th}}$ percentile	0.45	0.40	4×10^{-4}
	90$^{\mathrm{th}}$ percentile	0.80	1.82	6×10^{-2}

4.2 Sensitivity studies

Presented results using oblate or horizontally aligned prolate ice spheroids show that this assumption can lead to different retrieved ice microphysical properties. Seeking to better understand whether the assumptions used for the development of the ice microphysics retrieval are the most representative for the measurement dataset and how the results of the retrieval can differ depending on these assumptions made for the ice spheroids, several sensitivity studies were conducted. Therefore, different mass-size relations and hypotheses in particle size distribution, shape or horizontal flutter of ice particles were tested. Since the RMSE for oblates were found to be smaller than these of the horizontally aligned prolates in Sect. 4.1, oblate ice spheroids were merely used in the following sensitivity studies.

4.2.1 Mass-size relation

A significant assumption that had to be made about the simulated ice spheroids was about their mass. In the framework of the sensitivity studies on this assumption, the mass, shape and size of the detected hydrometeors was retrieved using aggregates and BF95 as well as modified and combined versions of the aforementioned $\mathrm{m(D_{max})}$ for the ice spheroids.

Brown and Francis $\mathbf{m(D_{max})}$

The ice retrieval results for 30 January 2019 at 10:08 UTC using LUTs for oblate ice spheroids, an exponential PSD and BF95 mass-size relation are presented in Fig. 4.6 along with the residual values of ZDR, DWR and Z_e, expressed using RMSE values in Table 4.3. The RMSE for ZDR and Z_e were quite low and generally in the same order of magnitude like the RMSE using $\mathrm{m(D_{max})}$ of aggregates for both oblate and prolate assumption (Table 4.1). However, for the BF95 $\mathrm{m(D_{max})}$ and the exponential PSD assumption, the retrieved AR and S (Fig. 4.6a and 4.6c) could not really explain ZDR measurements from Fig. 3.3d. The AR was retrieved quite large, suggesting e.g., plates, for the greater part of the cloud cross-section when the BF95 $\mathrm{m(D_{max})}$ was used. The RMSE for DWR with 2.27 dB was found to be quite high, suggesting that the retrieved D_m (Fig. 4.6b) could not replicate the DWR measurements (Fig. 3.3b). On the other hand, the retrieved IWC (Fig. 4.6d) showed a good agreement to the radar measurements as it could explain POLDIRAD Z_e shown in Fig. 3.3c. The retrieved values using the BF95 were found to be larger than the IWC values retrieved using the $\mathrm{m(D_{max})}$ of aggregates for both oblate and prolate assumption. Overall, the plots of retrieved parameters as well as the RMSE for ZDR, DWR and Z_e indicated that the output of the ice retrieval using an exponential PSD, the $\mathrm{m(D_{max})}$ of aggregates and LUTs for oblate ice spheroids (Fig. 4.1 and Table 4.1) was found to better explain the radar observations compared to the results assuming the BF95 mass-size relation. Figure 4.7 shows the residuals between the simulated and measured DWR for the aggregates (Fig. 4.7a) and the BF95 (Fig. 4.7b) $\mathrm{m(D_{max})}$. For ice spheroids that follow the $\mathrm{m(D_{max})}$ of aggregates, the residuals were distributed around 0 suggesting that this mass-size relation could better explain the radar measurements in this case. In contrast, the measured DWR appeared to be higher than the simulated one for BF95 for quite large part of the cloud cross-section (reddish areas).

Modified aggregates $\mathbf{m(D_{max})}$

To further investigate the significance of the $\mathrm{m(D_{max})}$ relation for the retrieval results, a small sensitivity study was conducted using the aggregates assumption from Yang et al. (2000) which suggests an almost constant effective density, ρ_eff, (approximately ρ_eff = 0.2 g cm^{-3}) of ice particles with increasing size (Fig. 2.2). Using this value as a reference, LUTs for oblate ice particles were created, 1) with twice and 2) with half the density of the aggregates mass-size relation (simulations shown in Fig. 3.14 with red dashed and dash-dotted lines), always with the assumption that the oblate ice spheroids followed an exponential PSD. Retrieval results for ice oblates with half, equal and twice the density of aggregates, are shown in (a)-(c), (d)-(f) and (g)-(i) panels of Fig. 4.8, respectively. Corresponding RMSE values for Z_e are given in Table 4.3. Focusing on the IWC retrieval, lower IWC values (with a RMSE = 0.28 dB for Z_e) were obtained for ice particles with twice the density of aggregates than the IWC values retrieved in Fig. 4.1d or 4.8f. Analogously, larger IWC (with a RMSE = 0.23 dB for Z_e) were retrieved for ice particles with half the density of aggregates. In Table 4.3 the residual values expressed as RMSE for DWR and ZDR can also be found. When the ice spheroids were denser with doubled the aggregates ρ_{eff}, the DWR RMSE was 0.50 dB, while the DWR RMSE was 0.54 dB for the less dense ice spheroids. The RMSE for ZDR were found to be similar with 0.21 dB and 0.20 dB when ice spheroids with twice and half the density of aggregates, respectively, were assumed. However, the denser ice spheroids assumption (doubled effective density of aggregates mass-size relation) suggested the presence of more spherical particles compared to more aspherical particles when less dense ice spheroids (halved effective density of aggregates) were assumed.

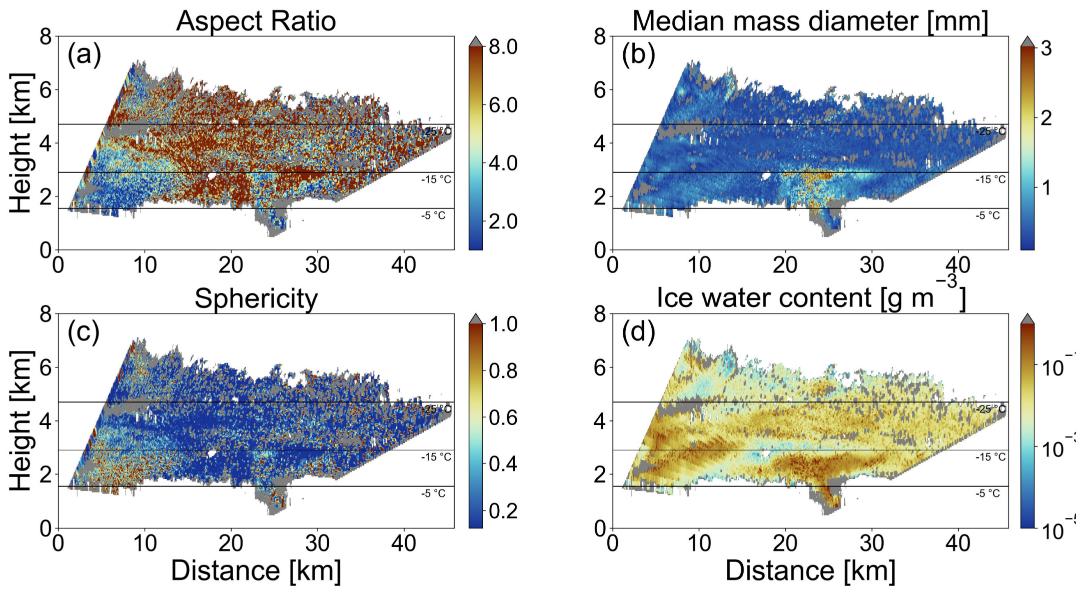

Figure 4.6: Retrieved (a) AR, (b) D_m, (c) S and (d) IWC for oblate ice particles for 30 January 2019 at 10:08 UTC using BF95 m(D_{max}) and an exponential PSD. The –5 ºC, –15 ºC and –25 ºC temperature levels are plotted with black solid lines (source: Deutscher Wetterdienst, data provided by University of Wyoming; http://weather.uwyo.edu/upperair/sounding.html, last access: 08 April 2022). Areas with filtered radar measurements are marked using grey color.

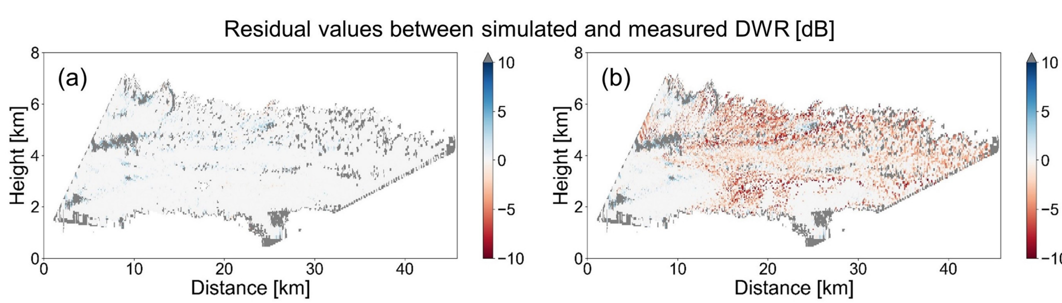

Figure 4.7: Difference (residuals) between simulated and measured values of DWR for ice spheroids that follow m(D_{max}) of (a) aggregates and (b) BF95 for 30 January 2019 at 10:08 UTC. For better visualization purposes the –5 ºC, –15 ºC and –25 ºC temperature lines are not plotted here. Areas with filtered radar measurements are marked using grey color.

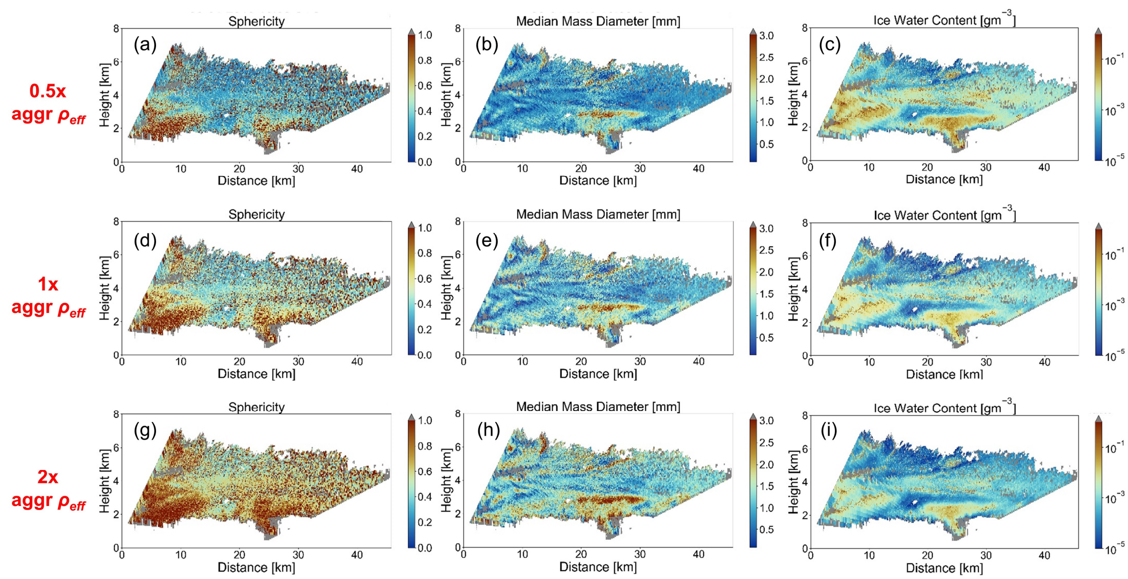

Figure 4.8: Ice microphysics results for 30 January 2019 at 10:08 UTC for oblate ice spheroids that follow an exponential PSD; sphericity, median mass diameter and ice water content using (a, b, c) 0.5x ρ_{eff}, (d, e, f) 1x ρ_{eff} and (g, h, i) 2x ρ_{eff} m(D_{max}) of aggregates from Yang et al. (2000). For better visualization purposes the –5 ºC, –15 ºC and –25 ºC temperature levels are not plotted here. Areas with filtered radar measurements are marked using grey color.

Table 4.3: RMSE values for simulated ZDR, DWR, Z_e compared to original observations for the whole radar cross-section after running the retrieval for 30 January 2019 at 10:08 UTC for oblate ice spheroids and different m(D_{max}) assumptions.

m(D_{max}) assumption for ice spheroids	**Parameter**	**RMSE**
BF95	DWR ZDR Z_e	2.27 dB 0.25 dB 0.20 dB
Aggregates Yang et al. (2000)	DWR ZDR Z_e	0.50 dB 0.19 dB 0.20 dB
Aggregates 2 times denser than Yang et al. (2000)	DWR ZDR Z_e	0.50 dB 0.21 dB 0.28 dB
Aggregates 0.5 times less dense than Yang et al. (2000)	DWR ZDR Z_e	0.54 dB 0.20 dB 0.23 dB

In the framework of the mass-size relation assumption investigation, a more homogenous atmospheric scene with a similar stratified radar reflectivity field with low Z_e at cloud top and higher Z_e towards the ML, was used. A homogeneous scene would be beneficial to test the performance of the ice retrieval as it could reveal unexpected retrieval behaviors caused by large discrepancies between the simulated and measured radar variables, especially when sensitivity studies using different assumptions about the shape, horizontal flutter, size and ice hydrometeors PSD properties, are conducted. The example case study from 10 January 2019 at 09:48 UTC was used throughout this but also the following sensitivity analyses and it is presented in Fig. 4.9. This case study refers to a snowfall that took place over Munich area that day and it is a simple example to test the performance of the developed ice retrieval (presented in Sect. 3.3), as well as to investigate in detail the output of sensitivity studies using different assumptions about the ice hydrometeors. Figure 4.9a and 4.9b show Z_e and ZDR measurements from POLDIRAD. In Fig. 4.9c, the DWR is drawn in the common radar grid, while in Fig. 4.9d the temperature sounding profile from Oberschleißheim station is shown (source: Deutscher Wetterdienst, data provided by University of Wyoming; http://weather.uwyo.edu/upperair/sounding.html, last access: 08 April 2022). Below 3 km height, at the –15 ºC isotherm, enhanced values of Z_e (> 5 dBZ) and DWR (> 5 dB) suggest the presence of large ice hydrometeors, while ZDR values between 0–1.5 dB indicate the presence of quite spherical ice particles.

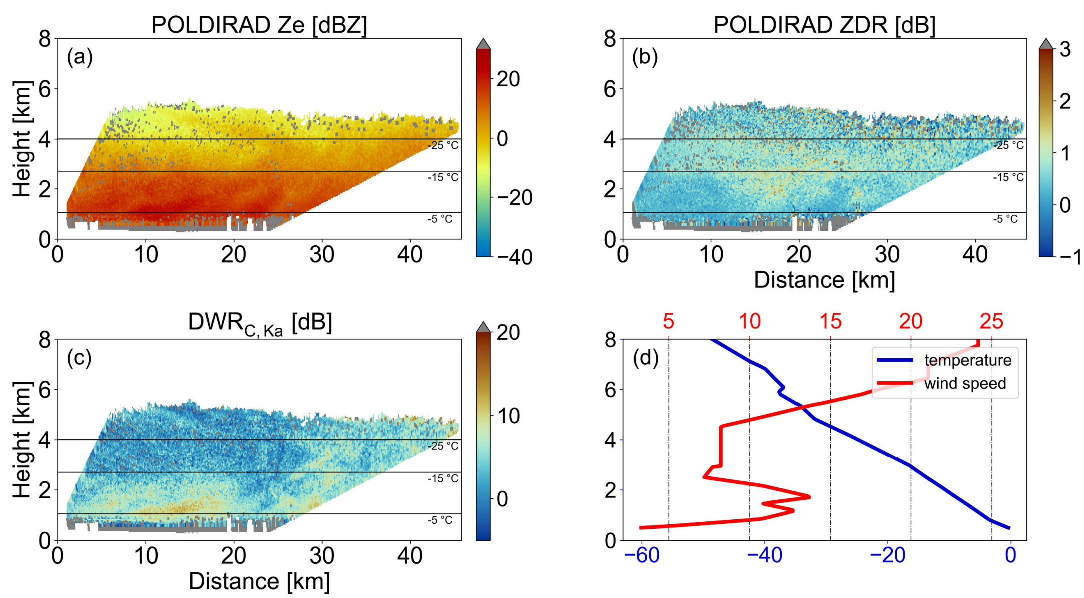

Figure 4.9: Filtered radar measurements of (a, b) POLDIRAD Z_e and ZDR as well as (c) DWR from 10 January 2019 at 09:48 UTC. Temperature data from Oberschleißheim sounding station are also plotted in the (d) panel (source: Deutscher Wetterdienst, data provided by University of Wyoming; http://weather.uwyo.edu/upperair/sounding.html, last access: 08 April 2022). With black solid lines the temperature levels of –5 ºC, –15 ºC and –25 ºC, are plotted. Areas with filtered radar measurements are marked using grey color.

After running the ice microphysics retrieval considering all the already discussed aspects in the radar observations, e.g., volumetric mismatch, the results using the aggregates was compared to this using the BF95 $m(D_{max})$. The results of this case study are presented in Fig. 4.10. Figure 4.10a shows larger averaged retrieved IWC when the BF95 (magenta color line) against the aggregates $m(D_{max})$ (orange color line) was used. The reason for this difference stems from the fact that the BF95 assumes less dense larger ice particles compared to the aggregates mass-size relation. Therefore, more ice spheroids would be needed assuming the BF95 than the aggregates $\mathrm{m}(\mathrm{D}_{\mathrm{max}})$ to match the measured Z_e. In Fig. 4.10b, a measurement density histogram for ZDR and DWR is presented. For the histogram only radar measurements performed with low elevation angles (< 4°) were used. In the same figure, lines for simulations with AR = 1.67, elevation angles $\theta_{\mathrm{C}} = \theta_{\mathrm{Ka}} = 0°$ and the aggregates (orange color line) as well as the BF95 (magenta color line) $\mathrm{m}(\mathrm{D}_{\mathrm{max}})$ were plotted. The low-density particles from the BF95 mass-size relation correspond to lower ZDR values and larger DWR than aggregates for a given median size, e.g., D_{m} = 0.5 mm. In this case, the aggregates $\mathrm{m}(\mathrm{D}_{\mathrm{max}})$ was found to represent the majority of the measurements as the orange solid line cuts better through the measurement distribution in the DWR-ZDR space. The difference of the mean averaged S, D_{m} and IWC between the two mass-size relation assumptions can be found in Table 4.4.

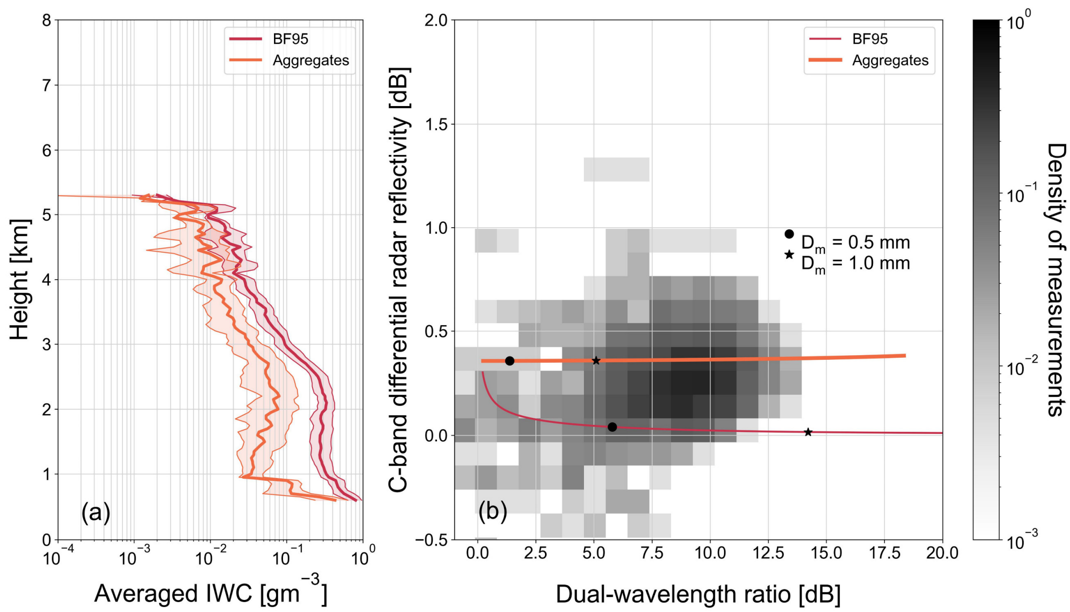

Figure 4.10: (a) Comparisons of averaged retrieved IWC for 10 January 2019 at 09:48 UTC and (b) ZDR-DWR histogram with measurement density for elevation angles < 4° along with scattering simulation lines with AR=1.67, elevation angles $\theta_{\mathrm{C}} = \theta_{\mathrm{Ka}} = 0°$, using aggregates and BF95 $\mathrm{m}(\mathrm{D}_{\mathrm{max}})$ and assuming oblate ice spheroids. The color-shaded areas indicate the estimated S, D_{m} and IWC uncertainties considered by the ±dDWR.

Mixing the $\mathrm{m}(\mathrm{D}_{\mathrm{max}})$ of aggregates with BF95

In a last step of the $\mathrm{m}(\mathrm{D}_{\mathrm{max}})$ analysis, combinations of the aggregates and the BF95 mass-size relation were used and the ice retrieval ran for the homogeneous case study from 10 January 2019 at 09:48 UTC. The combination of e.g., BF95 + aggregates $\mathrm{m}(\mathrm{D}_{\mathrm{max}})$ is implemented as follows and the procedure is similar for all other $\mathrm{m}(\mathrm{D}_{\mathrm{max}})$ combinations. The masses of the simulated sizes of the ice spheroids are calculated using the two different $\mathrm{m}(\mathrm{D}_{\mathrm{max}})$; here for BF95 and aggregates. Then, for each selected simulated maximum diameter, the two mass arrays are compared. As the PyTmatrix and the soft spheroid model are known to underestimate the simulated polarimetric signal of merely fluffy ice particles, the denser particles, i.e., particles with higher density, were chosen to be in the final mass array which was then used for the scattering calculations. For BF95, smaller ice spheroids of the PSD were found to have higher density than assuming the aggregates mass-size relation (Fig. 2.2) and thus, the BF95 spheroids were chosen. However, BF95 suggests a strong density decrease with size. For all sizes larger than a critical size, where the density of BF95 becomes lower than aggregates spheroids, the aggregates $m(D_{max})$ spheroids were selected. Then, the scattering simulations were calculated for the whole PSD consisted from BF95 and aggregates spheroids. Here, Fig. 4.11 is also introduced, to give a comprehensive idea about the density of the simulated ice spheroids using the different $m(D_{max})$ combinations.

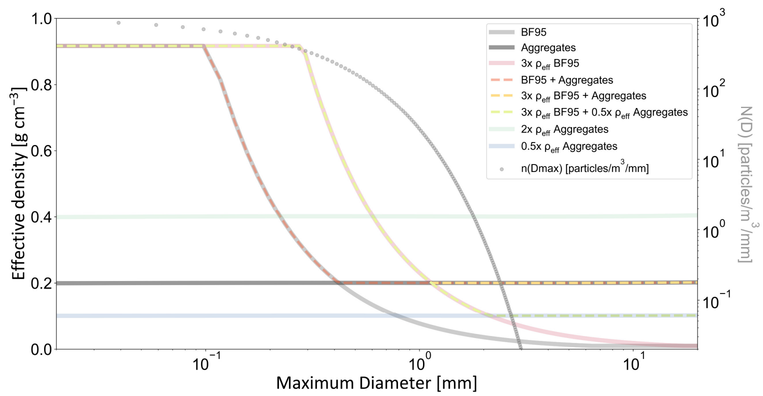

Figure 4.11: Comparisons of different mass-size relation combinations for ice particles with AR=1.67. With light grey scatters the exponential size distribution (D_m = 0.5 mm) used for the oblate ice spheroids is plotted.

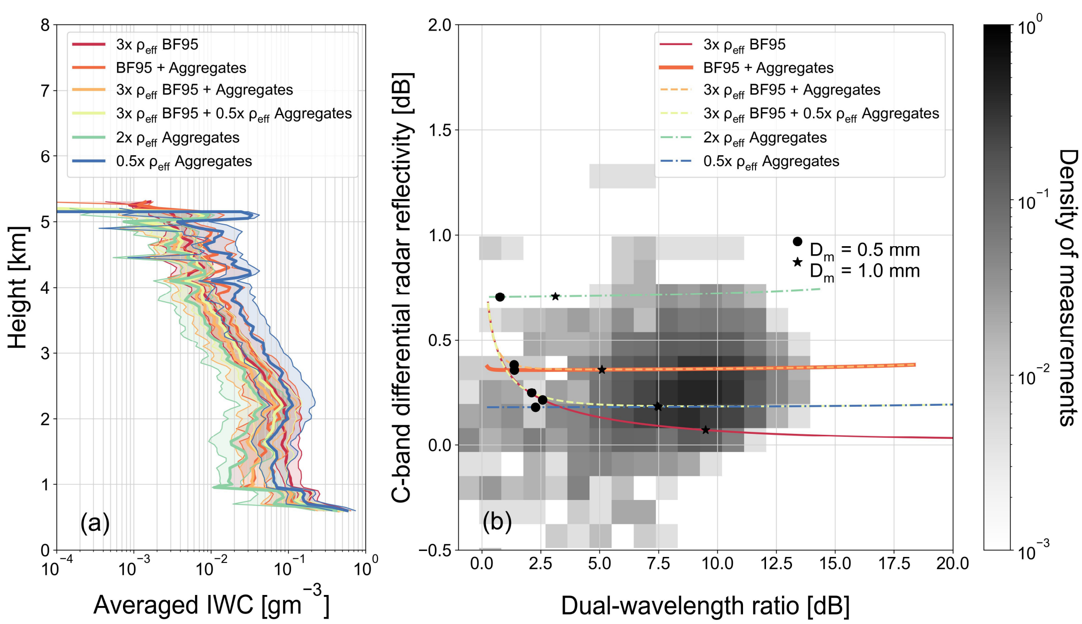

Figure 4.12: (a) Comparisons of averaged retrieved IWC for 10 January 2019 at 09:48 UTC and (b) ZDR-DWR histogram with measurement density for elevation angles < 4° along with scattering simulation lines with AR=1.67, elevation angles $\theta_C = \theta_{Ka} = 0°$, using different combinations of BF95 and aggregates $m(D_{max})$ and assuming oblate ice spheroids. The color-shaded areas indicate the estimated S, D_m and IWC uncertainties considered by the ±dDWR.

In Fig. 4.12 more results of the sensitivity study based on the assumed mass-size relations from Fig. 4.11 are presented. In this part, BF95 was further explored by combining it with the aggregates mass-size relation trying to answer the following question: “Can two modified mass-size relations be combined to obtain denser particles as aggregates that better explain the radar dataset?”. In Fig. 4.12b, it becomes obvious that a large part of the radar measurements can be explained using spheroids that follow the combined 3x ρ_{eff} BF95 + 0.5x ρ_{eff} aggregates $\mathrm{m(D_{max})}$ (yellow dashed color line) or the 0.5x ρ_{eff} aggregates $\mathrm{m(D_{max})}$ (blue dash-dotted color line) as these lines cut better through the measurement distribution in the DWR-ZDR space. The difference and intercomparisons of the mean averaged S, D_{m} and IWC for all the mixed mass-size relations are presented in Table 4.4, while a discussion on these results can be found in Sect. 5.1.

Table 4.4: Summarized intercomparisons of the retrieval results for 10 January 2019 at 09:48 UTC from sensitivity studies on the mass-size relation of the simulated ice hydrometeors using soft spheroids.

$\mathbf{m(D_{max})}$ assumption for ice spheroids	ΔS	ΔD_{m} [mm]	ΔIWC [g m^{-3}]
aggregates vs. BF95	0.31	0.48	–0.130
BF95 vs. 3x ρ_{eff} BF95	–0.12	–0.24	0.115
aggregates vs. BF95 + aggregates	0.00	0.00	–0.001
BF95 + aggregates vs. 3x ρ_{eff} BF95 + aggregates	–0.02	–0.01	0.007
3x ρ_{eff} BF95 + aggregates vs. 3x ρ_{eff} BF95 + 0.5x ρ_{eff} aggregates	0.11	0.16	–0.012
aggregates vs. 2x ρ_{eff} aggregates	–0.14	–0.23	0.015
aggregates vs. 0.5x ρ_{eff} aggregates	0.13	0.16	–0.024

4.2.2 Particle size distribution PSD

In the next step, the effect of the width parameter μ of PSD on the ice microphysics results was investigated. Previous studies, e.g., Field and Heymsfield (2003), Tiira et al. (2016), Matrosov and Heymsfield (2017) and many more, suggest that μ in the gamma PSD for snow and ice particles can be close to 0, leading to the assumption of an exponential PSD. In the framework of the sensitivity analysis, a gamma PSD with $\mu = 4$ was additionally investigated. Figure 4.13 and 4.14 show ice microphysics results from 10 January 2019 at 09:48 UTC using $\mu = 0$ and $\mu = 4$, assuming the aggregates mass-size relation and oblate ice spheroids. Between Fig. 4.13a, 4.13c, 4.14a and 4.14c (i.e., shape retrieval) no significant differences were observed. However, Fig. 4.13b shows smaller retrieved D_{m} against Fig. 4.14b, clearly seen above the isotherm of –15 ºC. On the contrary, the retrieved IWC using $\mu = 0$ in the gamma PSD was slightly greater than the retrieved IWC assuming $\mu = 4$ in the gamma PSD. A detailed explanation about these results can be found in Sect. 5.1. Differences between both width parameter assumptions are shown in Table 4.5.

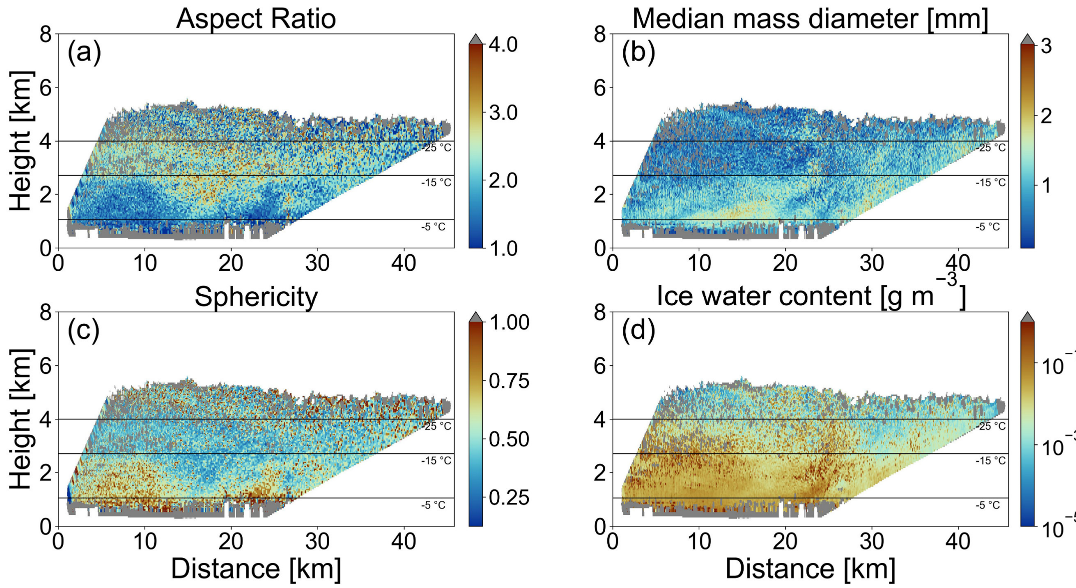

Figure 4.13: Ice microphysics retrieval results for (a) AR, (b) D_m, (c) S and (d) IWC for 10 January 2019 at 09:48 UTC, $\mu = 0$, aggregates m(D_{max}) and assuming oblate ice spheroids. With black solid lines the temperature levels of –5 ºC, –15 ºC and –25 ºC, are plotted (source: Deutscher Wetterdienst, data provided by University of Wyoming; http://weather.uwyo.edu/upperair/sounding.html, last access: 08 April 2022). Areas with filtered radar measurements are marked using grey color.

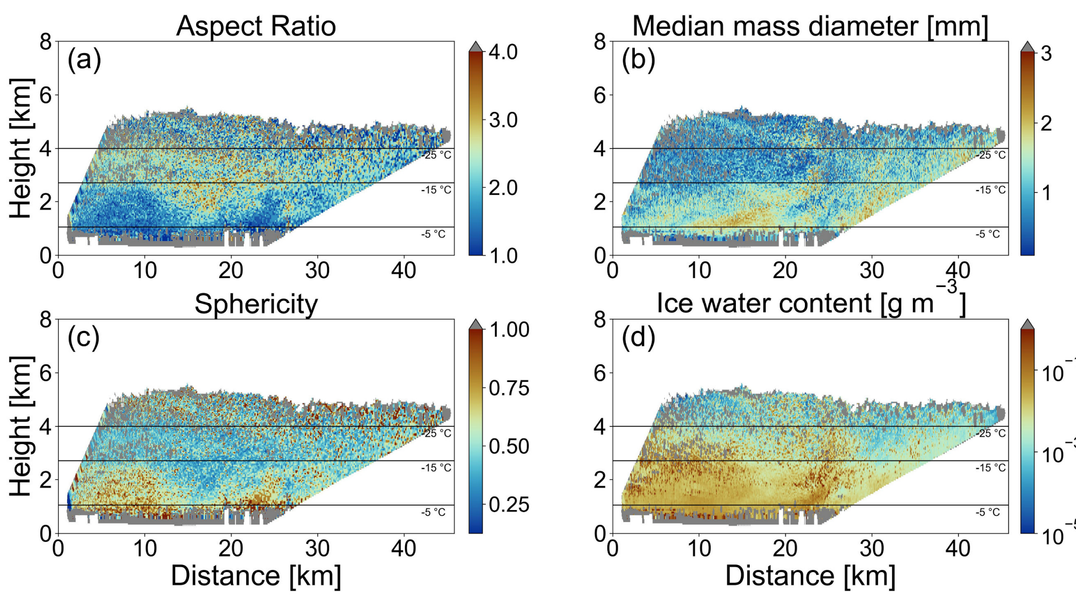

Figure 4.14: Ice microphysics retrieval results for (a) AR, (b) D_m, (c) S and (d) IWC for 10 January 2019 at 09:48 UTC, $\mu = 4$, aggregates m(D_{max}) and assuming oblate ice spheroids. With black solid lines the temperature levels of –5 ºC, –15 ºC and –25 ºC, are plotted (source: Deutscher Wetterdienst, data provided by University of Wyoming; http://weather.uwyo.edu/upperair/sounding.html, last access: 08 April 2022). Areas with filtered radar measurements are marked using grey color.

Table 4.5: Summarized intercomparisons of the retrieval results for 10 January 2019 at 09:48 UTC from sensitivity studies on the particle size distribution of the simulated ice hydrometeors using soft spheroids.

PSD assumption for ice spheroids	ΔS	ΔD_m [mm]	ΔIWC [g m^{-3}]
$\mu = 0$ vs. $\mu = 4$	0.00	–0.20	0.008

4.2.3 Horizontal flutter of falling ice particles

In this study, all simulated ice spheroids were assumed to fall with their maximum dimension parallel to the horizontal plane. However, it has been observed in nature that ice particles can tumble around this plane. The angle between the major dimension of the particle and the horizontal plane, i.e., canting angle, varied between 0° and 90° for oblate and horizontally aligned prolate spheroids, respectively, in the present work.

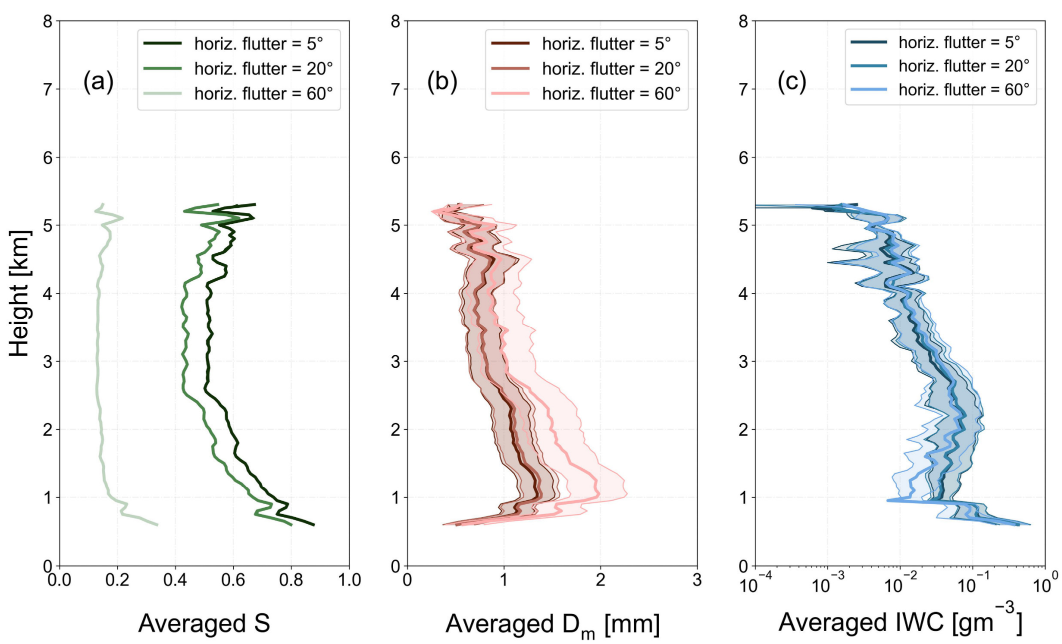

Figure 4.15: Comparisons of averaged retrieved (a) S, (b) D_m and (c) IWC for 10 January 2019 at 09:48 UTC, using oblate spheroids that follow the aggregates m(D_{max}), an exponential PSD and assuming 5°, 20° and 60° horizontal flutter. The color-shaded areas indicate the estimated S, D_m and IWC uncertainties considered by the ±dDWR.

Inside the measurement volume the flutter of all ice particles is not synchronized. Therefore, the whole distribution of canting angles can be found inside the measured volume. All these canting angles of ice crystals need to be represented using an average canting angle. This simplification raises the need for an additional standard deviation value (e.g., 2°–23° as in Melnikov, 2017). In the present doctoral study a standard deviation of 20° has been used so far to represent the tumbling of the particles maximum dimension around the selected canting angle. In the framework of the sensitivity analysis, the effect of two more standard deviation values, i.e., 5° and 60°, was investigated for the ice microphysics retrieval results. Figure 4.15 shows retrieval results for the three horizontal flutter assumptions using oblate spheroids that follow aggregates $\mathrm{m(D_{max})}$ and an exponential PSD, while Table 4.6 summarizes the results of the mean S, D_{m} and IWC for the aforementioned assumptions. A detailed discussion for the output of this sensitivity study can be found in Sect. 5.1.

Table 4.6: Summarized intercomparisons of the retrieval results for 10 January 2019 at 09:48 UTC from sensitivity studies on the horizontal flutter of the simulated ice hydrometeors using soft spheroids.

Horizontal flutter assumption for ice spheroids	mean S	mean D_{m}	mean IWC
5°	0.60	0.89	0.048
20°	0.52	0.90	0.049
60°	0.16	1.15	0.041

4.2.4 Oblates and horizontally aligned prolates ice spheroids

Particle size distribution, horizontal flutter, mass-size relation and oblate or prolate assumption can all influence the results of the ice microphysics retrieval. In Sect. 4.1, results of the ice microphysics retrieval for oblate and prolate assumption were presented. From Fig. 4.1 and 4.2, it becomes clear that the oblate/prolate assumption can slightly influence the retrieved parameters. Here, this assumption is investigated using a more homogeneous case study.

The averaged retrieval results for the 10 January 2019 at 09:48 UTC using oblate or horizontally aligned prolate spheroids to represent the ice hydrometeors are presented in Fig. 4.16. It is worth to be again noted here that, for the scattering simulations AR values of 0.125, 0.16, 0.21, 0.27, 0.35, 0.45, 0.6, 0.8, 1.0 for horizontally aligned prolate ice spheroids and the inverted values for oblate ice spheroids with a maximum AR = 8.0, were considered. For ice oblates, the averaged retrieved S and D_{m} (Fig. 4.16a and 4.16b) were smaller than when horizontally aligned ice prolates were used. The opposite was observed for the averaged retrieved IWC (Fig. 4.16c). Differences between the oblate and prolate assumption can be found in Table 4.7.

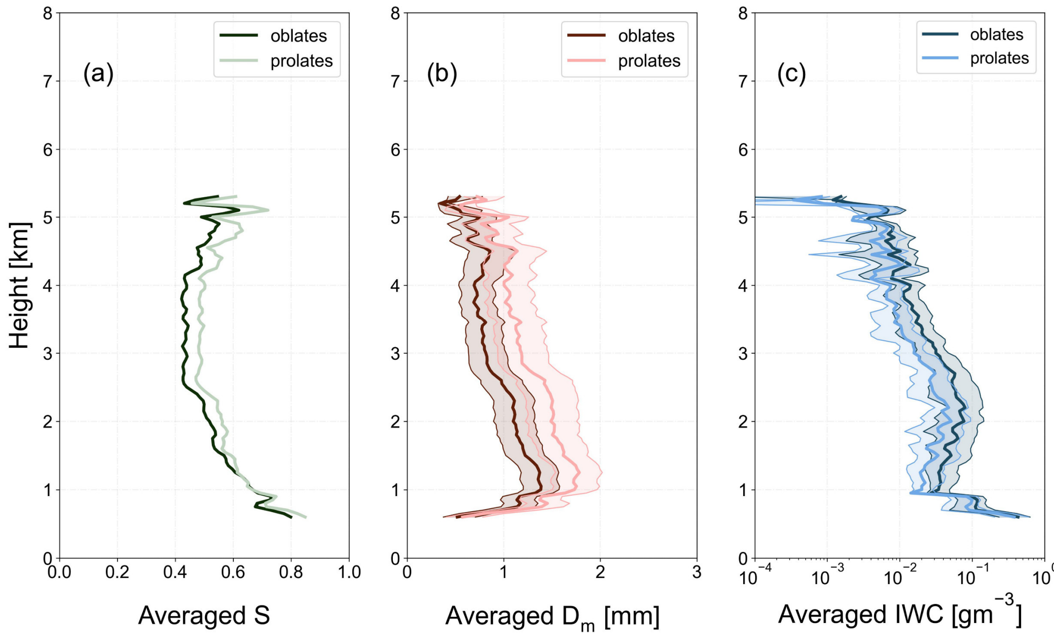

Figure 4.16: Comparisons of averaged retrieved (a) S, (b) D_m and (c) IWC for 10 January 2019 at 09:48 UTC, using oblate and prolate assumption as well as aggregates m(D_{max}) and an exponential PSD. The color-shaded areas indicate the estimated S, D_m and IWC uncertainties considered by the ±dDWR.

Table 4.7: Summarized intercomparisons of the retrieval results for 10 January 2019 at 09:48 UTC from sensitivity studies on the shape of the simulated ice hydrometeors using soft spheroids.

Oblate/prolate as well as aspect ratio assumption for ice spheroids	ΔS	ΔD_m [mm]	ΔIWC [g m^{-3}]
oblate vs. horizontally aligned prolate	–0.04	–0.32	0.014

Chapter 5

5 Discussion

This section contains work, which has already been published by Tetoni et al. (2022) in Atmospheric Measurement Techniques (AMT), entitled *"Retrievals of ice microphysical properties using dual-wavelength polarimetric radar observations during stratiform precipitation events"*.

After the development of the ice microphysics retrieval, several sensitivity studies were conducted aiming to investigate the effect of the assumed microphysics on the output of the retrieval. One limitation of the current version of the ice retrieval algorithm is the need to make some assumptions about the ice particle properties. At first, the spheroid model was selected to represent the ice hydrometeors, due to the small number of free parameters needed to describe the simulated ice particles. Then, the type of PSD that the ice spheroids would follow was chosen. For this assumption, several studies argue that a typical PSD is described by a width parameter close to 0 for low-density ice particles (e.g., Tiira et al., 2016). In this study, an exponential PSD was chosen for the simulated ice spheroids used for the scattering calculations. However, comparisons between retrieval results assuming an exponential and a gamma PSD were presented in Sect. 4.2.2 and will be further discussed in this chapter. The third assumption considered the choice of oblate or horizontally aligned prolate ice spheroids. In addition to the oblate or prolate assumption, a fourth assumption about a suitable $m(D_{max})$ relationship for the prevalent ice particles was needed. For the three investigated snow events the selection of the aggregates over the BF95 $m(D_{max})$ for ice spheroids has been briefly discussed in Sect. 4.2.1, but an extended explanation for this selection will be also presented in Sect. 5.1. Next to the aforementioned assumptions, a horizontal flutter of 20° around the selected canting angle has been used so far for the ice spheroids but in the framework of the sensitivity analysis, the effect of other values on the ice retrievals will be also investigated. In Sect. 5.2, the contribution of polarimetric measurements, i.e., ZDR, for this study will be shown while in Sect. 5.3, retrieval results will be evaluated with respect to other retrieval algorithms. In the last section further thoughts on the use of the developed ice microphysics retrieval will be presented.

5.1 How does each assumption affect the results of the ice retrieval?

In this section, all findings of the sensitivity studies conducted for this thesis are discussed. These findings refer to different assumptions in the scattering simulations of the ice spheroids used for the development of the ice microphysics retrieval.

Soft spheroid approximation

Although more complex ice particle and scattering models are available, the soft spheroid approximation was used in this doctoral thesis and the reasons for this selection are the following: *(1)* One of the goals of this work is to investigate the possibility to combine two spatially separated radars to better constrain the ice crystal shape in microphysical retrievals using simultaneous DWR and ZDR observations from an oblique angle. Besides the instrument coordination, the actual measurements and the assessment of measurement errors, the ice crystal and scattering model are just one component. This work utilized the soft spheroid approximation to study the benefit of additional ZDR measurements and the role of the observation geometry due to its simple, fast and versatile setup. *(2)* More importantly, to my knowledge, the more accurate SSRGA described by Hogan and Westbrook (2014) does not provide polarimetric variables used in this study, i.e., ZDR, yet. *(3)* In anticipation of a prognostic aspect ratio of ice crystals in bulk microphysical models (e.g., the adaptive habit prediction; Harrington et al., 2013), a minimal set of degrees of freedom was kept here to remain comparable with these modelling efforts. *(4)* Using ice spheroids, the varying of different parameters such as median size, aspect ratio and ice water content independently, was possible. The calculation of the varied optical properties of soft spheroids was possible without much computational cost as using other scattering algorithms (e.g., DDA) which are exploited for more realistic ice crystal shapes simulations. Moreover, using spheroids the ambiguities between these simple, aforementioned degrees of freedom could be better understood. The simplification of representing ice particles with soft spheroids caused an underestimation of the radar backscatter, and ZDR especially, for low-density snowflakes (e.g., Schrom and Kumjian, 2018), due to the missing internal structure of the reduced-density spheroids. This, limited this study to ice aggregates with sizes in the millimeter regime, including the onset of ice aggregation within clouds above the melting layer (ML) but excluding heavy snowfall close to the ground. Nevertheless, the latter region was rarely included in the measurement region with an overlap between the two scanning radars.

After interesting discussions with members of the scientific community with experience in ice scattering simulations, the scattering properties of the ice spheroids that follow a mass-size relation according to the aggregates from Yang et al. (2000) were compared to ice aggregates from a scattering database provided by Atmospheric Radiation Measurement (ARM; described in Lu et al., 2016; data available with identifier doi: https://doi.org/10.5439/1258029, Aydin et al., 2016). In particular, the polarimetric signal, i.e., ZDR, of the soft spheroids was compared to the one of the low-density ARM aggregates (i.e., the LD-P1d type), calculated at X band with λ = 31.9 mm provided by ARM as the closest value to the C band λ = 54.5 mm used in this study. The comparison showed that, only when the ice spheroids were assumed to have 2x ρ_{eff} aggregates $\mathrm{m}(\mathrm{D}_{\mathrm{max}})$ from Yang et al. (2000), the calculated ZDR for the soft ice spheroids from the T-Matrix could approach the one calculated for the ARM aggregates. When the soft spheroids were assumed to have the original effective density of aggregates, they produced approximately 1 dB lower ZDR values than that calculated for the ice aggregates of the ARM scattering database which are simulated with the Generalized Multiparticle Mie method (GMM). Here, it is important to note that the discrepancies observed between the ice spheroids and the ARM aggregates scattering properties occur due to the fact that in this study only the maximum dimension and the mass of aggregates from Yang et al. (2000) was borrowed, and not the internal structure of these particles. The soft spheroid model used here suggests homogeneity in the mass distribution over the whole volume of the spheroids and thus, reduced-density particles are used to represent realistic habits, i.e., aggregates, with the same maximum dimension. The ice spheroids produce lower simulated ZDR values due to the reduced-density and therefore, lower ZDR values are found for the homogeneous soft spheroids in contrast to more realistic ice habits (e.g., Schrom and Kumjian, 2018).

Mass-size relation $\mathrm{m}(\mathrm{D}_{\mathrm{max}})$

One of the most significant assumptions that had to be made in the present doctoral thesis was about the mass-size relation that the simulated ice hydrometeors would follow. The mass contained in the ice spheroids plays a leading role for the scattering properties as it is used to define the effective density ρ_{eff} of the simulated ice particles. Although the mass for water droplets is easy to estimate for a given size using the known density of water, the estimation of ice crystals mass remains a tough task in ice clouds studies. Hence, when particles simulations are performed in such studies, one has to assume a mass-size relation formula that describes the total ice mass as a function of the particle size. Such formulas are usually generated from in situ data (e.g., Heymsfield et al., 2010; Cotton et al., 2013; Erfani and Mitchell, 2016; Tiira et al., 2016 and many more).

In this thesis the way that the selected mass-size relation can affect the results of the ice microphysics retrieval was investigated in detail. The output of this investigation was presented in Chapter 4 and in particular in Sect. 4.2.1. At first, retrieval results using two established mass-size relations, i.e., the aggregates from Yang et al. (2000) as well as the BF95 from Brown and Francis (1995) as presented in Hogan et al. (2012), with the same assumptions for PSD and the same simulated aspect ratio, median size and ice water content values of the ice spheroids, were compared. From the aforementioned mass-size relations, only the aggregates could reasonably explain the radar observations during three snowfall events in winter 2019 over Munich. Particularly, for a selected case study from 30 January 2019 at 10:08 UTC, the RMSE for the whole cloud cross-section for Z_{e}, ZDR and DWR were found to be 0.20 dB, 0.19 dB and 0.50 dB, respectively, when the oblate ice spheroids followed the aggregates $\mathrm{m}(\mathrm{D}_{\mathrm{max}})$, against to 0.20 dB, 0.25 dB and 2.27 dB, when the oblate ice spheroids followed the BF95 $\mathrm{m}(\mathrm{D}_{\mathrm{max}})$. Figure 2.2, but also Fig. 4.11 with logarithmic horizontal axis, shows that BF95 assumes a fast decrease of the ice particle effective density with increasing size due to the exponent b = 1.9, while the aggregates formula assumes an almost constant effective density with size (also shown in the same figures). The fast decrease of ρ_{eff} for BF95 in combination with the soft spheroid model used to represent the ice hydrometeors, results to very low effective density values for larger ice particles and in turn, low simulated ZDR values, leading to large discrepancies between the measured and simulated radar variables, especially when it comes to polarimetric signals. Although simple and versatile, the soft spheroid model is known to underestimate polarimetric signal of very light particles due to the missing internal structure.

To further examine the mass-size relation assumption, more combinations of aggregates and BF95 $\mathrm{m}(\mathrm{D}_{\mathrm{max}})$ were investigated. In Table 4.4, intercomparisons between the different mass-size relations were presented. In the special case of aggregates vs. BF95 + aggregates $\mathrm{m}(\mathrm{D}_{\mathrm{max}})$, no difference between the mean averaged retrieved S and D_{m} was calculated, while a small difference of –0.001 g m^{-3} was calculated for the mean averaged retrieved values of IWC. In Sect. 4.1 (subsection Mixing the $\mathrm{m}(\mathrm{D}_{\mathrm{max}})$ of aggregates and BF95), the construction of the BF95 + aggregates $\mathrm{m}(\mathrm{D}_{\mathrm{max}})$ was described. The fast and sharp decrease of the density that the BF95 $\mathrm{m}(\mathrm{D}_{\mathrm{max}})$ suggests, leads to the use of the aggregates $\mathrm{m}(\mathrm{D}_{\mathrm{max}})$ "early" in size within the PSD and therefore, for larger particles or larger median sizes of PSD, the aggregates is merely used or – in other words – contributes the most to the scattering properties of the simulated PSD. This effect can be observed in Fig. 4.10b and 4.12b, where the aggregates and the BF95 + aggregates $\mathrm{m(D_{max})}$ produce the same polarimetric signal, i.e., ZDR. For the presented homogeneous case study from 10 January 2019 at 09:48 UTC, only a few ice hydrometeors populations with small sizes were detected in the total cloud cross-section, leading to no differences between the mean averaged retrieved microphysical properties.

Figure 5.1 shows a marginal histogram (2D data histogram with two additional 1D histograms describing the data distribution in each dimension ignoring the other) with ZDR-DWR measurements density from 10 January 2019 at 09:48 UTC. In the same plot, simulation lines using different assumptions of mass-size relation are plotted. For the density histogram, measurements up to 4° elevation angles from both radars were used, while simulations were done for horizontal beam's emission in both radar bands and for ice spheroids that follow an exponential PSD and AR=1.67. Central panel in Fig. 5.1 is accompanied with occurrence histograms for ZDR and DWR measurements. From the plot it is obvious that some simulation lines with $\mathrm{m(D_{max})}$, e.g., the 3x ρ_{eff} BF95 + 0.5x ρ_{eff} aggregates or the 0.5x ρ_{eff} aggregates, can already approach the higher measurements-density area in the 2D histogram, while the 3x ρ_{eff} BF95 + aggregates or BF95 + aggregates $\mathrm{m(D_{max})}$ are also quite close to this higher measurement-density area. Figure 5.1 indicates that the mass-size relation assumption is not so straightforward to be constrained for ice cloud particles, especially when in situ data are not available as in this case.

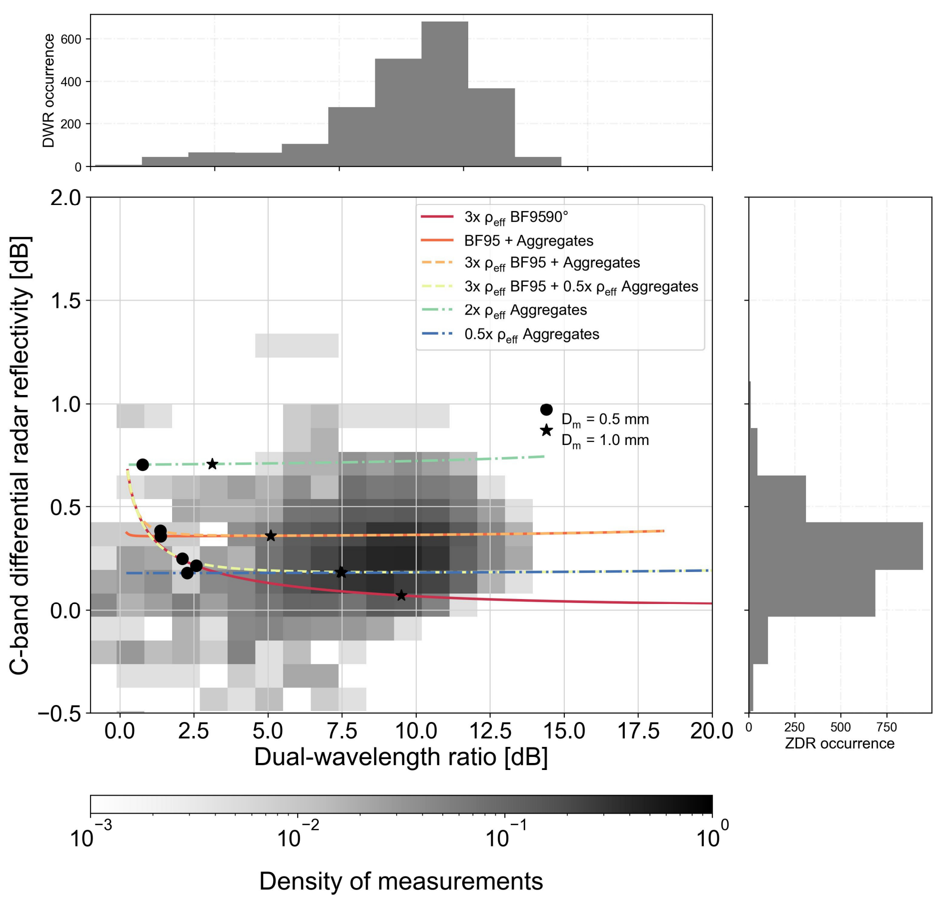

Figure 5.1: ZDR-DWR measurement density histogram with two additional ZDR and DWR occurrence histograms (marginal histograms) for 10 January 2019 at 09:48 UTC for elevation angles < 4° along with scattering simulation lines with AR=1.67, elevation angles $\theta_C = \theta_{Ka} = 0°$, using combinations of aggregates and BF95 m(D_{max}) and an exponential PSD.

The same is also obvious from Fig. 5.2 where again a marginal histogram with ZDR-DWR measurements density from 30 January 2019 at 10:08 UTC is plotted. For the density histogram, measurements between 6°–8° elevation angles from both radars were used as the cloud was detected at higher altitude that day. The simulations were done again for horizontal beam's emission in both radar bands, for ice spheroids that follow an exponential PSD and AR=1.67, as no significant differences were observed in the simulated radar variables for the selected AR value.

In both examples, it is obvious that a fixed $\mathrm{m(D_{max})}$ cannot fully capture the ice particles variability found in nature. For this reason, additional measurements (e.g., Doppler velocity or in situ data) could be exploited to provide additional density information. In this way, the fixed $\mathrm{m(D_{max})}$ assumption used here could be replaced with a set of mass-size relations, or even combinations of them, depending on the average ice particles density, a parameter which is affected by the environment in which the ice particles are formed.

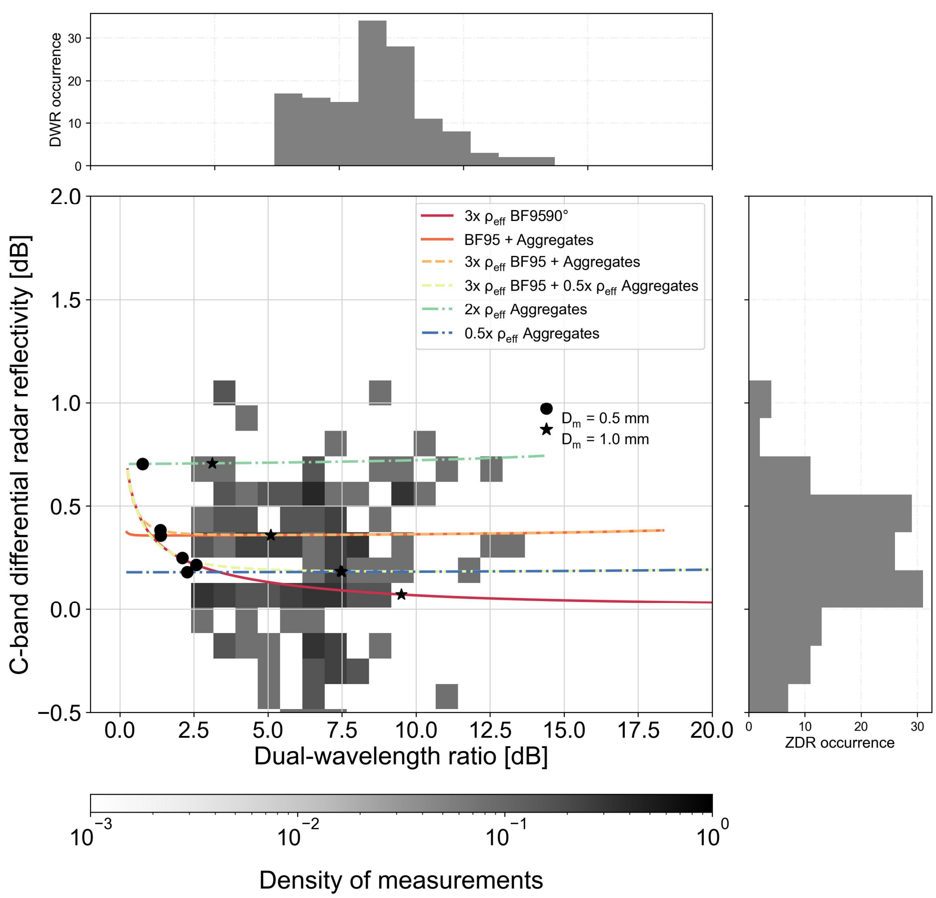

Figure 5.2: Same as Fig. 5.1 but for 30 January 2019 at 10:08 UTC and elevation angles 6°–8°.

Particle size distribution PSD

Atmospheric hydrometeors are found to follow different types of particle size distributions, e.g., exponential, gamma, bimodal, lognormal, in nature. Hence, the PSD is a very important parameter to be defined for the development of microphysics retrievals.

In the special case of ice hydrometeors, whose representation is crucial in numerical weather and climate models, the particle size distribution is a significant component and thus, it has been investigated in several studies. To constrain this parameter within clouds, one common approach is to use in situ observations from probes during aircraft flights (e.g., Matrosov and Heymsfield, 2017). As such data were not available for the analyzed time period in this study, an assumption for the PSD width parameter μ was made. The exponential PSD or a PSD with width parameter close to 0 has been used in several ice studies (Gunn and Marshall, 1958; Lo and Passarelli, 1982; Field and Heymsfield, 2003; Tiira et al., 2016). Hence, an exponential particle size distribution (Eq. 2.6 with $\mu = 0$) was also chosen in the scattering calculations of the present study.

During the sensitivity analysis, a different type of PSD, i.e., a gamma PSD, was also investigated. Recent studies conducted during flights within tropical cyclones showed that gamma particle size distributions can better represent ice particle populations than exponential particle size distributions (Leighton et al., 2020). Therefore, a PSD with a width parameter $\mu = 4$ was used and LUTs were generated with all other assumptions staying fixed (oblate ice spheroids, aggregates mass-size relation). Then, the ice microphysics retrieval ran for the homogeneous case study from 10 January 2019 at 09:48 UTC (Fig. 4.14). Figure 5.3 shows how the number concentration of particles is distributed with size, using a PSD with the same median size and different width parameter. In the case of $\mu = 0$ the distribution is broader with more smaller particles and more larger particles, in contrast to $\mu = 4$ when the distribution is narrower. The exponential PSD leads to larger simulated Z_e and DWR values when the same median size and ice water content of the PSD is assumed. The reason for this can be seen in Fig. 5.3 where more particles larger in size are included in the exponential rather than in gamma PSD. For instance, Z_{e_C} = 17.95 dBZ, $Z_{e_{Ka}}$ = 16.61 dBZ, DWR = 1.34 dB and ZDR = 0.36 dB for $\mu = 0$, while Z_{e_C} = 16.47 dBZ, $Z_{e_{Ka}}$ = 15.60 dBZ, DWR = 0.87 dB and ZDR = 0.36 dB for $\mu = 4$ when AR=1.67, D_m = 0.5 mm and IWC = 0.5 g m^{-3}. Therefore, the retrieved D_m for $\mu = 0$ has to be smaller compared to the D_m for $\mu = 4$ to explain the same measured values of DWR. This effect can be seen in Fig. 4.13b and 4.14b. The opposite applies for the retrieved IWC. For the same measured Z_e, IWC needs to be larger for $\mu = 0$ as the retrieved median size is smaller compared to these needed for $\mu = 4$. This is also shown in Fig. 4.13d against Fig. 4.14d, where higher values of IWC are retrieved for $\mu = 0$ than $\mu = 4$. As the radar reflectivity is proportional to the number concentration N and the particle size to the sixth power (D^6), and the ice water content is proportional to the number concentration N and the particle size to the third power (D^3), consequently the radar reflectivity is proportional to the ice water content and the particle size to the third power. This means that for larger ice water content, the particle size must be smaller to explain the same radar reflectivity. This statement (*higher IWC-smaller size/lower IWC-larger size*) will be used throughout the sensitivity analyses to explain the retrieval results.

Using the ice microphysics retrieval output assuming $\mu = 0$ as reference results (Fig. 4.13), the percent bias in the retrieval output assuming $\mu = 4$ was calculated, using the following formula:

$$bias = \frac{result_{\mu=0} - result_{\mu=4}}{result_{\mu=0}} \cdot 100\ \% \tag{5.1}$$

The results for aspect ratio, median mass diameter, sphericity and ice water content following this approach can be found in Fig. 5.4. Since sphericity is a derivative of aspect ratio, the difference is the same in both plots (Fig. 5.4a and 5.4c) and significantly low as the ZDR is the same for both PSD assumptions. More pronounced differences are observed for median mass diameter and ice water content, i.e., larger than 20%, throughout the whole cloud cross-section. Here, the negative bias of D_m and the positive bias of IWC highlight again the aforementioned statement about *higher IWC-smaller size/lower IWC-larger size*.

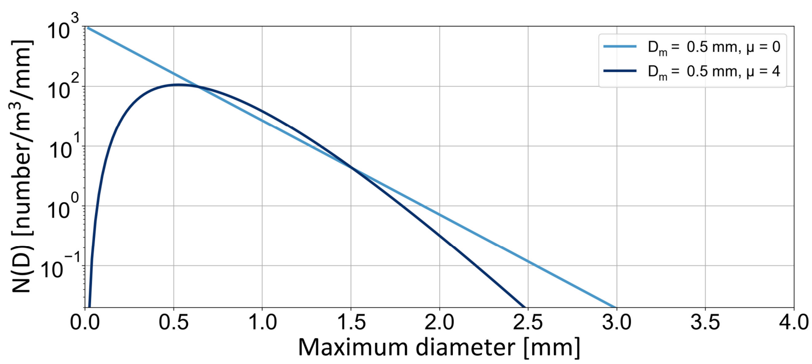

Figure 5.3: Particle size distribution for ice spheroids and different width parameter values ($\mu = 0$ and $\mu = 4$).

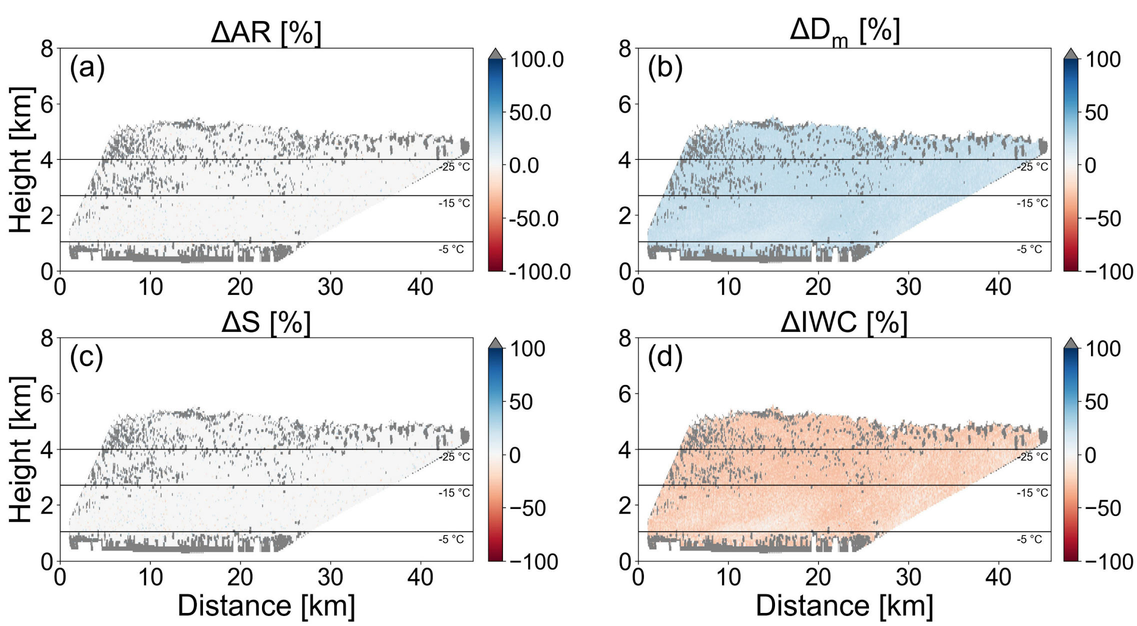

Figure 5.4: Percent difference in the retrieval results from 10 January 2019 at 09:48 UTC assuming $\mu = 0$ and $\mu = 4$ in the particle size distribution.

Horizontal flutter of ice spheroids

For the majority of the ice scattering simulations it was assumed that all ice spheroids are horizontally oriented with a fixed standard deviation of 20° to describe the tumbling of their maximum dimension around the selected canting angle. The calculation of the scattering properties in PyTMatrix was performed using an integration technique for all possible geometries of the particles, ignoring the α and β Euler angles of the scattering orientation. In the framework of the sensitivity analysis, a standard deviation of 5° and 60° was additionally used to describe the flutter out of the horizontal plane.

The lowest standard deviation assumption (5°) resulted in larger values of the simulated polarimetric radar variables, i.e., differential radar reflectivity, in contrast to 20°, because the particles were oriented almost horizontally. The opposite was observed for the largest standard deviation assumption (60°) because the particle orientations deviated more from the horizontal plane leading to lower simulated ZDR. The aforementioned differences in the standard deviation of the canting angle, had a great impact on the retrieved shape and much less on the retrieved size and mass – at least for the 5° and 20° standard deviation assumptions. This can be clearly seen in Fig. 4.15. The larger the standard deviation, the smaller the obtained sphericity and thus, more aspherical particles were retrieved. In other words, as the simulated ZDR becomes lower, i.e., for larger values of the standard deviation of the canting angle, ice spheroids need to be more elongated and thus, more aspherical to produce larger simulated ZDR that match the measured one. For the largest standard deviation assumption (60°) it becomes apparent that the lowest average retrieved S vertical profile leads to larger average retrieved D_m vertical profile compared to 5° and 20° standard deviation. The influence of the different standard deviation assumption around the selected canting angle is not that significant for the retrieval of IWC in this case. Nevertheless, one should be careful to choose a standard deviation value for the canting angle from a reasonable range suggested from literature (e.g., Melnikov, 2017).

Oblates and horizontally aligned prolates ice spheroids

The oblate or prolate assumption in the ice spheroid model has an impact on the simulated radar variables. It is helpful to remind again here, that oblate ice spheroids can be considered as lentil-like particles, while horizontally aligned prolate ice spheroids can be considered as rice-like particles.

When oblates are used as a reference for bias calculations using Eq. (5.1) and when both beams are emitted horizontally, Z_{e_C} for prolates with same S and mass is not significantly smaller than Z_{e_C} for oblates. In contrast, $Z_{e_{Ka}}$ is measurably smaller for oblates in this comparison. The reason for this difference is shown in Fig. 5.5. At the top of this figure, the side perspectives of oblate and horizontally aligned prolates are presented when they are azimuthally rotated around the z axis. The grey scale shows the distribution of the cross-sectional areas of the ice spheroids exposed to the incident beam for all azimuthally rotated geometries. During the rotation of oblates, their cross-sectional area and thus, the maximum dimension remains the same, while it changes for prolates. If a mean diameter is assumed for each collection of spheroids, then $D_{\mathrm{mean}} = D_{\mathrm{max}}$ for oblates but $D_{\mathrm{mean}} < D_{\mathrm{max}}$ for prolates. On average, Mie effects are therefore stronger for ice oblates leading to lower simulated Z_e compared to ice prolates. The larger mean diameter for oblates leads to larger simulated DWR than for prolates, but also to larger ZDR values as the mean cross-section of oblates appears to be more aspherical than that of prolates.

Since a difference in DWR is found between the oblate and prolate assumption, a different retrieved size is expected for each shape assumption. In Fig. 4.16b, size retrieval results, i.e., D_{m}, using both assumptions are shown. For the prolate assumption, particles need to be larger to match the measured DWR compared to the oblate assumption. As a consequence of the larger retrieved size, IWC for the same assumption is retrieved to be lower to match the measured Z_e in comparison to oblate ice spheroids, following the *higher IWC-smaller size/lower IWC-larger size* statement. This can be seen in Fig. 4.16c where the oblates IWC is retrieved higher than horizontally aligned prolates IWC. The aforementioned statement is also confirmed from the statistical results of the whole dataset in Table 4.2. The median retrieved D_{m} for oblates was found smaller for oblates than that for horizontally aligned prolates, while the opposite is valid for the median retrieved IWC.

As simulated ZDR is larger for oblate than prolate assumption for the same sphericity S, a difference in the retrieved shape is also expected. Comparing an oblate and a prolate with the same D_{max} at Fig. 5.5, it can be seen that the D_{mean} for oblates is more aspherical than that of a prolate for ice spheroids of the same sphericity. Therefore, the presented prolate ice spheroid needs to be more aspherical than the oblate to have the same average sphericity and in turn, to produce the same ZDR. This means that for a given ZDR value, a prolate needs to be more aspherical than an oblate ice spheroid. In contrast, Fig. 4.16a suggests that the ice hydrometeors are retrieved more aspherical when the oblate assumption is used. This inconsistency maybe originates from the fact that the shape retrieval is not independent from the size retrieval and the lower retrieved D_{m} for oblates influences the retrieval of AR/S. Moreover, ZDR is known to have a strong sensitivity to particle shape but it has also some sensitivity to the effective density as well, e.g., denser ice particles have larger ZDR than less dense ice particles of the same sphericity. The mass-size relation framework used in this thesis does not consider the different oblate and prolate assumption and thus, a rice-like particle and a lentil-like particle with same D_{max} appear to have the same mass. However, they don't have the same effective density as the volumes of a prolate and an oblate spheroid differ resulting to higher effective density for prolate than oblate ice spheroids with the same maximum dimension.

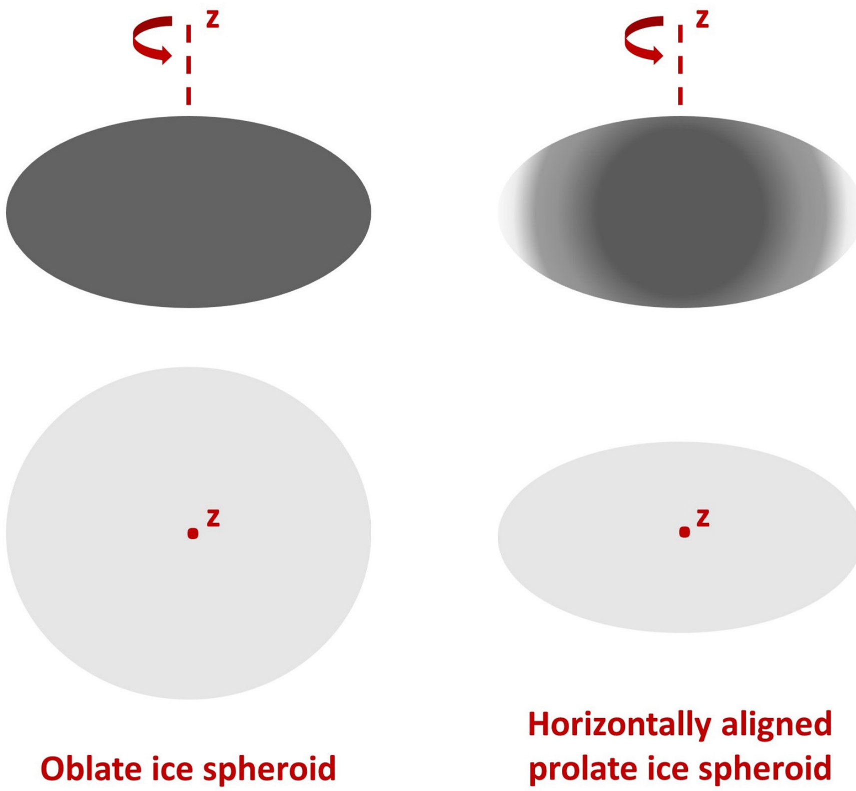

Figure 5.5: Side (dark grey shapes at the top) and bottom (light grey shapes at the bottom) perspective of an oblate and a horizontally aligned prolate ice spheroid. As *z* axis is defined to be the vertical, rotational axis during PyTMatrix averaging, the grey scale on the side face sketches (top) shows the distribution of the cross-sectional area of the ice spheroid exposed to the incident beam for all possible particle geometries.

5.2 How can ZDR constrain the retrieved particles size?

To investigate the hypothesis that ZDR is useful to constrain the shape, i.e., aspect ratio, in ice retrievals exploiting the slant-wise perspective, the performance of the retrieval was studied for different radar geometries using 2D density histograms of measured DWR and retrieved D_{m} for the oblate assumption, aggregates mass-size relation, exponential PSD and all 59 RHI scans. The histograms are presented in Fig. 5.6 for elevation angles $\theta_{\mathrm{C}} = \theta_{\mathrm{Ka}} = 30°$ (Fig. 5.6a) and $\theta_{\mathrm{C}} = 10°$, $\theta_{\mathrm{Ka}} = 90°$ (Fig 5.6b). The first observation geometry (Fig. 5.6a) is a region located between both radar instruments, while the second one (Fig. 5.6b) located directly above the Ka-band radar site. Along with the density histograms, DWR-D_{m} simulations for different values of AR are plotted with grey lines. In Fig. 5.6a, the simulations as well as the retrieved D_{m} are more closely distributed than in Fig. 5.6b. The close distribution of the DWR-D_{m} lines in Fig. 5.6a suggests that the shape constraint is not important for the size retrieval in the region between both radar systems since the simulated DWR-D_{m} do not change much with AR. In the region above the Ka-band cloud radar (Fig. 5.6b), however, polarimetric measurements from the C-band weather radar POLDIRAD, i.e., ZDR, help to narrow down the solution space of the size retrieval by providing information about the ice particle shape. This behavior is fully explained in Fig. 5.7 where the radar beams passing through ice oblate spheroids for the two different radar setups are drawn. In Fig. 5.7a, the radar beams from the two instruments penetrate oblate spheroids with different AR with the same elevation angle $\theta_C = \theta_{Ka} = 30°$. From the radar viewing geometry, this is supposed to happen in cloud regions located approximately between both radar instruments. In Fig. 5.7b, the elevation angle for the C-band radar is $\theta_C = 10°$, while the Ka-band radar points to zenith with $\theta_{Ka} = 90°$. In both cases, the radar beams penetrate two different shaped ice oblates that are aligned with their maximum dimension in the horizontal plane and which are chosen to have the same $D_{\max}$. In Fig. 5.7a, the length of the Ka-band beam does not change dramatically inside the oblate ice particles as AR increases. In Fig. 5.7b, however, the MIRA-35 beam length through the oblate ice particle, and hence the DWR, is very sensitive on the aspect ratio. Therefore, the DWR-D_m relationship becomes quite sensitive to AR in this area, especially when particles are assumed to be horizontally oriented. From similar geometric considerations, the region between both radars at very low elevation angles is another region in which the size retrieval benefits from the AR constraint. In the case of variable ice crystal shapes, ZDR from POLDIRAD is, thus, very helpful for the D_m estimation. Overall, the use of ZDR is found to be more important for the shape constraint in some radar geometries than in other, but in these areas it is considered to be crucial not only to constrain the shape but also to reduce ambiguities in size and mass of the detected ice hydrometeors.

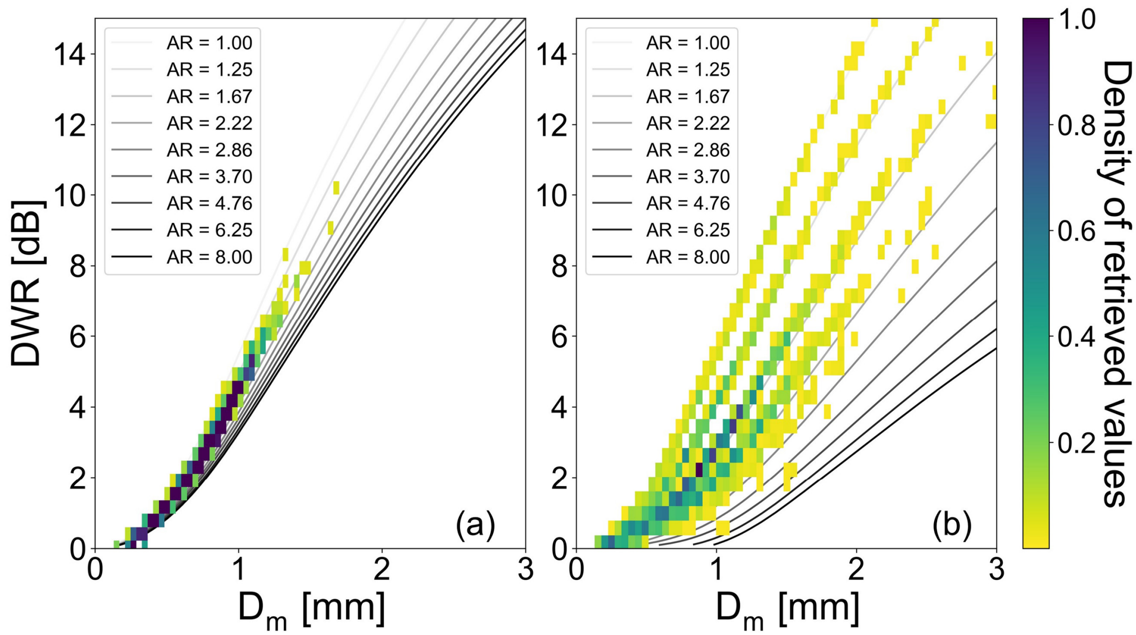

Figure 5.6: 2D density histograms between retrieved D_m and measured DWR for different observation geometries. (a) Between both radars with $\theta_C = \theta_{Ka} = 30°$ and (b) above the Ka-band radar $\theta_C = 10°$, $\theta_{Ka} = 90°$. With grey lines the DWR and D_m simulations are plotted for different values of AR using oblate ice spheroids with m(D_{max}) of aggregates.

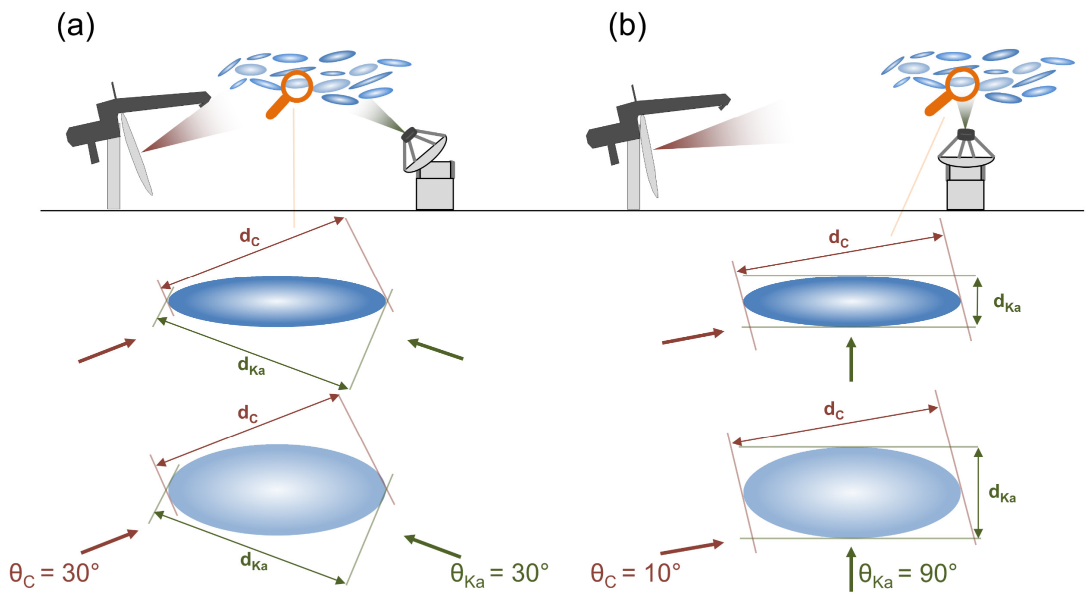

Figure 5.7: Radar beam geometries through oblate ice spheroids with different AR values for (a) $\theta_C = \theta_{Ka} = 30°$ and (b) $\theta_C = 10°$, $\theta_{Ka} = 90°$.

5.3 Evaluation of ice retrieval results and comparisons to other methods

Although sensitivity studies can be helpful to understand and interpret the performance of a retrieval, an external validation is needed to evaluate its results. A common method of external validation is to compare the output of developed retrievals with already established ones from satellites. One well-known retrieval for cloud properties is the Moderate Resolution Imaging Spectroradiometer (MODIS) retrieval. MODIS is a spectroradiometer on-board the Terra and the Aqua satellites. The Terra and Aqua MODIS provide data for the atmosphere, the land, the cryosphere and the ocean in 36 different spectral bands (0.4–14.4 µm) aiming to improve the representation of the atmospheric dynamics and processes in the Earth models (source: https://modis.gsfc.nasa.gov/). In particular, MODIS provide atmospheric measurements about clouds, water vapor or aerosols (source: https://ladsweb.modaps.eosdis.nasa.gov/). To only rough evaluate the ice microphysics results of the present study, the retrieved IWC was used to calculate the ice water path (IWP). Then, the results were compared to IWP data from the MODIS MOD06_L2 product (Platnick et al., 2015) of the Terra MODIS. The results of the comparison between the MODIS IWP and the IWP calculated from the retrieved IWC for the different $m(D_{max})$ assumptions can be found in Table 5.1. Figure 5.8 and 5.9 show the MODIS IWP for the two presented case studies from 10 and 30 January 2019.

For the case study from 10 January 2019, an average value of IWP ~ 500 g m^{-2} was estimated by eye for the whole radar cross-section from MODIS according to Fig. 5.8 (downloaded from the NASA Worldview imagery: https://worldview.earthdata.nasa.gov/ and modified to show additional information about the radar sites), when the Terra satellite passed at a horizontal distance of 560 km from Munich around 10:50 UTC. Figure 5.8 shows the two radar locations, which are areas where lower IWP values are found. However, the rest radar cross-section appears to have larger IWP values compared to Munich and Oberpfaffenhofen sites and thus, an averaged IWP value was used from MODIS, i.e., IWP ~ 500 g m^{-2} for a rough comparison of the retrieved IWP of this study. Using the mass-size relations assumed in the framework of the sensitivity studies, the best agreement between MODIS IWP and the retrieved IWP from this work was found using a modified version of aggregates, i.e., 0.5x ρ_{eff} aggregates $\mathrm{m}(\mathrm{D}_{\mathrm{max}})$. Using this assumption, it was found that the retrieved IWP was 346 g m^{-2} which is the closest value to the MODIS IWP against the other $\mathrm{m}(\mathrm{D}_{\mathrm{max}})$ assumptions (Table 5.1).

After revisiting Fig. 4.12b or 5.1 for the case study from 10 January 2019, it is clear that, some mass-size relation assumptions, used to simulate ZDR-DWR values, cannot explain a large part of the radar measurements compared to others. For instance, the 3x ρ_{eff} BF95 $\mathrm{m}(\mathrm{D}_{\mathrm{max}})$ was found to simulate very low ZDR failing to represent the measured ZDR, while the simulations using some of the rest of the $\mathrm{m}(\mathrm{D}_{\mathrm{max}})$ assumptions seem to simulate polarimetric signals that better match the ZDR measurements. Although mass-size relation assumptions that involve denser particles, i.e., the BF95 + aggregates, the 3x ρ_{eff} BF95 + aggregates, the 3x ρ_{eff} BF95 + 0.5x ρ_{eff} aggregates or the 0.5x ρ_{eff} aggregates are able to better explain the ZDR-DWR space of the radar measurements, the 0.5x ρ_{eff} aggregates assumption was found to be the best selection for this case study as it can not only produce ZDR simulations that match the measured values, but also the retrieved IWP using this assumption is quite close to the estimated average IWP from MODIS (Table 5.1).

For the case study from 30 January 2019, an averaged value of IWP ~ 170 g m^{-2} was estimated by eye for the whole radar cross-section from MODIS according to Fig. 5.9 (downloaded from NASA Worldview imagery: https://worldview.earthdata.nasa.gov/ and modified to show additional information about the radar sites), when the Terra satellite passed over Munich at a horizontal distance of 110 km around 10:30 UTC. Using the retrieved IWC for the present study and integrating with height, the closest IWP was obtained ~ 137 g m^{-2} assuming the 0.5x ρ_{eff} aggregates $\mathrm{m}(\mathrm{D}_{\mathrm{max}})$. However, after revisiting Fig. 5.2 this mass-size relation assumption is not representative for a large part of the radar measurements, highlighting once again the need for using more radar variables or in situ observations to better constrain the density of the detected ice hydrometeors.

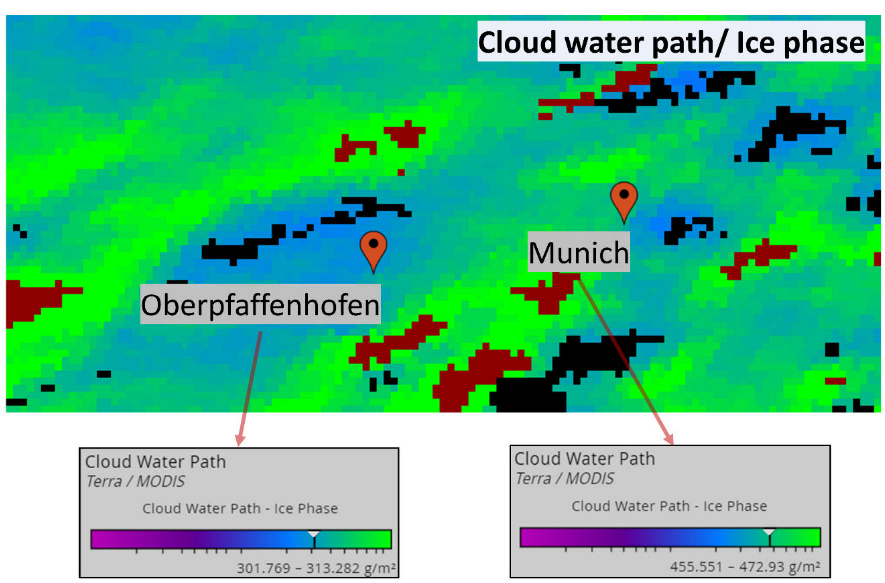

Figure 5.8: Ice water path data from MODIS MOD06_L2 product (Platnick et al., 2015) for 10 January 2019 (NASA Worldview). The image was downloaded from the NASA Worldview imagery application (https://worldview.earthdata.nasa.gov), part of the NASA Earth Observing System Data and Information System (EOSDIS), and modified to show additional information about the radar sites.

Table 5.1: Ice water path data from MODIS MOD06_L2 product (Platnick et al., 2015) and comparisons with the retrieved IWP for 10 and 30 January 2019. With bold, the closest retrieved IWP to the IWP from MODIS is marked.

Case study	MODIS MOD06_L2 IWP [g m^{-2}]	m(D_{max}) assumption	Retrieved IWP [g m^{-2}]
10 January 2019 09:48 UTC	**~500**	aggregates	234
		2x ρ_{eff} aggregates	158
		0.5x ρ_{eff} aggregates	**346**
		BF95	881
		BF95 & aggregates	240
		3x ρ_{eff} BF95	316
		3x ρ_{eff} BF95 + aggregates	203
		3x ρ_{eff} BF95 + 0.5x ρ_{eff} aggregates	260
30 January 2019 10:08 UTC	**~170**	aggregates	80
		2x ρ_{eff} aggregates	46
		0.5x ρ_{eff} aggregates	**137**
		BF95	238
		BF95 & aggregates	118
		3x ρ_{eff} BF95	98
		3x ρ_{eff} BF95 + aggregates	61
		3x ρ_{eff} BF95 + 0.5x ρ_{eff} aggregates	80

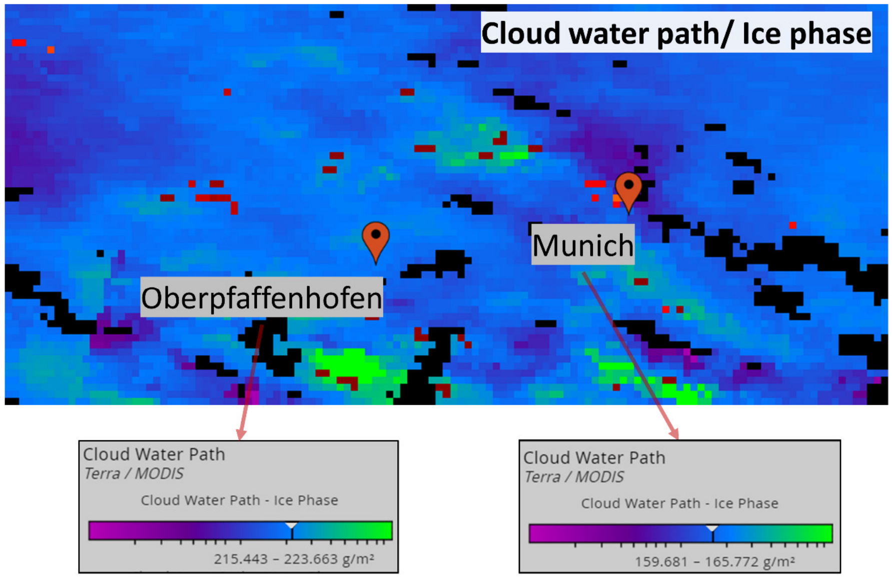

Figure 5.9: Ice water path data from MODIS MOD06_L2 product (Platnick et al., 2015) for 30 January 2019 (NASA Worldview). The image was downloaded from the NASA Worldview imagery application (https://worldview.earthdata.nasa.gov), part of the NASA Earth Observing System Data and Information System (EOSDIS), and modified to show additional information about the radar sites.

To further evaluate the retrieved IWC, the results of the present work for the case study from 30 January 2019 were compared with the IWC formula of Bukovčić et al. (2018) for dry snow ($\mathrm{IWC}\,(\mathrm{KDP}, Z_\mathrm{e}) = 0.71\mathrm{KDP}^{0.65} Z_\mathrm{e}^{0.28}$, their Eq. 28). For this comparison, the C-band radar KDP was used along with the Z_e (adjusting regarding the wavelength dependence, as the aforementioned literature suggests this formula for S band) for the presented case study (Fig. 3.3) to calculate IWC and IWP. The method of Bukovčić yields a much higher IWP (~ 2308 g m^{-2}) compared to the IWP from this study (~ 80 g m^{-2}). The IWP results of the present doctoral thesis are considered more reasonable for a moderate snowfall case since the presented method explicitly retrieves the particles size along with the IWC.

5.4 Can the ice retrieval contribute to other studies?

An interesting scientific question that arises from the present doctoral study is whether the findings of this work can be used in other studies. In this work it was found that the novel radar setup can be efficiently exploited to obtain microphysical information about ice hydrometeors. Therefore, radars from different locations can be used synergistically to monitor precipitation in their cross-sectional area. This finding can be very promising in areas with a large radar network. For instance, the nationwide C-band weather radar composite operated by the Deutscher Wetterdienst (DWD) in Germany could be used in synergy with different cloud radar sites providing information about the ice microphysics.

The developed ice retrieval can provide AR, D_m and IWC information about the ice hydrometeors detected in the radar cross-section when the right assumptions are used. Although some assumptions about the ice hydrometeors were found to be incapable to explain the radar measurements dataset compared to others, additional radar measurements could better constrain microphysical properties used in the ice retrieval. For instance, vertical radar measurements of Doppler velocity could provide density information about the detected ice particles or vertical radar measurements of LDR could constrain the oblate/prolate assumption. As future studies following this approach will consider a new measurement strategy with additional radar variables, the ice retrieval will be extended to include this information as well and hence, it will provide improved microphysical retrievals for the detected ice hydrometeors. The present doctoral study was conducted in parallel with a doctoral study from Gregor Köcher at Meteorological Institute Munich (MIM), University of Munich (LMU) in the framework of the IcePolCKa project. In that work, convective cloud microphysics in numerical weather prediction models were evaluated by developing a setup to systematically characterize the differences between model output and radar observations, i.e., dual-wavelength and polarimetric variables. Following literature recommendations to advance the microphysical representation in models by using new developments of ground-based instruments (e.g., Morrison et al., 2020), innovative measurements with already existed equipment, would improve the output of the ice retrieval developed the present study. This output could then be used to constrain microphysics in model simulations aiming to better understand and therefore, better represent the different ice processes in numerical weather prediction (NWP) models, e.g., aggregation or riming, which are significant for the evolution of precipitation.

In other studies, retrievals of ice microphysical properties can supply climatological information about the studied area. Investigating the properties of ice particles before and during different precipitation events, not only the role of ice for the evolution of precipitation but also possible trends of the microphysical properties are studied. Moreover, statistics of the retrieval results within the radars cross-section could make a significant contribution to studies investigating differences between urban (closer to MIRA-35) and suburban (closer to POLDIRAD) ice cloud characteristics, revealing possible influence by the atmospheric aerosol concentrations. Such studies could potentially give an overview on how these kind of aerosol-cloud interactions can affect the type or amount of precipitation in these two areas.

The current version of the ice microphysics retrieval scheme considers only dry ice particles. In future studies, this methodology should be extended to include wet particles as well. In this way, a better understanding of microphysical processes of ice growth, such as aggregation or riming, leading to a better representation of these processes in future weather and climate models will be achieved.

Chapter 6

6 Summary and Conclusions

This section contains work, which has already been published by Tetoni et al. (2022) in Atmospheric Measurement Techniques (AMT), entitled *"Retrievals of ice microphysical properties using dual-wavelength polarimetric radar observations during stratiform precipitation events"*.

Research Question 1: *How can the dual-wavelength method be combined with polarimetry to obtain information about the size and shape of ice hydrometeors?*

Using multi-wavelength radar methods is the state-of-the-art when it comes to the constraint of ice cloud microphysics, e.g., retrievals of ice particle size. Multi-wavelength radar methods which exploit the synergy of vertically pointing radars located at the same place cannot provide adequate shape information, i.e., aspect ratio, for the detected ice particles from polarimetric observations. In this kind of ice retrievals an assumption of the aspect ratio of ice particles is necessary.

To overcome this limitation, the possibility to use two spatially separated radars to study ice microphysics over Munich area was investigated in the present doctoral thesis. The C-band weather radar POLDIRAD and the Ka-band cloud radar MIRA-35, located at 23 km distance, provided measurements during snowfall events. The C-band weather radar is an instrument, similar to the operational DWD C-band weather radars, which is used for research purposes and thus, allows for specific scan strategies depending on the research interest. The radar reflectivities from POLDIRAD and MIRA-35 were combined to obtain dual-wavelength ratio – a parameter which is sensitive to the size of the detected ice hydrometeors. Using slant-wise radar observations it was possible to use polarimetric radar observations such as differential radar reflectivity, as well as radar reflectivity from POLDIRAD weather radar to constrain the shape – avoiding using an aspect ratio assumption – and the mass of the ice particles.

Three radar variables were extensively used in this study. Produced by two instruments with different spatial resolution, radar reflectivity, differential radar reflectivity and dual-wavelength ratio were interpolated onto a common radar grid (50 m x 50 m) using the nearest neighbor interpolation method. Different aspects that should be considered in this study were investigated. The radar calibration errors as well as random measurement errors were taken into account. Moreover, combining two spatially separated radars can produce spatiotemporal and volumetric mismatch errors in DWR measurements and thus, the effect of such errors on the present analysis was investigated too. The non-uniform beam filling errors produced by the different beam widths, i.e., 1° for POLDIRAD and 0.6° for MIRA-35, were calculated in the different areas of the radar cross-section. Additionally, the attenuation of each radar beam by atmospheric gases and hydrometeors was calculated. Since the hydrometeors attenuation using two radars at different locations is quite challenging to be estimated, a method to calculate this component within the ice retrieval algorithm was developed. Targeting only on ice microphysics retrievals, an ice mask was also implemented using polarimetric data from the two radars.

All in all, the combination of two radars measuring from different locations is not an easy task and different error sources have to be considered. However, with all the aforementioned challenges which are now known, this radar setup provides valuable microphysical information by combining dual-wavelength and polarimetric measurements without assuming an aspect ratio for the ice microphysics retrievals, e.g., size and mass, as other radar multi-wavelength methods do. Following this approach, weather radars from the DWD radar network could potentially be used in synergy with cloud radars in Germany to provide more ice microphysics information contributing to a better numerical weather prediction.

Research Question 2: *How well can a simple ice particle model explain the dual-wavelength and polarimetric radar observations? Can this model be used for ice retrievals, i.e., size, shape, mass, making some assumptions about the microphysics of the ice particles?*

In this part of the study, the combination of the radar measurements with scattering simulations for simple ice crystals to retrieve ice microphysical information was investigated. Engaging the radar measurements of dual-wavelength ratio, radar reflectivity and differential radar reflectivity with ice scattering simulations, an ice microphysics retrieval which retrieves mass, size and shape of the detected ice particles, was developed. In this retrieval, the ice particles were selected to be represented by soft spheroids. The scattering properties for a variety of ice spheroids were calculated, using the PyTMatrix algorithm and varying the AR/S, D_m and IWC of these spheroids. Scattering simulations for all possible viewing geometries between the cross-section of the radar instruments were compiled in LUTs and compared to radar observations for the implementation of the ice microphysics retrieval scheme. The ice retrieval needs to make some assumptions to determine AR/S, D_m and IWC, namely about the shape (oblate or prolate), the horizontal flutter, the PSD and the mass-size relation of the ice spheroids. Next to AR/S, D_m and IWC, the specific attenuation A was also retrieved and then, the attenuation by ice hydrometeors was estimated and used to correct the radar observations. Besides attenuation, the uncertainty of the radar calibration has been considered. In addition, the impact of the spatiotemporal mismatch between RHI scans and the volumetric mismatch between the radar beams on the measured DWR were analyzed. All aforementioned were then propagated through the retrieval to obtain an error estimation of the retrieved parameters.

Using ZDR along with DWR as well as scattering simulations for ice soft spheroids, the ambiguity in size retrievals caused by the variable aspect ratio of the ice particles could be reduced. While some influence of AR on D_m retrievals was found, in the region between both radar instruments and at high elevation angles (e.g., 30°), ZDR from POLDIRAD was very helpful to improve D_m retrievals above the Ka-band cloud radar, or in the areas between both systems where the elevation angles of both radars are low. In these regions, ZDR measurements are found to be essential not only to constrain the shape but also to reduce the uncertainty in the size retrieval from DWR measurements of horizontally aligned ice spheroids.

Overall, despite the missing internal structure of realistic ice habits which is not realistically represented by the soft spheroids, this model still remains an advantageous tool to represent ice particles as it allows for easy and fast calculations, especially during sensitivity studies as conducted in the last part of the present doctoral thesis. Due to the independent parameters describing a soft spheroid, the dependence between each degree of freedom, i.e., size, shape, mass, could be understood and studied in depth. Although it's simplicity, using the soft spheroid model the development of a simple ice microphysics retrieval constraining the AR/S, D_{m} and IWC of the detected ice hydrometeors was possible, when suitable assumptions about ice microphysics were used.

Research Question 3: *How are the ice retrievals affected by the assumptions about the (unknown) microphysics?*

Three snow events from January 2019 were used to test the ice microphysics retrieval. The retrieved parameters for shape, size and mass could reasonably explain the radar measurements of ZDR, DWR and Z_e when the detected ice particles were assumed to be represented by oblate soft spheroids (smaller RMSE errors than for horizontally aligned prolates) that follow an exponential PSD and the $\mathrm{m(D_{max})}$ of aggregates from Yang et al. (2000). An assumption if oblates or prolates are prevalent has still to be made in the current version of the ice microphysics retrieval as it was seen that this assumption can affect the retrieval results. In future studies auxiliary polarimetric data, i.e., vertical LDR measurements from the cloud radar, could provide information to this respect and reveal if the falling hydrometeors look like e.g., horizontally aligned columns (prolate ice particles) or plates (oblate ice particles).

In the present study it was found that the well-known BF95 mass-size relation assumption could not represent the radar dataset for large particles as the density of large ice spheroids using BF95 is very low. Furthermore, the soft spheroid model represents more realistic habits with reduced-density particles due to the homogeneity in the mass distribution all over the spheroid volume. The reduced-density ice spheroids produce lower simulated ZDR values and, in combination with already low-density mass-size relations like BF95, this influence on ZDR becomes even more pronounced. Therefore, BF95 combined with the soft spheroid model cannot produce polarimetric signals matching the ZDR measurements. Although the assumption of aggregates $\mathrm{m(D_{max})}$ for ice spheroids could better explain the ZDR-DWR observations, it suggests an almost constant density with increasing particle size, i.e., small ice crystals (columns or plates) appear to have the same density as larger ice particles (aggregates). Therefore, a $\mathrm{m(D_{max})}$ relation which describes a more realistic function between density and size is needed.

More investigations on the mass-size relation indicated that such assumption it is not easily constrained for ice cloud particles when in situ observations or additional radar measurements are missing. Attempting to find a most suitable mass-size relation that best explains the radar measurements, the original aggregates and BF95 $\mathrm{m(D_{max})}$ were combined in different ways, or even modified. Investigating two case studies using different mass-size relation assumptions and comparing the retrieved IWP to the IWP from Terra MODIS, it was found that the assumption of 0.5x ρ_{eff} aggregates $\mathrm{m(D_{max})}$ can best represent the radar observations and also using this assumption the retrieved IWP was the closest to the IWP from MODIS compared to all mass-size relation assumptions. Additional measurements, e.g., Doppler velocity of ice hydrometeors or in situ data, could be exploited in future studies to provide information about the mass or the density of the ice hydrometeors and thus, suggest a more variable $\mathrm{m(D_{max})}$

relation instead of a fixed one. Especially with the use of Doppler velocity radar observations, different ice particle populations could be detected, i.e., aggregated versus rimed ice particles. Since the Doppler velocity is connected to the density of the ice particles, a suitable mass-size relation can be selected. Then, additional new scattering simulations for all the different ice particle types could be included in the ice retrieval. In this way, microphysical information about dry or wet aggregated/rimed ice particles could be provided.

After the mass-size relation, which is found to be the most significant assumption in this study, the PSD, oblate/prolate and horizontal flutter assumption for the ice particles are similarly important. First of all, differences using a gamma over an exponential PSD, which is typical for cloud ice particles, can be larger than 20% for the retrieved median mass diameter and the retrieved ice water content, but differences are found to be quite low (< 5–10%) for the shape retrieval. The horizontal flutter assumption of the ice spheroids has the biggest impact on the shape retrieval, and almost no impact on the retrieved size and mass – except for the extreme case when ice spheroids are assumed with a flutter of 60° out of the horizontal plane.

Beyond the aforementioned assumptions, the radar calibration plays an important role for retrieval results, while errors due to spatiotemporal and volumetric mismatches are considered to be even less important than the radar calibration. Non-uniform beam filling effects, however, can locally have strong impacts on DWR measurements (several dB). Future studies exploring in detail this effect for spatially separated radars and developing techniques to detect and filter out these regions are definitely needed.

In conclusion, the sensitivity analysis showed that the assumption of the $\mathrm{m}(\mathrm{D}_{\mathrm{max}})$ relation plays the leading role on the current version of the retrieval. As of secondary importance are found to be the decision for oblate or prolate ice spheroids, the horizontal flutter and the particle size distribution of the ice particles. However, additional radar measurements, i.e., LDR and Doppler velocity measurements as well as in situ data, could constrain these assumptions and lead to even more realistic ice cloud microphysics retrievals considering also wet and aggregated/rimed ice particles.

This doctoral thesis presented a feasibility study to combine slant-wise polarimetric radar observations and dual-wavelength from two spatially-separated radar systems to retrieve ice cloud microphysics. The major findings of this work are summarized below:

1. The combination of two radar instruments located at different places to obtain dual wavelength and polarimetric observations is possible. For this combination different aspects need to be considered e.g., possible measured volume mismatches, as they can affect radar observations and thus, the results of the ice retrievals, and are all presented here.

2. Microphysical properties of ice hydrometeors can be retrieved by developing a retrieval scheme which uses a simple particle model, i.e., soft spheroid, and suitable assumptions about the microphysics of the ice particles.

3. The soft spheroid model used to represent the ice hydrometeors in the scattering simulations can well explain the radar observations for some mass-size relation assumptions, while it is found not to successfully produce polarimetric simulations that match the polarimetric radar observations when it is used along with mass-size relations that consider less dense ice particles. The soft spheroid model considers homogeneity in the mass distribution all over the spheroid volume and thus, reduced-density particles are used to represent realistic habits with the same maximum dimension. Therefore, they produce lower simulated ZDR values compared to more realistic habits. This effect in combination with mass-size relations which consider particles with low effective density leads to even lower simulated ZDR failing to realistically represent the measured ZDR.

4. The presented approach seems to work when the right assumptions about ice microphysics are made. Among all assumptions, the constraint of the mass-size relation used for the ice hydrometeors is found to be the most important as it can strongly affect the results of the ice retrieval.

5. Although the presented approach is developed using assumptions about the density, shape (oblate/prolate), horizontal flutter or PSD of the detected ice hydrometeors, additional radar measurements and in situ data could help to constrain these assumptions. For future studies following this approach, a new measurement strategy with additional radar variables is planned. Using this strategy, vertical measurements of Doppler velocity and LDR from the MIRA-35 cloud radar will help to better constrain the effective density of ice particles or the oblate/prolate assumption.

6. This approach included coordinated RHI scans from the two radars resulting to a single radar cross-section. As the average wind direction in the Munich area is almost aligned to this radar cross-section, the evolution of precipitation and the development of fall streaks inside the clouds could be monitored. Microphysics retrievals during ice growth processes could be very helpful as they can contribute to the constraint of such processes during the parameterizations of ice particles in numerical weather prediction, e.g., for the ice particles growth speed.

7. Using an extended version of the methodology presented in this doctoral thesis, the ice microphysical information could be better constrained. As the used radar setup seems to work, this method could potentially be applied from DWD operational weather radars and cloud radars located throughout Germany to improve the understanding on ice cloud microphysics and thus, also improve the parameterizations used in numerical weather and climate models.

Appendices

Appendix A: Estimation of minimum retrievable D_m

For sensitivity purposes regarding DWR measurements a minimum D_m had to be considered in the scattering simulations. For this reason, a minimum value of DWR = 0.1 dB that can be observed by the two radars was assumed. The minimum retrievable D_m depends not only on the viewing geometry of the two radars but also on the AR and the $m(D_{max})$ used for the calculation of the ice spheroids density. In Fig. A1 examples of the minimum retrievable D_m for different radar geometries and $m(D_{max})$ are presented. For this figure, the $m(D_{max})$ of aggregates is used for red and dark red line plots for the mass estimation of the ice spheroids. The "horiz-horiz" label is used when the two radar beams are emitted horizontally, while the "horiz-vert" label is used when the C-band beam is emitted horizontally and the Ka-band beam towards the zenith.

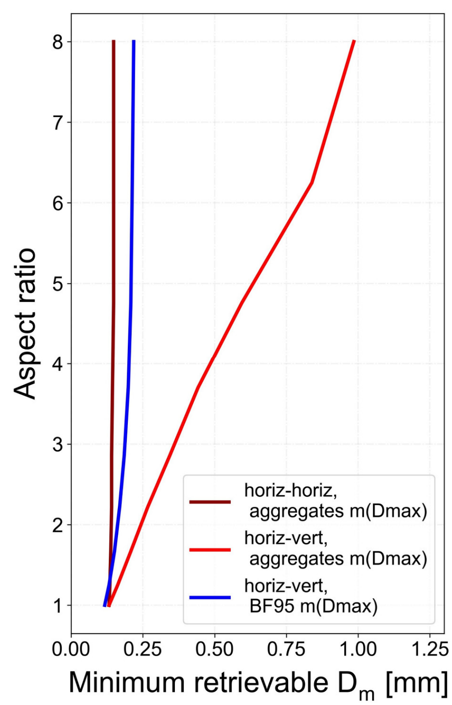

Figure A1: Minimum possible retrieved D_m using ice spheroids with $m(D_{max})$ analog to aggregates when C-band and Ka-band beam are emitted horizontally (dark red). With red and blue color, the minimum possible retrieved D_m for ice spheroids with $m(D_{max})$ analog to aggregates and BF95 when C-band beam is emitted horizontally and Ka-band beam is emitted towards zenith is plotted.

As all ice spheroids are assumed to be aligned to the horizontal plane with small flutter of up to 20° out of this plane, the minimum retrievable D_m is, in general, smaller when the radar beams are passing through the ice spheroids from the side. Assuming C-band beam emitted horizontally and for ice particles with the same size, Mie effects can be stronger for Ka-band beam when it penetrates the particles from the side (horiz-horiz geometry) rather than from below (horiz-vert geometry), as the beam path is longer inside the particle. For horiz-horiz geometry, $Z_{e_{Ka}}$ values are lower and thus, DWR is larger than for horiz-vert geometry for same particle size. Therefore, the lowest minimum retrievable D_{m} is smaller in horiz-horiz than in horiz-vert geometry. From the comparison of red (ice spheroids that follow $\mathrm{m(D_{max})}$ of aggregates) and blue (ice spheroids that follow $\mathrm{m(D_{max})}$ of BF95) color line plots, in which the radar beams are simulated to be emitted horizontally (C band) and vertically (Ka band), the minimum retrievable D_{m} using ice spheroids with $\mathrm{m(D_{max})}$ analog to this of aggregates is larger compared to this of BF95, due to the higher effective density of aggregates assumption for ice spheroids of the same size. The less dense the particles are, the smaller the D_{m} will be for the minimum DWR threshold of 0.1 dB. For the "horiz-vert" geometry, more aspherical particles have a larger minimum retrievable D_{m} due to their weaker DWR signature as a result of their shorter cross-section along the Ka-band beam. Vice versa for the "horiz-horiz" geometry, more aspherical particles have a smaller minimum retrievable D_{m} due to their stronger DWR signature as a result to their longer cross-section along the Ka-beam.

Appendix B: Estimation of total hydrometeors attenuation

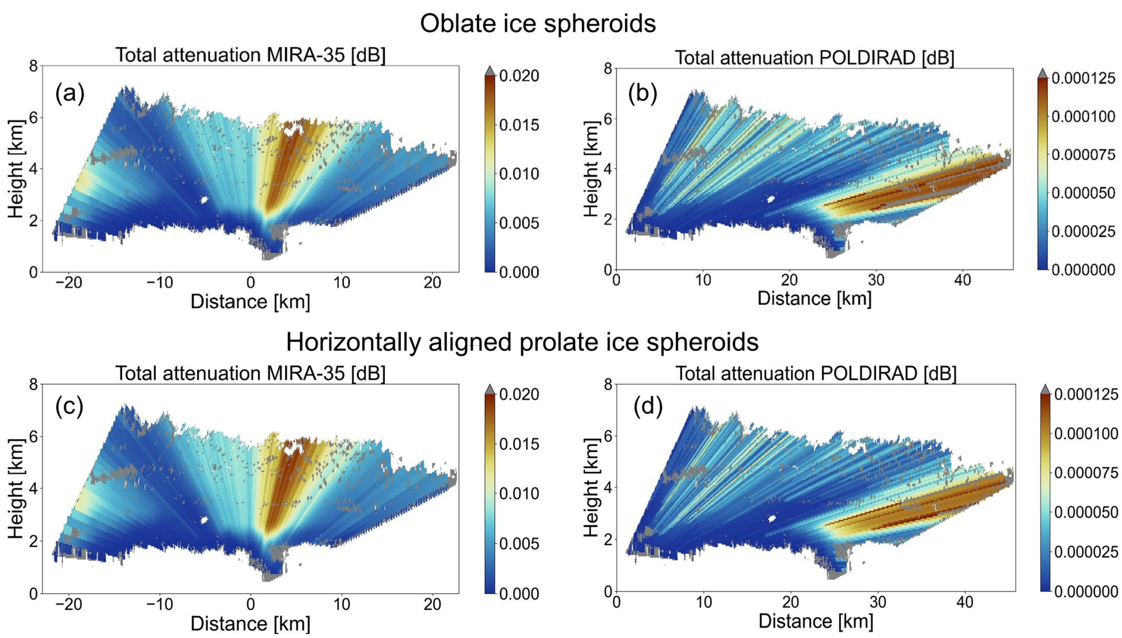

Figure B1: Total attenuation estimation for Ka and C band for 30 January 2019 at 10:08 UTC when (a, b) ice oblates and (c, d) horizontally aligned ice prolates and aggregates $\mathrm{m(D_{max})}$ (Yang et al., 2000) are used for the scattering simulations performed by using PyTMatrix (Leinonen, 2014). Areas with filtered radar measurements are marked using grey color.

Data and datasets availability

The Hersbach et al. (2018) data were downloaded from the Copernicus Climate Change Service (C3S) Climate Data Store (CDS): https://doi.org/10.24381/cds.bd0915c6. The authors did not download the data to distribute them. The results contain modified Copernicus Climate Change Service information 2020. The IWP data used in this work were the MODIS MOD06_L2 product (identifier doi: http://dx.doi.org/10.5067/MODIS/MOD06_L2.061; Platnick et al., 2015). The images with the MODIS IWP data were obtained from the NASA Worldview imagery application (https://worldview.earthdata.nasa.gov), part of the NASA Earth Observing System Data and Information System (EOSDIS). The wind speed and temperature data were provided by the University of Wyoming (https://weather.uwyo.edu/upperair/sounding.html, University of Wyoming, source: Deutscher Wetterdienst). The radar data collected from the weather radar POLDIRAD and the cloud radar MIRA-35 can be available upon request. Finally, the creation of some figures in the present doctoral thesis is implemented using the "Scientific colour maps 7.0" package (identifier doi: https://doi.org/10.5281/zenodo.5501399), as described in, e.g., Crameri et al., 2020) and the ARM Radar Toolkit (Py-ART; Helmus and Collis, 2016, identifier doi: https://doi.org/10.5334/jors.119). The ARM scattering database data are available for downloading with identifier doi: https://doi.org/10.5439/1258029 (Aydin et al., 2016).

List of figures

List of tables

List of abbreviations

Abbreviation	Long name
AMT	Atmospheric Measurement Techniques
ARM	Atmospheric Radiation Measurement
BAECC	Biogenic Aerosols-Effects on Clouds and Climate
BF95	Brown and Francis 1995
C3S	Copernicus Climate Change Service
CDS	Climate Data Store
DDA	Discrete-Dipole Approximation
DFG	Deutsche Forschungsgemeinschaft (German Research Foundation)
DLR	Deutsches Zentrum für Luft- und Raumfahrt (German Aerospace Center)
DWD	Deutscher Wetterdienst
ECMWF	European Centre for Medium-Range Weather Forecasts
EMA	Effective Medium Approximation
GMM	Generalized Multiparticle Mie method
IcePolCKa	Investigation of the initiation of convection and the evolution of Precipitation using simulatiOns and poLarimetric radar observations at C- and Ka-band
IPA	Institute of Atmospheric Physics
ITU	International Telecommunication Union
IWC	Ice Water Content
IWP	Ice Water Path
LMU	Ludwig Maximilians University of Munich
LUTs	Look-Up Tables
MACS	Munich Aerosol Cloud Scanner
MG	Maxwell-Garnett
MIM	Meteorological Institute Munich
ML	Melting Layer
MODIS	Moderate resolution imaging spectroradiometer
MOR-G	Morrison scheme with rimed particles assumed graupel
MOR-H	Morrison scheme with rimed particles assumed hail
MSL	Mean Sea Level
NWP	Numerical Weather Prediction
OLYMPEX	Olympic Mountains Experiment
P3	Predicted Particle Properties
PPI	Plain-Position-Indicator scan
PROM	Polarimetric radar observations meet atmospheric modelling
PSD	Particle Size Distribution
QPE	Quantitative Precipitation Estimation

RADAR	RAdio Detection And Ranging
RHI	Range-Height-Indicator scan
RMSE	Root Mean Square Error
S-RHI	Sector Range-Height-Indicator scan
SSRGA	Self-Similar Rayleigh-Gans Approximation
STAR	Simultaneous Transmission And Reception
StormVEx	Storm Peak Laboratory Cloud Property Validation Experiment

List of symbols

Symbol	Parameter
$\lvert K\rvert^2$	dielectric factor
a	prefactor of the $\mathrm{m}(D_{\max})$,
A	specific attenuation
A_{eff}	effective area of the radar antenna
AR	aspect ratio
A_{target}	area of a target
a_{ZDR}	ratio of local ZDR standard deviation to local ZDR mean
b	exponent of the $\mathrm{m}(D_{\max})$
b_{n}	fitting coefficient
c	speed of light
d	diameter of a medium inclusion
D	geometrical diameter of the ice particles
D_0	median volume diameter
D_{area}	equivalent-area diameter
D_{crit}	critical size parameter of medium inclusions
D_{eq}	melted equivalent diameter
D_{m}	median mass diameter
$D_{\max}$	maximum diameter
$D_{\mathrm{max\_PSD}}$	PSD maximum diameter
D_{mean}	mean-dimension diameter
$D_{\min}$	minimum diameter/dimension
$D_{\mathrm{min\_PSD}}$	PSD minimum diameter
DWR	dual-wavelength ratio
e_{eff}	effective permittivity
e_{i}	permittivity of the inclusion
e_{m}	permittivity of the medium
f	radar frequency
g	antenna gain
I_{iso}	power density of an isotropic source
$I_{\mathrm{non\text{-}iso}}$	power density of a non-isotropic source
IWC	ice water content
IWP	ice water path
J_1	cost function for size and shape ice retrieval
J_2	cost function for mass ice retrieval
k	imaginary part of refractive index
KDP	specific differential phase

LD-P1d	low-density P1d ice aggregates from ARM scattering database
LDR	linear depolarization ratio
m	mass of the ice particle
$m(D_{max})$	mass-size relation
m_{RI}	complex refractive index
n	real part of refractive index
N	number concentration of ice particles
N_w	PSD intercept parameter
P_r	received power
PSD	particle size distribution
P_{target}	antenna intercepted power from a target
P_τ	transmitted power
r	energy distance
R	snowfall rate
RMSE	Root Mean Square Error
r_p	particle radius
r_{target}	radius of a target
S	sphericity
S_{HH}	scattering amplitude of the horizontally polarized received signal from a horizontally polarized emitted signal
S_{VV}	scattering amplitude of the vertically polarized received signal from a vertically polarized emitted signal
T	temperature
V	measured volume
x	size parameter
z	radar reflectivity in linear scale
Z	radar reflectivity in logarithmic scale
ZDP	reflectivity difference
ZDR	differential radar reflectivity
ZDR_{mean}	local ZDR mean
ZDR_{stdv}	local ZDR standard deviation
z_e	equivalent reflectivity factor in linear scale
Z_e	equivalent reflectivity factor in logarithmic scale
Z_H	horizontal radar reflectivity in logarithmic scale
z_{HH}	linear reflectivity at the horizontal polarization channel when the radar transmits horizontally polarized signal
z_{HV}	linear reflectivity at the vertical polarization channel when the radar transmits horizontally polarized signal
Z_V	vertical radar reflectivity in logarithmic scale
α	Euler angle of the scattering orientation
β	Euler angle of the scattering orientation

η	measured radar reflectivity
θ	radar elevation angle
λ	radar wavelength
μ	PSD width parameter
π	pi
ρ_{eff}	effective density
ρ_{HV}	cross-correlation coefficient
ρ_w	water density
σ_{b_sca}	backscattering cross-section of a target
τ	radar pulse duration
φ	vertical radar beam width
φDP	differential propagation phase

Bibliography

Aristotle: Meteorologica, Book I, 340a, available at Wikisource: https://el.wikisource.org/wiki/Μετεωρολογικά/Α#p340a.

Aydin, K., Verlinde, J., Clothiaux, E. E., Lu, Y., Jiang, Z., and Botta, G.: Polarimetric scattering database for non-spherical ice particles at microwave wavelengths. Atmospheric Radiation Measurement (ARM) Climate Research Facility Data Archive: Oak Ridge, Tennessee, USA, [data set], https://doi.org/10.5439/1258029 (last access: 14 September 2022), 2016.

Bailey, M. P. and Hallett, J.: A Comprehensive Habit Diagram for Atmospheric Ice Crystals: Confirmation from the Laboratory, AIRS II, and Other Field Studies, J. Atmos. Sci., 66, 2888–2899, https://doi.org/10.1175/2009JAS2883.1, 2009.

Battan, L. J.: Radar observation of the atmosphere., Q. J. R. Meteorolog. Soc., 99, 793–793, https://doi.org/10.1002/qj.49709942229, 1973.

Brdar, S. and Seifert, A.: McSnow: A Monte-Carlo Particle Model for Riming and Aggregation of Ice Particles in a Multidimensional Microphysical Phase Space, J. Adv. Model. Earth Syst., 10, 187–206, https://doi.org/10.1002/2017MS001167, 2018.

Bringi, V. N. and Chandrasekar, V.: Polarimetric Doppler Weather Radar: Principles and Applications, Cambridge University Press, Cambridge, https://doi.org/10.1017/CBO9780511541094, 2001.

Brown, P. R. A. and Francis, P. N.: Improved Measurements of the Ice Water Content in Cirrus Using a Total-Water Probe, J. Atmos. Oceanic Technol., 12, 410–414, https://doi.org/10.1175/1520-0426(1995)012<0410:IMOTIW>2.0.CO;2, 1995.

Bukovčić, P., Ryzhkov, A., Zrnić, D., and Zhang, G.: Polarimetric Radar Relations for Quantification of Snow Based on Disdrometer Data, J. Appl. Meteorol. Clim., 57, 103–120, https://doi.org/10.1175/JAMC-D-17-0090.1, 2018.

Cazenave, Q., Ceccaldi, M., Delanoë, J., Pelon, J., Groß, S., and Heymsfield, A.: Evolution of DARDAR-CLOUD ice cloud retrievals: new parameters and impacts on the retrieved microphysical properties, Atmos. Meas. Tech., 12, 2819–2835, https://doi.org/10.5194/amt-12-2819-2019, 2019.

Connolly, P. J., Emersic, C., and Field, P. R.: A laboratory investigation into the aggregation efficiency of small ice crystals, Atmos. Chem. Phys., 12, 2055–2076, https://doi.org/10.5194/acp-12-2055-2012, 2012.

Cotton, R. J., Field, P. R., Ulanowski, Z., Kaye, P. H., Hirst, E., Greenaway, R. S., Crawford, I., Crosier, J., and Dorsey, J.: The effective density of small ice particles obtained from in situ aircraft observations of mid-latitude cirrus, Q. J. R. Meteorolog. Soc., 139, 1923–1934, https://doi.org/10.1002/qj.2058, 2013.

Crameri, F.: Scientific colour-maps, Zenodo, [data set], https://doi.org/10.5281/zenodo.5501399, 2021.

Crameri, F., Shephard, G. E., and Heron, P. J.: The misuse of colour in science communication, Nat. Commun., 11, 5444, https://doi.org/10.1038/s41467-020-19160-7, 2020.

Ding, S., McFarquhar, G. M., Nesbitt, S. W., Chase, R. J., Poellot, M. R., and Wang, H.: Dependence of Mass–Dimensional Relationships on Median Mass Diameter, Atmosphere, 11, 756, https://doi.org/10.3390/atmos11070756, 2020.

Draine, B. T. and Flatau, P. J.: Discrete-Dipole Approximation For Scattering Calculations, J. Opt. Soc. Am. A, JOSAA, 11, 1491–1499, https://doi.org/10.1364/JOSAA.11.001491, 1994.

Erfani, E. and Mitchell, D. L.: Developing and bounding ice particle mass- and area-dimension expressions for use in atmospheric models and remote sensing, Atmos. Chem. Phys., 16, 4379–4400, https://doi.org/10.5194/acp-16-4379-2016, 2016.

Erfani, E. and Mitchell, D. L.: Growth of ice particle mass and projected area during riming, Atmos. Chem. Phys., 17, 1241–1257, https://doi.org/10.5194/acp-17-1241-2017, 2017.

Ewald, F., Winkler, C., and Zinner, T.: Reconstruction of cloud geometry using a scanning cloud radar, Atmos. Meas. Tech., 8, 2491–2508, https://doi.org/10.5194/amt-8-2491-2015, 2015.

Ewald, F., Groß, S., Hagen, M., Hirsch, L., Delanoë, J., and Bauer-Pfundstein, M.: Calibration of a 35 GHz airborne cloud radar: lessons learned and intercomparisons with 94 GHz cloud radars, Atmos. Meas. Tech., 12, 1815–1839, https://doi.org/10.5194/amt-12-1815-2019, 2019.

Ferrone, A. and Berne, A.: Dynamic Differential Reflectivity Calibration Using Vertical Profiles in Rain and Snow, Remote Sens., 13, 8, https://doi.org/10.3390/rs13010008, 2021.

Field, P. R. and Heymsfield, A. J.: Aggregation and Scaling of Ice Crystal Size Distributions, J. Atmos. Sci., 60, 544–560, https://doi.org/10.1175/1520-0469(2003)060<0544:AASOIC>2.0.CO;2, 2003.

Field, P. R. and Heymsfield, A. J.: Importance of snow to global precipitation, Geophys. Res. Lett., 42, 9512–9520, https://doi.org/10.1002/2015GL065497, 2015.

Frech, M. and Hubbert, J.: Monitoring the differential reflectivity and receiver calibration of the German polarimetric weather radar network, Atmos. Meas. Tech., 13, 1051–1069, https://doi.org/10.5194/amt-13-1051-2020, 2020.

Garnett, J. C. M. and Larmor, J.: XII. Colours in metal glasses and in metallic films, Philosophical Transactions of the Royal Society of London. Series A, Containing Papers of a Mathematical or Physical Character, 203, 385–420, https://doi.org/10.1098/rsta.1904.0024, 1904.

Gorgucci, E., Scarchilli, G., and Chandrasekar, V.: A procedure to calibrate multiparameter weather radar using properties of the rain medium, IEEE Trans. Geosci. Remote Sens., 37, 269–276, https://doi.org/10.1109/36.739161, 1999.

Görsdorf, U., Lehmann, V., Bauer-Pfundstein, M., Peters, G., Vavriv, D., Vinogradov, V., and Volkov, V.: A 35-GHz Polarimetric Doppler Radar for Long-Term Observations of Cloud Parameters—Description of System and Data Processing, J. Atmos. Oceanic Technol., 32, 675–690, https://doi.org/10.1175/JTECH-D-14-00066.1, 2015.

Gunn, K. L. S. and Marshall, J. S.: THE DISTRIBUTION WITH SIZE OF AGGREGATE SNOWFLAKES, J. Atmos. Sci., 15, 452–461, https://doi.org/10.1175/1520-0469(1958)015<0452:TDWSOA>2.0.CO;2, 1958.

Harrington, J. Y., Sulia, K., and Morrison, H.: A Method for Adaptive Habit Prediction in Bulk Microphysical Models. Part I: Theoretical Development, J. Atmos. Sci., 70, 349–364, https://doi.org/10.1175/JAS-D-12-040.1, 2013.

Helmus, J. and Collis, S.: The Python ARM Radar Toolkit (Py-ART), a Library for Working with Weather Radar Data in the Python Programming Language, J. Open Res. Software, 4, e25, https://doi.org/10.5334/jors.119, 2016.

Hersbach, H., Bell, B., Berrisford, P., Biavati, G., Horányi, A., Muñoz Sabater, J., Nicolas, J., Peubey, C., Radu, R., Rozum, I., Schepers, D., Simmons, A., Soci, C., Dee, D., and Thépaut, J.- N.: ERA5 hourly data on pressure levels from 1979 to present, Copernicus Climate Change Service (C3S) Climate Data Store (CDS), [data set], https://doi.org/10.24381/cds.bd0915c6, 2018.

Heymsfield, A. J., Bansemer, A., Field, P. R., Durden, S. L., Stith, J. L., Dye, J. E., Hall, W., and Grainger, C. A.: Observations and Parameterizations of Particle Size Distributions in Deep Tropical Cirrus and Stratiform Precipitating Clouds: Results from In Situ Observations in TRMM Field Campaigns, J. Atmos. Sci., 59, 3457–3491, https://doi.org/10.1175/1520-0469(2002)059<3457:OAPOPS>2.0.CO;2, 2002.

Heymsfield, A. J., Schmitt, C., Bansemer, A., and Twohy, C. H.: Improved Representation of Ice Particle Masses Based on Observations in Natural Clouds, J. Atmos. Sci., 67, 3303–3318, https://doi.org/10.1175/2010JAS3507.1, 2010.

Heymsfield, A. J., Schmitt, C., Chen, C.-C.-J., Bansemer, A., Gettelman, A., Field, P. R., and Liu, C.: Contributions of the Liquid and Ice Phases to Global Surface Precipitation: Observations and Global Climate Modeling, J. Atmos. Sci., 77, 2629–2648, https://doi.org/10.1175/JAS-D-19-0352.1, 2020.

Hogan, R. J. and Illingworth, A. J.: The Potential of Spaceborne Dual-Wavelength Radar to Make Global Measurements of Cirrus Clouds, J. Atmos. Oceanic Technol., 16, 518–531, https://doi.org/10.1175/1520-0426(1999)016<0518:TPOSDW>2.0.CO;2, 1999.

Hogan, R. J. and Westbrook, C. D.: Equation for the Microwave Backscatter Cross Section of Aggregate Snowflakes Using the Self-Similar Rayleigh–Gans Approximation, J. Atmos. Sci., 71, 3292–3301, https://doi.org/10.1175/JAS-D-13-0347.1, 2014.

Hogan, R. J., Illingworth, A. J., and Sauvageot, H.: Measuring Crystal Size in Cirrus Using 35- and 94-GHz Radars, J. Atmos. Ocean. Technol., 17, 27–37, https://doi.org/10.1175/1520-0426(2000)017<0027:MCSICU>2.0.CO;2, 2000.

Hogan, R. J., Mittermaier, M. P., and Illingworth, A. J.: The Retrieval of Ice Water Content from Radar Reflectivity Factor and Temperature and Its Use in Evaluating a Mesoscale Model, J. Appl. Meteorol. Clim., 45, 301–317, https://doi.org/10.1175/JAM2340.1, 2006.

Hogan, R. J., Tian, L., Brown, P. R. A., Westbrook, C. D., Heymsfield, A. J., and Eastment, J. D.: Radar Scattering from Ice Aggregates Using the Horizontally Aligned Oblate Spheroid Approximation, J. Appl. Meteorol. Clim., 51, 655–671, https://doi.org/10.1175/JAMC-D-11-074.1, 2012.

Hogan, R. J., Honeyager, R., Tyynelä, J., and Kneifel, S.: Calculating the millimetre-wave scattering phase function of snowflakes using the self-similar Rayleigh–Gans Approximation, Q.J.R. Meteorol. Soc., 143, 834–844, https://doi.org/10.1002/qj.2968, 2017.

Höller, H.: Radar-Derived Mass-Concentrations of Hydrometeors for Cloud Model Retrievals., in: Proc. 27th Conference on Radar Meteorology, 27th Conference on Radar Meteorology, Vail, CO, USA, 9-13 October 95, 453–454, 1995.

Höller, H., Hagen, M., Meischner, P. F., Bringi, V. N., and Hubbert, J.: Life Cycle and Precipitation Formation in a Hybrid-Type Hailstorm Revealed by Polarimetric and Doppler Radar Measurements, J. Atmos. Sci., 51, 2500–2522, https://doi.org/10.1175/1520-0469(1994)051<2500:LCAPFI>2.0.CO;2, 1994.

Houze, R. A.: Observed structure of mesoscale convective systems and implications for large-scale heating. Q. J. R. Meteorol. Soc., 115, 425–461, https://doi.org/10.1002/qj.49711548702, 1989.

Houze, R. A.: Cloud Dynamics, Second Edition, in: International Geophysics, Vol. 104, Academic Press, ISBN: 978-0-12-374266-7, 2014.

Houze, R. A., McMurdie, L. A., Petersen, W. A., Schwaller, M. R., Baccus, W., Lundquist, J. D., Mass, C. F., Nijssen, B., Rutledge, S. A., Hudak, D. R., Tanelli, S., Mace, G. G., Poellot, M. R., Lettenmaier, D. P., Zagrodnik, J. P., Rowe, A. K., DeHart, J. C., Madaus, L. E., Barnes, H. C., and Chandrasekar, V.: The Olympic Mountains Experiment (OLYMPEX), Bull. Am. Meteorol. Soc., 98, 2167–2188, https://doi.org/10.1175/BAMS-D-16-0182.1, 2017.

Huang, G.-J., Bringi, V. N., Newman, A. J., Lee, G., Moisseev, D., and Notaroš, B. M.: Dual-wavelength radar technique development for snow rate estimation: a case study from GCPEx, Atmos. Meas. Tech., 12, 1409–1427, https://doi.org/10.5194/amt-12-1409-2019, 2019.

Huang, Y., Wu, W., McFarquhar, G. M., Xue, M., Morrison, H., Milbrandt, J., Korolev, A. V., Hu, Y., Qu, Z., Wolde, M., Nguyen, C., Schwarzenboeck, A., and Heckman, I.: Microphysical processes producing high ice water contents (HIWCs) in tropical convective clouds during the HAIC-HIWC field campaign: dominant role of secondary ice production, Atmos. Chem. Phys., 22, 2365–2384, https://doi.org/10.5194/acp-22-2365-2022, 2022.

ITU-R P.676-12: Attenuation by atmospheric gases, ITU, https://www.itu.int/rec/R-REC-P.676/en (last access: 8 April 2022), 2019.

Jiang, Z., Verlinde, J., Clothiaux, E. E., Aydin, K., and Schmitt, C.: Shapes and Fall Orientations of Ice Particle Aggregates, J. Atmos. Sci., 76, 1903–1916, https://doi.org/10.1175/JAS-D-18-0251.1, 2019.

Kalesse, H., Szyrmer, W., Kneifel, S., Kollias, P., and Luke, E.: Fingerprints of a riming event on cloud radar Doppler spectra: observations and modeling, Atmos. Chem. Phys., 16, 2997–3012, https://doi.org/10.5194/acp-16-2997-2016, 2016.

Kneifel, S., Lerber, A. von, Tiira, J., Moisseev, D., Kollias, P., and Leinonen, J.: Observed relations between snowfall microphysics and triple-frequency radar measurements, J. Geophys. Res.: Atmos., 120, 6034–6055, https://doi.org/10.1002/2015JD023156, 2015.

Kneifel, S., Kollias, P., Battaglia, A., Leinonen, J., Maahn, M., Kalesse, H., and Tridon, F.: First observations of triple-frequency radar Doppler spectra in snowfall: Interpretation and applications, Geophys. Res. Lett., 43, 2225–2233, https://doi.org/10.1002/2015GL067618, 2016.

Köcher, G., Zinner, T., Knote, C., Tetoni, E., Ewald, F., and Hagen, M.: Evaluation of convective cloud microphysics in numerical weather prediction models with dual-wavelength polarimetric radar observations: methods and examples, Atmos. Meas. Tech., 15, 1033–1054, https://doi.org/10.5194/amt-15-1033-2022, 2022.

Kumjian, M.: Principles and applications of dual-polarization weather radar. Part I: Description of the polarimetric radar variables, J. Oper. Meteorol., 1, 226–242, https://doi.org/10.15191/nwajom.2013.0119, 2013.

Lawson, R. P., Baker, B., Pilson, B., and Mo, Q.: In Situ Observations of the Microphysical Properties of Wave, Cirrus, and Anvil Clouds. Part II: Cirrus Clouds, J. Atmos. Sci., 63, 3186–3203, https://doi.org/10.1175/JAS3803.1, 2006.

Leighton, H., Black, R., Zhang, X., Marks Jr, F. D., and Gopalakrishnan, S. G.: Ice Particle Size Distributions From Composites of Microphysics Observations Collected in Tropical Cyclones, Geophys. Res. Lett., 47, e2020GL088762, https://doi.org/10.1029/2020GL088762, 2020.

Leinonen, J.: High-level interface to T-matrix scattering calculations: architecture, capabilities and limitations, Opt. Express, 22, 1655–1660, https://doi.org/10.1364/OE.22.001655, 2014.

Leinonen, J., Kneifel, S., Moisseev, D., Tyynelä, J., Tanelli, S., and Nousiainen, T.: Evidence of nonspheroidal behavior in millimeter-wavelength radar observations of snowfall, J. Geophys. Res.: Atmos., 117, https://doi.org/10.1029/2012JD017680, 2012.

Leinonen, J., Kneifel, S., and Hogan, R. J.: Evaluation of the Rayleigh–Gans approximation for microwave scattering by rimed snowflakes, Q. J. R. Meteorol. Soc., 144, 77–88, https://doi.org/10.1002/qj.3093, 2018a.

Leinonen, J., Lebsock, M. D., Tanelli, S., Sy, O. O., Dolan, B., Chase, R. J., Finlon, J. A., von Lerber, A., and Moisseev, D.: Retrieval of snowflake microphysical properties from multifrequency radar observations, Atmos. Meas. Tech., 11, 5471–5488, https://doi.org/10.5194/amt-11-5471-2018, 2018b.

Leroy, D., Fontaine, E., Schwarzenboeck, A., and Strapp, J. W.: Ice Crystal Sizes in High Ice Water Content Clouds. Part I: On the Computation of Median Mass Diameter from In Situ Measurements, J. Atmos. Ocean. Technol., 33, 2461–2476, https://doi.org/10.1175/JTECH-D-15-0151.1, 2016.

Liao, L., Meneghini, R., Tokay, A., and Bliven, L. F.: Retrieval of Snow Properties for Ku- and Ka-Band Dual-Frequency Radar, J. Appl. Meteorol. Clim., 55, 1845–1858, https://doi.org/10.1175/JAMC-D-15-0355.1, 2016.

Lin, L., Fu, Q., Liu, X., Shan, Y., Giangrande, S. E., Elsaesser, G. S., Yang, K., and Wang, D.: Improved Convective Ice Microphysics Parameterization in the NCAR CAM Model, J. Geophys. Res.: Atmos., 126, e2020JD034157, https://doi.org/10.1029/2020JD034157, 2021.

Lin, Y.-L., Farley, R. D., and Orville, H. D.: Bulk Parameterization of the Snow Field in a Cloud Model, J. Appl. Meteorol. Clim., 22, 1065–1092, https://doi.org/10.1175/1520-0450(1983)022<1065:BPOTSF>2.0.CO;2, 1983.

Liou, K.-N.: Influence of Cirrus Clouds on Weather and Climate Processes: A Global Perspective, Mon. Weather Rev., 114, 1167–1199, https://doi.org/10.1175/1520-0493(1986)114<1167:IOCCOW>2.0.CO;2, 1986.

Liou, K.-N. and Yang, P.: Light Scattering by Ice Crystals: Fundamentals and Applications, Cambridge University Press, Cambridge, https://doi.org/10.1017/CBO9781139030052, 2016.

Liu, C., Lee Panetta, R., and Yang, P.: Inhomogeneity structure and the applicability of effective medium approximations in calculating light scattering by inhomogeneous particles, J. Quant. Spectrosc. Radiat. Transfer, 146, 331–348, https://doi.org/10.1016/j.jqsrt.2014.03.018, 2014.

Lo, K. K. and Passarelli, R. E.: The Growth of Snow in Winter Storms:. An Airborne Observational Study, J. Atmos. Sci., 39, 697–706, https://doi.org/10.1175/1520-0469(1982)039<0697:TGOSIW>2.0.CO;2, 1982.

Lu, Y., Jiang, Z., Aydin, K., Verlinde, J., Clothiaux, E. E., and Botta, G.: A polarimetric scattering database for non-spherical ice particles at microwave wavelengths, Atmos. Meas. Tech., 9, 5119–5134, https://doi.org/10.5194/amt-9-5119-2016, 2016.

Lynn, B. H., Khain, A. P., Dudhia, J., Rosenfeld, D., Pokrovsky, A., and Seifert, A.: Spectral (Bin) Microphysics Coupled with a Mesoscale Model (MM5). Part I: Model Description and First Results, Mon. Weather Rev., 133, 44–58, https://doi.org/10.1175/MWR-2840.1, 2005.

Mason, S. L., Chiu, C. J., Hogan, R. J., Moisseev, D., and Kneifel, S.: Retrievals of Riming and Snow Density From Vertically Pointing Doppler Radars, J. Geophys. Res.: Atmos., 123, 13,807-13,834, https://doi.org/10.1029/2018JD028603, 2018.

Mason, S. L., Hogan, R. J., Westbrook, C. D., Kneifel, S., Moisseev, D., and von Terzi, L.: The importance of particle size distribution and internal structure for triple-frequency radar retrievals of the morphology of snow, Atmos. Meas. Tech., 12, 4993–5018, https://doi.org/10.5194/amt-12-4993-2019, 2019.

Matrosov, S. Y.: A Dual-Wavelength Radar Method to Measure Snowfall Rate, J. Appl. Meteorol. Clim., 37, 1510–1521, https://doi.org/10.1175/1520-0450(1998)037<1510:ADWRMT>2.0.CO;2, 1998.

Matrosov, S. Y.: Evaluations of the Spheroidal Particle Model for Describing Cloud Radar Depolarization Ratios of Ice Hydrometeors, J. Atmos. Ocean. Technol., 32, 865–879, https://doi.org/10.1175/JTECH-D-14-00115.1, 2015.

Matrosov, S. Y.: Ice Hydrometeor Shape Estimations Using Polarimetric Operational and Research Radar Measurements, Atmosphere, 11, 97, https://doi.org/10.3390/atmos11010097, 2020.

Matrosov, S. Y. and Heymsfield, A. J.: Empirical Relations between Size Parameters of Ice Hydrometeor Populations and Radar Reflectivity, J. Appl. Meteorol. Clim., 56, 2479–2488, https://doi.org/10.1175/JAMC-D-17-0076.1, 2017.

Matrosov, S. Y., Orr, B. W., Kropfli, R. A., and Snider, J. B.: Retrieval of Vertical Profiles of Cirrus Cloud Microphysical Parameters from Doppler Radar and Infrared Radiometer Measurements, J. Appl. Meteorol. Clim., 33, 617–626, https://doi.org/10.1175/1520-0450(1994)033<0617:ROVPOC>2.0.CO;2, 1994.

Matrosov, S. Y., Heymsfield, A. J., and Wang, Z.: Dual-frequency radar ratio of nonspherical atmospheric hydrometeors, Geophys. Res. Lett., 32, https://doi.org/10.1029/2005GL023210, 2005.

Matrosov, S. Y., Maahn, M., and Boer, G. de: Observational and Modeling Study of Ice Hydrometeor Radar Dual-Wavelength Ratios, J. Appl. Meteorol. Clim., 58, 2005–2017, https://doi.org/10.1175/JAMC-D-19-0018.1, 2019.

Melnikov, V.: Parameters of Cloud Ice Particles Retrieved from Radar Data, J. Atmos. Ocean. Technol., 34, 717–728, https://doi.org/10.1175/JTECH-D-16-0123.1, 2017.

Milbrandt, J. A. and Yau, M. K.: A Multimoment Bulk Microphysics Parameterization. Part I: Analysis of the Role of the Spectral Shape Parameter, J. Atmos. Sci., 62, 3051–3064, https://doi.org/10.1175/JAS3534.1, 2005a.

Milbrandt, J. A. and Yau, M. K.: A Multimoment Bulk Microphysics Parameterization. Part II: A Proposed Three-Moment Closure and Scheme Description, J. Atmos. Sci., 62, 3065–3081, https://doi.org/10.1175/JAS3535.1, 2005b.

Mishchenko, M. I. and Travis, L. D.: T-matrix computations of light scattering by large spheroidal particles, Opt. Commun., 109, 16–21, https://doi.org/10.1016/0030-4018(94)90731-5, 1994.

Mishchenko, M. I., Travis, L. D., and Mackowski, D. W.: T-matrix computations of light scattering by nonspherical particles: A review, J. Quant. Spectrosc. Radiat. Transfer, 55, 535–575, https://doi.org/10.1016/0022-4073(96)00002-7, 1996.

Mishchenko, M. I., Dlugach, J. M., and Liu, L.: Applicability of the effective-medium approximation to heterogeneous aerosol particles, J. Quant. Spectrosc. Radiat. Transfer, 178, 284–294, https://doi.org/10.1016/j.jqsrt.2015.12.028, 2016.

Moisseev, D. N., Lautaportti, S., Tyynela, J., and Lim, S.: Dual-polarization radar signatures in snowstorms: Role of snowflake aggregation, J. Geophys. Res.: Atmos., 120, 12644–12655, https://doi.org/10.1002/2015JD023884, 2015.

Morrison, H. and Milbrandt, J.: Comparison of Two-Moment Bulk Microphysics Schemes in Idealized Supercell Thunderstorm Simulations, Mon. Weather Rev., 139, 1103–1130, https://doi.org/10.1175/2010MWR3433.1, 2011.

Morrison, H. and Milbrandt, J. A.: Parameterization of Cloud Microphysics Based on the Prediction of Bulk Ice Particle Properties. Part I: Scheme Description and Idealized Tests, J. Atmos. Sci., 72, 287–311, https://doi.org/10.1175/JAS-D-14-0065.1, 2015.

Morrison, H., Curry, J. A., and Khvorostyanov, V. I.: A New Double-Moment Microphysics Parameterization for Application in Cloud and Climate Models. Part I: Description, J. Atmos. Sci., 62, 1665–1677, https://doi.org/10.1175/JAS3446.1, 2005.

Morrison, H., Thompson, G., and Tatarskii, V.: Impact of Cloud Microphysics on the Development of Trailing Stratiform Precipitation in a Simulated Squall Line: Comparison of One- and Two-Moment Schemes, Mon. Weather Rev., 137, 991–1007, https://doi.org/10.1175/2008MWR2556.1, 2009.

Morrison, H., Milbrandt, J. A., Bryan, G. H., Ikeda, K., Tessendorf, S. A., and Thompson, G.: Parameterization of Cloud Microphysics Based on the Prediction of Bulk Ice Particle Properties. Part II: Case Study Comparisons with Observations and Other Schemes, J. Atmos. Sci., 72, 312–339, https://doi.org/10.1175/JAS-D-14-0066.1, 2015.

Morrison, H., van Lier-Walqui, M., Fridlind, A. M., Grabowski, W. W., Harrington, J. Y., Hoose, C., Korolev, A., Kumjian, M. R., Milbrandt, J. A., Pawlowska, H., Posselt, D. J., Prat, O. P., Reimel, K. J., Shima, S.-I., van Diedenhoven, B., and Xue, L.: Confronting the Challenge of Modeling Cloud and Precipitation Microphysics, J. Adv. Model. Earth Syst., 12, e2019MS001689, https://doi.org/10.1029/2019MS001689, 2020.

Mroz, K., Battaglia, A., Nguyen, C., Heymsfield, A., Protat, A., and Wolde, M.: Triple-frequency radar retrieval of microphysical properties of snow, Atmos. Meas. Tech., 14, 7243–7254, https://doi.org/10.5194/amt-14-7243-2021, 2021.

Myagkov, A., Seifert, P., Wandinger, U., Bauer-Pfundstein, M., and Matrosov, S. Y.: Effects of antenna patterns on cloud radar polarimetric measurements, J. Atmos. Ocean. Tech., 32, 1813–1828, https://doi.org/10.1175/JTECH-D-15-0045.1, 2015.

Nishikawa, M., Nakamura, K., Fujiyoshi, Y., Nakagawa, K., Hanado, H., Minda, H., Nakai, S., Kumakura, T., and Oki, R.: Radar Attenuation and Reflectivity Measurements of Snow With Dual Ka-Band Radar, IEEE Trans. Geosci. Remote Sens., 54, 714–722, https://doi.org/10.1109/TGRS.2015.2464099, 2016.

Petäjä, T., O'Connor, E. J., Moisseev, D., Sinclair, V. A., Manninen, A. J., Väänänen, R., Lerber, A. von, Thornton, J. A., Nicoll, K., Petersen, W., Chandrasekar, V., Smith, J. N., Winkler, P. M., Krüger, O., Hakola, H., Timonen, H., Brus, D., Laurila, T., Asmi, E., Riekkola, M.-L., Mona, L., Massoli, P., Engelmann, R., Komppula, M., Wang, J., Kuang, C., Bäck, J., Virtanen, A., Levula, J., Ritsche, M., and Hickmon, N.: BAECC: A Field Campaign to

Elucidate the Impact of Biogenic Aerosols on Clouds and Climate, Bull. Am. Meteorol. Soc., 97, 1909–1928, https://doi.org/10.1175/BAMS-D-14-00199.1, 2016.

Platnick, S., Ackerman, S., King, M., et al., 2015. MODIS Atmosphere L2 Cloud Product (06_L2). NASA MODIS Adaptive Processing System, Goddard Space Flight Center, USA, [data set], http://dx.doi.org/10.5067/MODIS/MOD06_L2.061

Reimann, J.: On fast, polarimetric non-reciprocal calibration and multipolarization measurements on weather radars, PhD dissertation, Technische Universität Chemnitz, 161 pp., https://nbn-resolving.de/urn:nbn:de:bsz:ch1-qucosa-132088 (last access: 8 April 2022), 2013.

Reimann, J. and Hagen, M.: Antenna Pattern Measurements of Weather Radars Using the Sun and a Point Source, J. Atmos. Ocean. Technol., 33, 891–898, https://doi.org/10.1175/JTECH-D-15-0185.1, 2016.

Ryzhkov, A. V. and Zrnic, D. S.: Data Quality and Measurement Errors, in: Radar Polarimetry for Weather Observations, Springer Atmospheric Sciences, Springer, Cham, https://doi.org/10.1007/978-3-030-05093-1_6, 2019.

Ryzhkov, A. V., Giangrande, S. E., Melnikov, V. M., and Schuur, T. J.: Calibration Issues of Dual-Polarization Radar Measurements, J. Atmos. Ocean. Technol., 22, 1138–1155, https://doi.org/10.1175/JTECH1772.1, 2005.

Schrom, R. S. and Kumjian, M. R.: Bulk-Density Representations of Branched Planar Ice Crystals: Errors in the Polarimetric Radar Variables, J. Appl. Meteorol. Clim., 57, 333–346, https://doi.org/10.1175/JAMC-D-17-0114.1, 2018.

Schroth, A. C., Chandra, M. S., and Mesichner, P. F.: A C-Band Coherent Polarimetric Radar for Propagation and Cloud Physics Research, J. Atmos. Ocean. Technol., 5, 803–822, https://doi.org/10.1175/1520-0426(1988)005<0803:ABCPRF>2.0.CO;2, 1988.

Steinert, J. and Chandra, M.: Classification of ice crystals at C-band, Adv. Radio Sci., 7, 273–277, https://doi.org/10.5194/ars-7-273-2009, 2009.

Straka, J. M., Zrnić, D. S., and Ryzhkov, A. V.: Bulk Hydrometeor Classification and Quantification Using Polarimetric Radar Data: Synthesis of Relations, J. Appl. Meteorol. Clim., 39, 1341–1372, https://doi.org/10.1175/1520-0450(2000)039<1341:BHCAQU>2.0.CO;2, 2000.

Sullivan, S. C. and Voigt, A.: Ice microphysical processes exert a strong control on the simulated radiative energy budget in the tropics, Commun. Earth Environ., 2, 1–8, https://doi.org/10.1038/s43247-021-00206-7, 2021.

Tetoni, E., Ewald, F., Hagen, M., Köcher, G., Zinner, T., and Groß, S.: Retrievals of ice microphysical properties using dual-wavelength polarimetric radar observations during stratiform precipitation events, Atmos. Meas. Tech., 15, 3969–3999, https://doi.org/10.5194/amt-15-3969-2022, 2022.

Tiira, J. and Moisseev, D.: Unsupervised classification of vertical profiles of dual polarization radar variables, Atmos. Meas. Tech., 13, 1227–1241, https://doi.org/10.5194/amt-13-1227-2020, 2020.

Tiira, J., Moisseev, D. N., von Lerber, A., Ori, D., Tokay, A., Bliven, L. F., and Petersen, W.: Ensemble mean density and its connection to other microphysical properties of falling snow as observed in Southern Finland, Atmos. Meas. Tech., 9, 4825–4841, https://doi.org/10.5194/amt-9-4825-2016, 2016.

Trömel, S., Simmer, C., Blahak, U., Blanke, A., Doktorowski, S., Ewald, F., Frech, M., Gergely, M., Hagen, M., Janjic, T., Kalesse-Los, H., Kneifel, S., Knote, C., Mendrok, J., Moser, M., Köcher, G., Mühlbauer, K., Myagkov, A., Pejcic, V., Seifert, P., Shrestha, P., Teisseire, A., von Terzi, L., Tetoni, E., Vogl, T., Voigt, C., Zeng, Y., Zinner, T., and Quaas, J.: Overview: Fusion of radar polarimetry and numerical atmospheric modelling towards an improved understanding of cloud and precipitation processes, Atmos. Chem. Phys., 21, 17291–17314, https://doi.org/10.5194/acp-21-17291-2021, 2021.

Tyynelä, J., Leinonen, J., Moisseev, D., and Nousiainen, T.: Radar Backscattering from Snowflakes: Comparison of Fractal, Aggregate, and Soft Spheroid Models, J. Atmos. Ocean. Technol., 28, 1365–1372, https://doi.org/10.1175/JTECH-D-11-00004.1, 2011.

University of Wyoming (UW): Radiosonde data, UW, [data set], http://weather.uwyo.edu/upperair/sounding.html, last access: 8 April 2022.

Wallace, J. M. and Hobbs, P. V.: Atmospheric science: an introductory survey, Second Edition, Vol. 92, Academic Press, https://doi.org/10.1016/C2009-0-00034-8, 2006.

Waterman, P. C.: Matrix formulation of electromagnetic scattering, Proc. IEEE, 53, 805–812, https://doi.org/10.1109/PROC.1965.4058, 1965.

Wolfensberger, D., Scipion, D., and Berne, A.: Detection and characterization of the melting layer based on polarimetric radar scans, Q. J. R. Meteorol. Soc., 142, 108–124, https://doi.org/10.1002/qj.2672, 2016.

Wu, D., Zhang, F., Chen, X., Ryzhkov, A., Zhao, K., Kumjian, M. R., Chen, X., and Chan, P.-W.: Evaluation of Microphysics Schemes in Tropical Cyclones Using Polarimetric Radar Observations: Convective Precipitation in an Outer Rainband, Mon. Weather Rev., 149, 1055–1068, https://doi.org/10.1175/MWR-D-19-0378.1, 2021.

Yang, P. and Liou, K.: Single-scattering properties of complex ice crystals in terrestrial atmosphere, Contrib. Atmos. Phys., 71, 223–248, 1998.

Yang, P., Liou, K. N., Wyser, K., and Mitchell, D.: Parameterization of the scattering and absorption properties of individual ice crystals, J. Geophys. Res.: Atmos., 105, 4699–4718, https://doi.org/10.1029/1999JD900755, 2000.

Zhang, Y., Li, Z., and Macke, A.: Retrieval of Surface Solar Radiation Budget under Ice Cloud Sky: Uncertainty Analysis and Parameterization, J. Atmos. Sci., 59, 2951–2965, https://doi.org/10.1175/1520-0469(2002)059<2951:ROSSRB>2.0.CO;2, 2002.

Zrnic, D. S., Melnikov, V. M., and Carter, J. K.: Calibrating Differential Reflectivity on the WSR-88D, J. Atmos. Ocean. Technol., 23, 944–951, https://doi.org/10.1175/JTECH1893.1, 2006.

Acknowledgements

The present doctoral thesis is the outcome of my three-and-a-half-year research at the Institut für Physik der Atmosphäre (IPA) of Deutsches Zentrum für Luft- und Raumfahrt (DLR). My multi-year research was funded within the priority program “Fusion of Radar Polarimetry and Numerical Atmospheric Modelling Towards an Improved Understanding of Cloud and Precipitation Processes” (SPP-2115, PROM) of the Deutsche Forschungsgemeinschaft (DFG), especially for the project “Investigation of the initiation of convection and the evolution of precipitation using simulations and polarimetric radar observations at C- and Ka-band” (IcePolCKa) with grant no. HA 3314/9-1.

Being a part of the Lidar department of the IPA institute, I would like to thank all my colleagues for the great collaboration and spirit all these years.

In particular, I would like to thank Dr. Silke Groß for her guidance and her full support throughout my studies not only in a professional but also in a personal way. During my hardest times, she was there to fully encourage me to continue my research with more strength and willingness.

Exceptional thanks also to my mentor Dr. Florian Ewald. During these years he supported me in any way; professional or friendly. While I was sometimes struggling to find a solution, he was always there giving me hints to accomplish my Ph.D. goals, but he was also there during my biggest life challenges here in Germany.

I would also like to thank my colleagues, Dr. Martin Hagen, Dr. Tobias Zinner and Gregor Köcher for the fruitful discussions that we had during our meetings and their scientific help and ideas within the framework of the IcePolCKa project. Special thank also to Dr. Manuel Gutleben and Dr. Robert Reichert for the whiteboard sessions we had in our office.

Except for my colleagues, I would also like to thank my family and especially my mother for being there when I mostly needed her. Last but not least, I would like to thank my husband, Nikolaos Nikolaou, who absolutely supported my dream to do my doctoral studies on radars, even if that meant that I had to move and study abroad.